Carbon Nanotube Field Effect Transistors with Al$_2$O$_3$ Passivated Metal Contacts as NO$_2$ Gas Sensors

A dissertation submitted to
ETH Zurich

for the degree of
Doctor of Sciences

presented by
Moritz Peter Paul Mattmann
Dipl. El.-Ing. ETH, ETH Zurich

born September 13, 1983
citizen of Hohenrain LU

accepted on the recommendation of
Prof. Dr. Christofer Hierold, examiner
Prof. Dr. Janos Vörös, co-examiner

2011

Tore schiessen, gewinnen, Erfolg haben.
Die Frechheit, in den leeren Raum zu spielen -
wo es jetzt grad noch leer ist, ist Zukunft!
Zukunft können wir nicht sichern. Wir müssen sie wagen.

Ludwig Hasler, Engineering Days 2010

to my family

Abstract

Single walled carbon nanotubes (SWNTs) are hollow cylindrical structures with their sidewalls consisting of carbon atoms arranged in a hexagonal lattice. They feature diameters ranging from 0.4 to 4 nm and are typically up to several μm long. Since all carbon atoms are in direct contact with the environment their electrical properties are very sensitive to changes in their chemical environment. As such, they are predestinated to be employed as sensitive material in novel chemical sensors. In 2000, Kong *et al.* first demonstrated NO_2 detection with SWNT based field effect transistors (CNFETs). The CNFET sensors were operated at room temperature (RT), which rendered them very power-efficient compared to today's heated metal-oxide based gas sensors.

In this thesis, inspired by the promising results by Kong *et al.* and other research groups and driven by the need for power-efficient, longterm stable NO_2 sensing technologies, we propose, fabricate and characterize an enhanced CNFET sensor structure for NO_2 detection. The proposed CNFETs are operated with a Si backgate and employ individual SWNTs (1 μm length) as channel, from which only the middle section (0.5 μm length) is exposed to the ambient and used for NO_2 sensing. The rest of the sensor structure is buried under an atomic layer deposited (ALD) Al_2O_3 film of 40 nm thickness. This ensures that the delicate source and drain metal contacts (Cr/Au) are protected from unwanted environmental influences, such as oxidation, and results in an improved device lifetime in ambient conditions (310 days measured) compared to as-prepared, non-passivated CNFETs. We demonstrate a limit of detection (LOD) of 0.1 ppm NO_2, which is comparable with minimum NO_2 concentrations measured with other CNFETs with pristine SWNT channels. Sensor recovery from NO_2 exposure is achieved at RT within about 24 h and can be accelerated by heat treatment (110 °C) for 1 h. During NO_2 sensing, our sensors feature a power consumption in the range of tens of nW. This value is comparable to other CNFET chemical sensors and about 6 orders of magnitude lower compared to today's heated metal-oxide based NO_2 sensors.

CNFETs often suffer from substantial gate hysteresis due to trapped charges in the vicinity of the SWNT channels. For CNFETs operated as chemical sensors, gate hysteresis can hamper the unambiguous extraction of the intrinsic threshold voltage (V_{th}) as sensor output signal, which is a direct measure for an analyte induced shift of the Fermi level (E_F). We demonstrate that pulsed gate voltage (V_g)

SWNTs

Enhanced Sensor Structure

Gate Hysteresis

Abstract

waveforms with pulse times t_{high} in the order of ms can be used instead of continuous V_g to essentially eliminate gate hysteresis during NO_2 sensing. In pulsed V_g regime, small NO_2 induced shifts of V_{th} remain resolvable and we observe an enhancement of the measurement range due to the improved gate coupling compared to the continuous V_g mode. For discussion of the measurement result, we use a hysteresis model adapted to the pulsed V_g waveforms. In addition, it is shown that pulsed V_g strategies can be used to electrically initialize CNFETs before measuring $I_d V_g$ characteristics for the extraction of the V_{th} sensor signal. This can help to improve the sensors' reliability, especially close to the LOD, when NO_2 induced shifts of V_{th} are small.

Humidity and temperature are two external parameters to which sensor are very likely to be exposed in real-life applications. We perform a preliminary study, which reveals that increased gate hysteresis is the dominant first order effect upon increasing temperature (300 K $\leq$ T $\leq$ 390 K) and humidity (r.h. $\leq$ 70 %). It is shown that pulsed V_g strategies can be used to essentially eliminate the humidity and temperature caused gate hysteresis. Especially a pulsed V_g waveform, based on pulses of alternating polarity, shows good hysteresis reduction capabilities, even with relatively long pulse times (t_{high} = 50 ms). The NO_2 detection behavior of our sensors in moderate humid conditions (40 % r.h.) is found to be very similar to NO_2 sensing in dry conditions with similar LOD. Above 70 % r.h. the CNFET NO_2 sensors can not be operated any longer. Measurement data suggests that adsorbed H_2O molecules start to form a conductive film on the sensor surface, which electrically shortcuts the exposed SWNT channel and the Si backgate electrode. We propose strategies how to enable sensor operation at high humidity levels.

Finally, we address the issue of defining a time-dependent sensor output signal. Three different schemes are investigated to form a sensor output signal from consecutively recorded $I_d V_g$ characteristics. All three signals are found to suffer from considerably high signal fluctuations, which severely limit the signal to noise ratio (SNR). Recording of $I_d V_g$ characteristics over 72 h with 1 min sampling rate reveals, that the observed fluctuations are random, mostly in the form of rigid shifts along the V_g axis. The obtained $1/f$ frequency spectrum suggests that mostly fluctuating trap sites near the SWNT channel are the origin for the high noise level. We propose and discuss different strategies to reduce the charge trap density in our sensors to improve the SNR.

The findings of this thesis extend the state-of-the-art knowledge in CNFET chemical sensors and provide some of the many still missing stepping stones on the way to a mature CNT based chemical sensing technology.

Electrical
Initialization

Humidity &
Temperature

Sensor Output
Signal

Zusammenfassung

Einwandige Kohlenstoff Nanoröhrchen (SWNTs) sind hohle, zylindrische Struk-
turen, deren Seitenwände aus Kohlenstoffatomen bestehen, die in einem hexa-
gonalen Gitter angeordnet sind. SWNTs haben Durchmesser zwischen 0.4 und 4
nm und sind typischerweise bis zu mehreren μm lang. Da in SWNTs alle Kohlen-
stoffatome in direktem Kontakt mit der Umgebung sind, reagieren ihre elektro-
nischen Eigenschaften sehr sensitiv auf Veränderungen der chemischen Zusam-
mensetzung ihrer Umgebung. Deshalb sind SWNTs prädestiniert, um als sensiti-
ves Material in neuartigen, chemischen Sensoren eingesetzt zu werden. Im Jah-
re 2000 wurden SWNT basierte Feldeffekttransistoren (CNFETs) zum ersten Mal
von Kong *et al.* als chemische Sensoren eingesetzt und die Detektion von NO_2 Gas
erfolgreich demonstriert. Da SWNTs nur aus Oberflächenatomen bestehen, kön-
nen CNFET-Sensoren bei Raumtemperatur betrieben werden. Das macht sie sehr
energieeffizient im Vergleich zu heutigen Metalloxid-basierten Gassensoren, die
im Detektionsbetrieb geheizt werden müssen.

Inspiriert durch die vielversprechenden Resultate von Kong *et al.* und anderen
Forschungsgruppen und getrieben von der Nachfrage nach energieeffizienten und
langzeitstabilen NO_2 Gassensoren, präsentieren, fabrizieren und charakterisieren
wir in dieser Arbeit eine erweiterte CNFET-Sensorstrukur für die Detektion von
NO_2. Die erweiterte CNFET-Sensorstrukturen werden mit einer Si Gateelektro-
de betrieben und haben einzelne SWNTs (1 μm Länge) als Transistorkanal. Vom
Kanal is nur der Mittelteil (0.5 μm Länge) der Umgebung ausgesetzt und wird
zur Detektion von NO_2 verwendet. Der Rest der Sensorstruktur ist abgedeckt
von einer Dünnfilmschutzschicht, bestehend aus Al_2O_3 (40 nm dick), die in ei-
nem atomic layer deposition (ALD) Prozess abgeschieden wird. Die Schutzschicht
stellt sicher, dass die empfindlichen Metallkontakte (Cr/Au) von unerwünschten,
äusseren Einflüssen, z.B. Oxidation, geschützt sind. Dadurch kann die Sensorle-
benszeit in Umgebungsluft (310 Tage gemessen) deutlich verbessert werden im
Vergleich zu CNFET-Sensoren ohne Schutzschicht. Weiter zeigen wir, dass unsere
Sensoren eine Detektionsgrenze von 0.1 ppm NO_2 aufweisen, was ungefähr ver-
gleichbar ist mit anderen CNFET-Sensorstrukturen, die ebenfalls chemisch unver-
änderte SWNTs als Kanal verwenden. Sensorrückstellung nach NO_2-Exposition,
dauert bei Raumtemperatur etwa 24 h und kann durch Ausheizen des Sensors
bei 110 °C auf etwa 1 h reduziert werden. Im Detektionsbetrieb weisen unsere

SWNTs

Erweiterte
Sensorstruktur

Zusammenfassung

Sensoren einen Energieverbrauch im Bereich von mehreren zehn nW auf. Dieser Wert ist ungefähr vergleichbar mit anderen CNFET chemischen Sensoren und etwa 6 Grössenordnungen kleiner im Vergleich zu heutigen, beheizten Metalloxid-basierten NO_2 Gassensoren.

Hystereseeffekt

Infolge von beweglichen Ladungsträgern, die sich in der Nähe des SWNT-Kanals befinden, weisen Kennlinien von CNFETs häufig Hysterese auf. Für CNFETs, die als chemische Sensoren betrieben werden, kann Hysterese die eindeutige Bestimmung der intrinsischen Schwellspannung (V_{th}) beeinträchtigen. Diese wird häufig als Sensorausgangssignal verwendet, da diese eine direkte Information über die NO_2 induzierte Verschiebung der Fermienergie (E_F) liefert. In dieser Arbeit zeigen wir, dass anstelle von kontinuierlichen Signalverläufen der Gatespannung (V_g), gepulste V_g Signale mit Pulslängen im Bereich von ms verwendet werden können, um die Hysterese in Kennlinien von CNFETs während der Detektion von NO_2 praktisch vollständig zu unterdrücken. Mit gepulsten V_g Signalen können auch sehr kleine Verschiebungen von V_{th} aufgelöst werden und zudem wird der Messbereich des Sensors erweitert, dank der verbesserten Gatekopplung im Vergleich zum Betrieb mit kontinuierlichen V_g Signalen. Für die Diskussion der Messresultate ziehen wir ein Hysteresemodell bei, welches für die gepulsten V_g Signale angepasst wurde. Des Weiteren zeigen wir, dass gepulste V_g Signale auch dazu verwendet werden können, um CNFETs elektrisch zu initialisieren bevor eine Transistorkennlinie aufgenommen und V_{th} als Sensorsignal davon extrahiert wird. Die Initialisierung kann helfen, um die Zuverlässigkeit des Sensors zu erhöhen, speziell Im Bereich der Detektionsgrenze, wo nur kleine Verschiebungen von V_{th} auftreten.

Elektrische Initialisierung

Feuchte & Temperatur

Feuchte und Temperatur sind zwei äussere Einflüsse, welchen Sensoren in realen Anwendugen mit grosser Wahrscheinlichkeit ausgesetzt sind. Wir präsentieren hier eine Untersuchung, welche zeigt, dass eine Vergrösserung der Hysterese in CNFET Kennlinien der dominante Effekte in Folge steigender Temperatur ($300 \leq T \leq 390$ K) und Feuchte (relative Feuchte ≤ 70 %) ist. Weiter wird gezeigt, dass gepulste V_g Signale verwendet werden können, um die durch Feuchte und Temperatur induzierte Vergrösserung der Hysterese fast vollständig zu unterdrücken. Ein gepulstes V_g Signal, welches aus Pulsen wechselnder Polarität besteht, vermag die Hysterese besonders gut zu reduzieren, selbst bei der Verwendung relativ langer Pulszeiten (t_{high} = 50 ms). Das Verhalten der CNFET Sensoren während NO_2 Detektion in moderat feuchten Bedingungen (40 % r.f.) ist dem Sensorverhalten in trockenen Bedingungen sehr ähnlich, mit vergleichbaren Detektionsgrenzen für NO_2. In Bedingungen mit realtiver Feuchte über 70 %, können die CNFET NO_2 Sensoren nicht mehr betrieben werden. Sorgfältige Analyse der Messdaten lässt vermuten, dass auf der Chipoberfläche adsorbierte H_2O Moleküle einen elektrisch leitfähigen Film zu formen beginnen, der den Mittelteil

des SWNT Kanals und die Si Gateelektrode elektrisch kurzschliesst. Wir schlagen mögliche Massnahmen vor, um den Sensorbetrieb auch in sehr feuchten Bedingungen zu ermöglichen.

Im letzten Teil dieser Arbeit widmen wir uns der Problematik, ein zeitabhängiges Sensorsignal zu definieren. Wir untersuchen drei verschiedene Strategien, um ein Sensorausgangssignal aus nacheinander aufgenommenen CNFET Kennlinien zu bilden. Alle drei Signale weisen grosse Fluktuationen auf, welche das Signal-zu-Rausch-Verhältnis stark vermindern. Analyse von CNFET Kennlinien, welche über eine Zeitdauer von 72 h im Abstand von 1 min aufgenommen wurden, zeigt, dass die Signalfluktuationen zufälliger Natur sind und meist in der Form von reinen Verschiebungen entlang der V_g Achse auftreten. Das Frequenzspektrum der Signalfluktuationen zeigt ein 1/f Verhalten, was darauf hinweist, dass zu einem grossen Teil fluktuierende Ladungen in der Nähe des SWNT Kanals für den hohen Rauschpegel verantwortlich sind. Wir diskutieren und schlagen einige möglichen Strategien vor, um die Dichte von Ladungsfallen in unseren Sensoren zu reduzieren, um das Signal-zu-Rausch-Verhältnis zu verbessern.

Sensorausgangssignal

Die Resultate dieser Arbeit erweitern den aktuellen Stand der Technik von CNFET chemischen Sensoren. Zudem werden einige der noch vielen offenen Fragen beantwortet, die in der Entwicklung einer neuen Sensortechnologie geklärt werden müssen.

Acknowledgment

First, I would like to thank Prof. Christofer Hierold for giving me the opportunity to pursue my PhD thesis in his research group. I really enjoyed the stimulating atmosphere and the exceptional infrastructure, which he provides to his students. I'm also very grateful to Maximilian Fleischer, Roland Pohle and Erhard Magori of Siemens AG Corporate Technology in Munich, who let me use their gas mixing units to characterize my devices in NO_2.

I'm deeply indebted to Cosmin Roman and Thomas Helbling, who generously spent their time helping me planning my experiments, learning fabrication processes and discussing results. We also shared philosophical thoughts and had great discussions (not only about carbon nanotubes), which I keep in good memory. I would like to thank Lukas Durrer, Matthias Muoth, and Shih-Wei Lee for the excellent quality carbon nanotubes, which they provided me for the fabrication of my sensor devices. I'm also grateful to Kiran Chikkadi, Valentin Döring, Tobias Süss, Miroslav Haluska, Hengky Chandrahalim and Emine Cagin for the fruitful discussions with them and their help and collaboration during device fabrication and characterization. It has been a great pleasure for me to work also with all the other and former members of the MNS group. I really spent an enjoyable time during my PhD project.

During my project I had the pleasure to collaborate with Master students, who I wish to thank for their significant contributions to my thesis. These are Daniel Bechstein, Kiran Chikkadi, Ralf Flückiger and Robert Schrobenhauser.

I also really appreciated the help of Eeva Köpilä and Rebekka Hugger to deal with all the administrative duties.

Further, I'm thankful to all people, who help maintaining the great infrastructure of the clean room environment in FIRST-CLA and FIRST-Hönggerberg. Especially Sandro Bellini and Otte Homan gave me stimulating ideas how to solve issues, which arose during device fabrication.

Last but not least I am very grateful to my girlfriend Isabelle for her great support during my PhD thesis and for cheering me up when experiments had failed. I also would like to thank my parents, who made it possible for me to study at ETH and also supported me in many ways during my PhD project.

Contents

Contents

List of Symbols and Abbreviations

Symbol	Unit	Description
a	m	Length of the graphene basis vector
a	A/MV^2	constant in the expression for FN current
$\vec{a}_1, \vec{a}_2$	m	Basis vectors of the graphene lattice
a_{cc}	Å	Length of the carbon-carbon bond in the graphene lattice ($a_{cc} = 1.42$ Å)
b	MV/cm	constant in the expression for FN current
$\vec{C}_h$	m	Circumferential vector of a SWNT
d	nm	Diameter of a SWNT
e	C	Electron charge ($e = 1.602 \cdot 10^{-19}$ C)
E	V/m	Electric field strength
E_c	eV	Energy of the conduction band edge
E_F	eV	Fermi energy
E_g	eV	Electronic bandgap of a SWNT
E_v	eV	Energy of the valence band edge
ϵ_0	$CV^{-1}m^{-1}$	Vacuum permittivity ($\epsilon_0 = 8.854 \cdot 10^{-12}$ $CV^{-1}m^{-1}$)
ϕ_m	eV	Workfunction of a metal
ϕ_B	eV	Energy barriers for electrons or holes
ϕ_B^n	eV	Energy barriers for electrons
ϕ_B^p	eV	Energy barriers for holes
ϕ_{ext}	V	SWNT surface/external potential
ϕ_{SB}^n	eV	Schottky barrier height for electrons
ϕ_{SB}^p	eV	Schottky barrier height for holes
G	Ω^{-1}	Electrical conductance
G_0	Ω^{-1}	Quantum conductance ($\hat{=}1/12.9k\Omega^{-1}$)
γ_0	eV	Hopping integral
h	Js	Planck constant ($h = 6.62 \cdot 10^{-34}$ Js)
H	V	Width of the gate hysteresis in CNFETs
I_d	A	CNFET source-drain current
I_{FN}	A	Fowler-Nordheim current
I_{on}	A	Transistor on-state current
k_B	J/K	Boltzmann constant ($k_B = 1.38 \cdot 10^{-23}$ J/K)
L	m	Channel length in a FET
L_ϕ	m	Electron phase relaxation length

l_e	m	Electron mean free path
n, m		Chiral indices of a SWNT
M		Number of modes in a quantum conductor
R	Ω	Electrical resistance of a conductor
R_c	Ω	Contact resistance of a CNFET
r	m	Radius of a SWNT
$r.h.$	%	relative humidity level
T	K	Temperature
θ	°	Chiral angle of a SWNT with $0° \leq \theta \leq 30°$
t_{high}	s	Gate pulse high time during pulsed V_g
t_{low}	s	Gate pulse low time during pulsed V_g
t_{acq}	s	I_d acquisition time during pulsed V_g
t_c	s	Duration of a charge pulse
t_{total}	s	Total duration of a V_g sweep
t_{ox}	m	Thickness of the gate oxide
V_{sd}	V	Source-drain voltage
V_g	V	Gate voltage
$V_{g,max}$	V	Maximum gate voltage
V_{th}	V	Threshold voltage of a transistor
V_{thzero}	V	Initial threshold voltage of a transistor
V_{trap}	V	Potential due to trapped charges
χ_s	eV	Electron affinity of a SWNT

1 Introduction

In our everyday life we are exposed to a vast number of external stimuli. This might be the sound of classical music, the taste of a delicious lunch, the smell of a flower, blinking traffic lights at a crossing or the touch during a handshake. All these stimuli we are able to sense and interpret thanks to our body's own sensor network, nerves and certainly our brain. As such, our sensor system helps us to perceive our environment and allows us to interact accordingly with it. Typically, five human senses are distinguished: sight, hearing, taste, touch and smell [1].

Despite the richness and the astonishing sophistication of human senses, there exist stimuli in our environment, which we are not able detect. It might be because our senses are totally insensitive to them (e.g. sound in the ultrasonic frequency range or ultraviolet radiation) or not sensitive enough (e.g. very low concentrated odor). Stimuli, which are "invisible" for us, can be problematic if they are harmful for our health. In such situations, we can enhance our natural senses by artificial sensors systems, which are able to detect harmful stimuli and warn us from toxication in any for us perceivable way.

Long time before modern sensor technologies were available, humans already employed primitive detectors. In early days, when coal mines were not equipped with ventilation systems, miners ran the risk of dying from exposure to natural toxic gases such as methane or carbon monoxide. The miners took canary birds with them into the mines, which they knew to be more sensitive to these gases than humans. If the birds suddenly stopped tweeting, the miners knew that they were in danger due to the presence of toxic gases and could leave the contaminated mine [2].

Nitrogen dioxide (NO_2) is one of the six common air pollutants for which the U.S. Environmental Protection Agency (EPA) has to set standards, since they are harmful for public health and the environment [3]. At room temperature NO_2 is a gaseous compound, which is emitted into the air by combustion processes of fossil fuels. It is very toxic for humans by inhalation and can, according to EPA, lead to adverse respiratory effects, such as airway inflammation and asthma. To monitor the set standards a network of NO_2 sensors is required, which currently consists of only 81 NO_2 monitors [3] spread over the US. The lethal concentration for rats is reported to be 115 ppm / 1h [4]. The MAK (Maximale Arbeitsplatzkonzentration - maximum allowed concentration at workplace) value for NO_2 is at 6 mg/m^3 or

about 5 ppm [5]. In case of NO_2, danger for humans does not only come from exposure to the gas itself but it can be the signature of chemical reactions and events, which can be even more drastic for human life. As such, NO_2 monitoring might be useful for fire prevention. In contrast to optical fire detectors, a NO_2 sensor based fire detector would be independent from the formation of smoke during a fire. Additionally, gas sensors may capture valuable early information about the type of a fire, as different test fires, performed according to the European standard EN54, show different gas fingerprints [6]. Breath analyzing to uncover disposition of patients for asthma [7, 8] is another application for NO_x monitoring. As NO_2 is the product of combustion processes, it can be used to monitor and control the characteristics of combustion processes. Placed in the exhaust stream of any kind of burner, a NO_2 sensor may give a feedback signal, which can be used to optimize burning processes.

Sensor Requirements In [9] an extensive list of requirements on sensor technologies can be found. Typically, they heavily depend on the target application. For the above listed applications for NO_2 sensing, we can identify three main requirements on an "ideal sensor" technology, which are indispensable for sensors used in ubiquitous networks and which can serve us in almost any situation of daily life:

- *Power consumption.* If the sensors are supposed to accompany humans in almost any situation or if they are installed in large numbers, forming sensor networks, they may have to be powered by batteries or any kind of energy harvesting technology. The sensor power consumption therefore needs to be small to enable operation from low power sources or to ensure long-time operation without replacement of the power supply.

- *Lifetime.* The sensor should have a long lifetime to avoid frequent sensor replacement and therewith high maintenance costs.

- *Costs.* In order to make the sensor technology affordable for everyone in a large number and to build closely meshed sensor network, the costs should be low.

Commercial NO_2 Sensors There exist already commercial-off-the-shelf (COTS) NO_2 sensors. The two prevalent technologies are electrochemical cells [10–13] and metal oxide based sensors [13, 14]. In section 2.3.4, we will look in more detail at the two technologies. However, in brief we can state: while electrochemical cells show limited lifetimes, metal oxide oxide based sensors suffer from high power consumption, since they need to be heated during operation.

SWNT Based NO_2 Sensor In 2000, Kong *et al.* [15] first demonstrated NO_2 detection with single walled carbon nanotube (SWNT) based transistors (CNFETs). SWNTs are hollow cylinders

with their sidewalls consisting of carbon atoms arranged in a hexagonal lattice structure. They have diameters in the range of 0.4 to 4 nm and are typically several μm long. All their carbon atoms are surface atoms and are therewith in direct contact with environment. This makes SWNTs very sensitive to changes in their chemical environment and species adsorbed onto SWNTs affect their electronic properties without prior diffusion into the material bulk. As such, SWNT based chemical sensors do not require heating and can be operated at room temperature, which makes them very power-efficient. Further, SWNTs feature strong sp^2 bonds between their carbon atoms, which render SWNTs mechanically very stable and chemically quasi-inert. From this structural property long sensor lifetime might be envisioned.

As such, CNFET based chemical sensing technology has high potential to simultaneously be low-power in operation (no heating is required), can be cheap (simple FET sensor structure) and may have lifetimes of several years (due to the intrinsically stable structure of SWNTs).

1.1 Scope and organization of the thesis

The first study about carbon nanotube (CNT) based chemical sensors has triggered a massive number of follow-up studies on this topic. As such, many additional device architectures were proposed and the detection of almost any imaginable (bio)chemical analytes was demonstrated. All these studies achieved substantial progress in understanding the working principle of these devices. However, before CNT based chemical sensing technology is mature enough to become competitive to established sensing technologies, a large number of fundamental questions still needs to be clarified.

Open Issues

The scope of this thesis is to investigate some of the open issues related to CNFET chemical sensing technology to advance the current state-of-the-art. Namely, sensor lifetime, sensor reliability with regards to hysteretic effects, first order effects due humidity and temperature on CNFET electrical properties and the definition of a sensor output signal are addressed here. To focus efforts and avoid random research of open sensor issues, we performed a Failure Mode and Effect Analysis (FMEA) [16] in the early phase of the project, see appendix C. The FMEA helped us to recognize dependencies between so far unaddressed questions, which was useful to decide the order of investigation.

FMEA

The thesis is structured as follows:

Chapter 2 This chapter covers the essential theoretical background. It starts

with a short overview of the basic structural and electronic properties of SWNTs. Then, the the SWNT based transistor (CNFET) is introduced with its basic properties such as electrical transport through the SWNT channel, SWNT-metal interfaces and gate hysteresis. In the last part we introduce the CNFETs as NO_2 sensors with their major sensing mechanisms and give a short state-of-the-art overview. The chapter ends with a comparison of SNWT-based NO_2 sensors with commercially available NO_2 sensors.

Chapter 3 The fabrication process of the CNFET NO_2 sensors is detailed and illustrated in this chapter. Further, the used electrical measurement setup with its different measurement modes is presented. Finally, the gas mixing unit, the employed NO_2 gas calibration method and the used gas measurement chamber are introduced.

Chapter 4 Since as-prepared CNFETs suffer from on-state conductance degradation, a new CNFET structure is proposed to be used as NO_2 sensors. The structure features an exposed midsection of the gas sensitive SWNT channel, while the degradation-prone SWNT-metal interfaces are protected from the ambient by an atomic layer deposited (ALD) Al_2O_3 layer. In this chapter, the new CNFET sensor structure is subject to numerous systematic tests. First, the sealing properties of ALD Al_2O_3 against high concentrations of NO_2 are tested. Then, the NO_2 detection behavior and the sensor recovery are verified. Finally, also improved long-term stability of the proposed CNFET sensor structure compared to as-prepared CNFETs is discussed.

Chapter 5 This chapter is dedicated to the issue of CNFET gate hysteresis, an undesired effect due to trapped charges in the vicinity of the SWNT channel. We test different pulsed V_g waveforms for hysteresis reduction in synthetic dry air and during NO_2 detection for hysteresis reduction. During discussion of the measurement data we employ an adapted gate hysteresis model. At the end of the chapter we demonstrate that pulsed V_g can be used to remove electrical charges near the SWNT channel and therewith electrically initialize CNFET sensors.

Chapter 6 Exposure to humidity and temperatures in the range above room temperatures are conditions, which sensors are highly probable to face in real-life applications. In this chapter we present the results of preliminary studies, which investigate first order effects of these two external parameters on CNFET electrical properties. We expose CNFET devices to humidity in synthetic air and during NO_2 detection and to temperatures in the range of 300 to 390 K in synthetic air.

Chapter 7 In the last chapter we address the issue of defining a time-dependent sensor output signal for our CNFET NO_2 sensors. From consecutively recorded $I_d V_g$ characteristics we extract three different parameters to form a sensor output signal. We compare their ability to reveal the presence of NO_2 and discuss the observed signal fluctuations.

2 Theory

In this chapter, the theoretical background is presented, which is necessary to understand the results, discussions and conclusions of this thesis. First, single-walled carbon nanotubes (SWNTs) and their structural and electronic properties are introduced. This part is intentionally kept short since there exist already several theses from the Micro and Nanosystems group at ETH [17–21], numerous textbooks [22–26] and review papers [27–30], which cover this topic thoroughly. In the second section, the sensor building block, a CNFET with an individual SWNT as conductive channel, which is employed in this thesis, is more deeply introduced. The electronic transport in the SWNT channel and especially the SWNT-metal interface in a CNFET are discussed. Further, gate hysteresis, an usually undesired but prevalent property of CNFETs operated with exposed SWNT channel, as is often the case with CNFET chemical sensors, is introduced. Based on the concept of charge trapping, a gate hysteresis model was developed by Robert-Peillard *et al.* [31], which is applied and adapted later in the thesis to better understand the recorded measurement data. The basic working principle of the gate hysteresis model is explained in the last part of this section.

Finally, CNT based NO_2 gas sensors are presented, starting with SWNTs as sensitive material in chemial sensors and the explanation of the NO_2 gas sensing mechanisms in CNFETs. Then, a short state-of-the-art overview about CNFET NO_2 sensors is presented, followed by a comparison to commercially available NO_2 gas sensors.

2.1 Single-walled carbon nanotubes (SWNTs)

Single-walled carbon nanotubes (SWNTs) are hollow cylindrical structures of about 0.4 to 4 nm in diameter and typically several μm in length. Their sidewalls consist of one layer of carbon atoms, which are arranged in a hexagonal lattice structure. In 1991, it was the Japanese research group around Sumio Iijima [32], who first reported the synthesis of multi-walled carbon nanotubes (MWNTs), which feature multiple concentric shells. Two year later the discovery of SWNTs was reported [33].

It is not only due to their probably most obvious property of small size that CNTs

have attracted the attention of so many research groups around the world. Since their discovery, many other exceptional properties of CNTs have been theoretically predicted and/or experimentally verified: their metallic or semiconducting electrical behavior, the high piezoresistivity, their high surface-to-volume-ratio and their very high tensile strength. All these properties, and the listing is by far not complete, triggered an amazing variety of possible applications [34] including electronics [35–39], sensors [15, 40–44], actuators [45] and optical applications [46–48].

2.1.1 Structural properties

A SWNT can be imagined as being formed by rolling up a single layer of graphite, also called graphene, into a hollow cylindrical structure. Depending on the width of the rolled up graphene sheet, SWNTs of different diameters can be formed. Its structure can therefore by specified by its circumferential vector, also called chiral vector $\vec{C}_h$ [24], shown in Fig. 2.1. The chiral vector can be expressed as $\vec{C}_h = n\vec{a}_1 + m\vec{a}_2$, the linear combination of the two graphene lattice vectors $\vec{a}_1$ and $\vec{a}_2$ [25]. The two integers n and m uniquely define the structure of a SWNT and are called indices. With this information the diameter of a SWNT can be expressed as:

Chiral Vector

Diameter

$$d = \frac{\left|\vec{C}_h\right|}{\pi} = \frac{a}{\pi}\sqrt{n^2 + nm + m^2}. \tag{2.1}$$

$a_0 = \left|\vec{a1}\right| = \left|\vec{a2}\right| = \sqrt{3}\, a_{cc} = 2.461$ Å with $a_{cc} \cong 1.42$ Å, the bond length of two carbon atoms in a graphene sheet.

Chiral Angle

By means of the indices (n,m) the chiral angle θ can be defined, which also uniquely defines the structure of a SWNT. θ is defined as the the angle between the chiral vector $\vec{C}_h$ and the unit vector $\vec{a}_1$ and is calculated as:

$$cos(\theta) = \frac{\vec{a}_1 \cdot \vec{C}_h}{\left|\vec{a}_1\right|\left|\vec{C}_h\right|} = \frac{2n + m}{2\sqrt{n^2 + nm + m^2}}. \tag{2.2}$$

The value of θ can be restricted to an interval $0 \leq \theta \leq 30°$ due to the hexagonal symmetry of the graphene sheet. Typically, SWNTs are then classified into three types according to the value of θ or their indices (n,m):

SWNT Classes

- $\theta = 30°$. (n,n). These SWNTs are called armchair nanotubes, due to the armchair pattern along the chiral vector (Fig. 2.1a).

- $\theta = 0°$. (n,0). These SWNTs are called zigzag nanotubes, because they feature a zigzag pattern along the chiral vector (Fig. 2.1b).
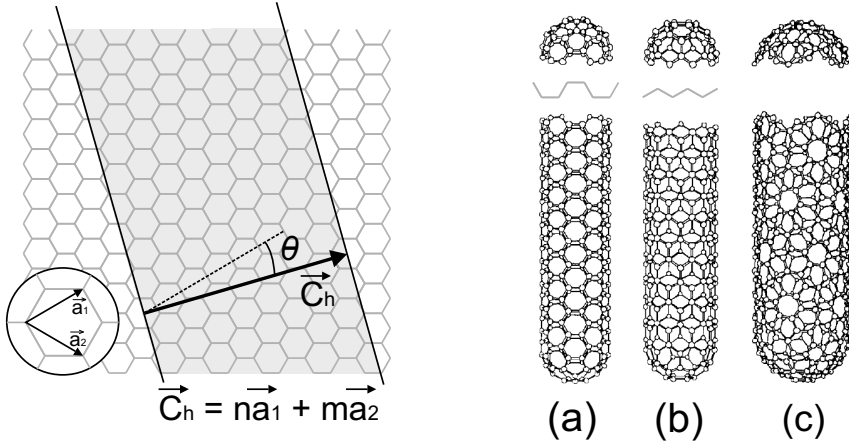
Figure 2.1: Stripe of a graphene sheet (highlighted area), which is rolled up to form a SWNT. $\vec{C}_h$ is the circumferential vector or chiral vector. $\vec{a}_1$ and $\vec{a}_2$ are the two lattice vectors of graphene. (5,5) armchair SWNT (a),(9,0) zigzag SWNT (b) and (10,5) chiral SWNT (c). Adapted from [49]. Copyright Elsevier Ltd 1995.

- $0 < \theta < 30°$. (n,m $\neq$ n $\neq$ 0). These SWNTs are called chiral nanotubes (Fig. 2.1c).

2.1.2 Electronic properties

Similarly, to understand and describe the structural properties of SWNTs, the electronic properties of SWNTs can be considered to be derived from the electronic properties of graphene. Via the tight binding model the electronic properties of an infinitely large sheet of graphene can be obtained. Rolling up graphene into a tube to form a SWNT, the graphene sheet is confined to a stripe of width $\left|\vec{C}_h\right|$. This imposes new boundary conditions on the electronic properties of graphene and by means of the so-called zone folding approximation, the electronic properties of SWNTs can be finally derived. In brief, how a sheet of graphene is rolled up determines the electronic properties of the resulting SWNT, which can be either metallic or semiconducting. SWNTs with indices (n,m), where (n-m) mod3 $\neq$ 0, are predicted by the above model to be semiconducting ($\frac{2}{3}$ of all SWNTs) and SWNTs with (n-m) mod3 = 0 are are predicted to be metallic ($\frac{1}{3}$ of all SWNTs). Band diagrams and the density of states (DOS) for a semiconducting SWNT (11,0) zigzag (a) and a metallic (6,6) armchair SWNT (b) are shown in Fig. 2.2. In the remaining text, m-SWNTs and s-SWNTs are used to abbreviate metallic and semiconducting SWNTs, respectively.

Tight Binding Model

Zone Folding Approximation
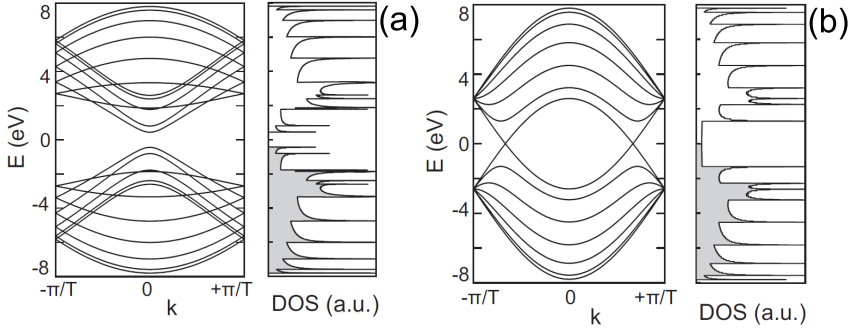
Semiconducting

Metallic

Figure 2.2: Calculated band diagram and density of states (DOS) of a semiconducting zig-zag (a) and of a metallic armchair SWNT (b). Courtesy of C. Roman.

Bandgap

An approximation for the bandgap opening in s-SWNTs is given by:

$$E_g = \frac{2\pi a_0 \gamma_0}{\sqrt{3}\left|\vec{C}_h\right|} = \frac{2 a_0 \gamma_0}{\sqrt{3}d} \approx \frac{0.75}{d}[eV].\tag{2.3}$$

$\gamma_0 = 2.6$ eV (hopping tight binding parameter for π orbitals), d is the diameter of the SWNT. From this estimation it appears that E_g of a s-SWNT scales with $\frac{1}{d}$. For a SWNT of very large diameter, E_g becomes close to zero, which is close to an unfolded graphene sheet. Fig. 2.3 shows the dependence of E_g on the SWNT diameter.

Curvature Induced Bandgap

When additionally taking into account the small curvature of SWNTs, it turns out that only SWNTs with indices (n,n) (armchair SWNTs) are truly metallic. All other other SWNTs with (n-m) mod3 = 0 feature small curvature induced bandgaps [51].

2.2 SWNT based transistors (CNFETs)

In the previous section we have seen that SWNTs can be both semiconducting and metallic depending on their structure. To experimentally characterize the electronic transport in an individual SWNT, it is typically contacted in a transistor configuration. In a SWNT based transistor (CNFET) the SWNT is located on an isolating substrate (typically SiO_2 on Si) and serves as the conductive channel between two metal electrodes, called source and drain electrodes - in analogy to standard semiconducting devices. A third electrode, called gate, is used to modulate the current through the SWNT channel. Fig. 2.4 shows a schematic of a CNFET, in which the Si substrate (highly doped) is used as back gate electrode
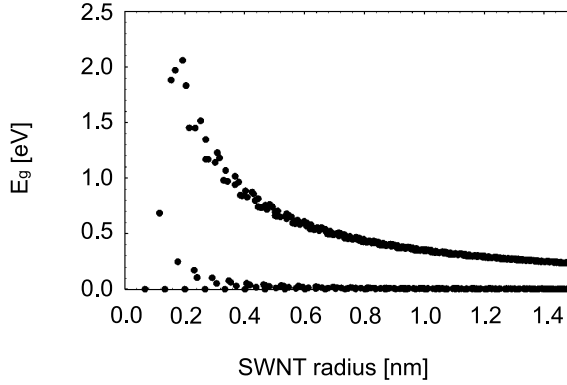
Figure 2.3: E_g for SWNTs with radii up to 1.5 nm. E_g scales with $\frac{1}{r}$. The data points at $E_g = 0$ correspond to armchair SWNTs, which are always metallic. Adapted from [50]. Copyright American Physical Society 1997.

and the SiO_2 layer acts as gate oxide.

2.2.1 Electronic transport in SWNTs

The electronic transport through an ideal 1D conductor (e.g. a m-SWNT) can be described by the Landauer formula [26]. If we assume the length of the m-SWNT to be shorter than the mean free path (l_e) and the phase relaxation length L_ϕ, then the Landauer formula gives the conductance (at low bias and temperature) as

Ideal 1D Conductor

$$G = (2e^2/h)M \qquad (2.4)$$

with $(2e^2/h) = G_0$ is called the quantum conductance and M is the number of active modes in the 1D conductor. e is the electron charge and h the Planck's constant. m-SWNTs feature two subbands close to the Fermi level E_F ($\pm$ 1 eV), as can be seen in the band diagram (Fig. 2.2) of a (6,6) armchair m-SWNT. Each subband can carry a current of $(2e^2/h)V_{sd}$ and therefore M = 2. V_{sd} is the voltage applied between the source and drain electrodes. This yields a maximum conductance for a m-SWNT of

m-SWNT

$$G = 2G_0 = 2(1/12.9k\Omega) = (1/6.5k\Omega). \qquad (2.5)$$

In an ideal and undoped s-SWNT in contrast, no conductive states are available at the charge neutrality level since it is within the band gap of the s-SWNT. At this point, the gate electrode of the CNFET structure comes into play and can be

s-SWNT

Figure 2.4: Schematic of a CN-FET. The SWNT is situated on a SiO$_2$ layer and contacted by source and drain metal electrodes. The highly doped Si substrate is used as backgate.
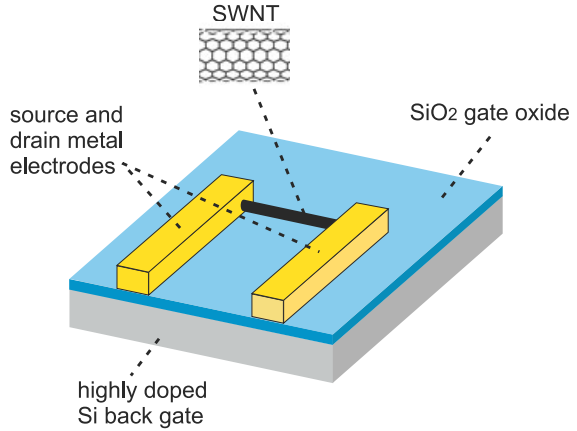

SWNT

source and drain metal electrodes

SiO2 gate oxide

highly doped Si back gate

used to move E_F into a subband, such that conduction through the s-SWNT can be observed. For $V_g < 0$, E_F is moved into the valence band and hole conductivity is observed while for $V_g > 0$ E_F is moved into the conduction band causing electron conductivity. Once E_F is moved into the valence or conduction band, G = 2G_0.

Reduced Conduction

Conduction values through SWNTs close to the theoretical limits were indeed observed in experiments [52] at cryogenic temperatures, when acoustic phonon scattering is mostly suppressed, in contrast to measurements performed at room temperature. Additionally, conduction through SWNTs below the predicted maximum value can be due to a random potential profile of the gate oxide under the SWNT due to trapped charges. In simple words, the potential landscape along the SWNT has valleys and hills through which the charge carriers have to hop [53]. Another reason for reduced conduction can be adsorbed molecules on the SWNT channel or disorder due to structural defects in the SWNT sidewall, such as heptagon-pentagon defects, vacancies or chirality changes along the SWNT [27, 54–56]. Other than effects dedicated to the SWNT channel itself that may cause reduced electrical conduction, are barriers present at the interface between the source/drain metal electrodes and the SWNT reducing the electron transfer rate.

2.2.2 Metal-SWNT contacts

Interface Barriers

In a CNFET, metal electrodes are used to electrically contact the SWNT channel. Due to lattice mismatch and differences in geometry and electrical properties (such as workfunction (WF) and effective mass) between the metal electrodes and the SWNT, interface barriers are formed [57]. These barriers can strongly influence and even dominate the overall electronic behavior of a CNFET.
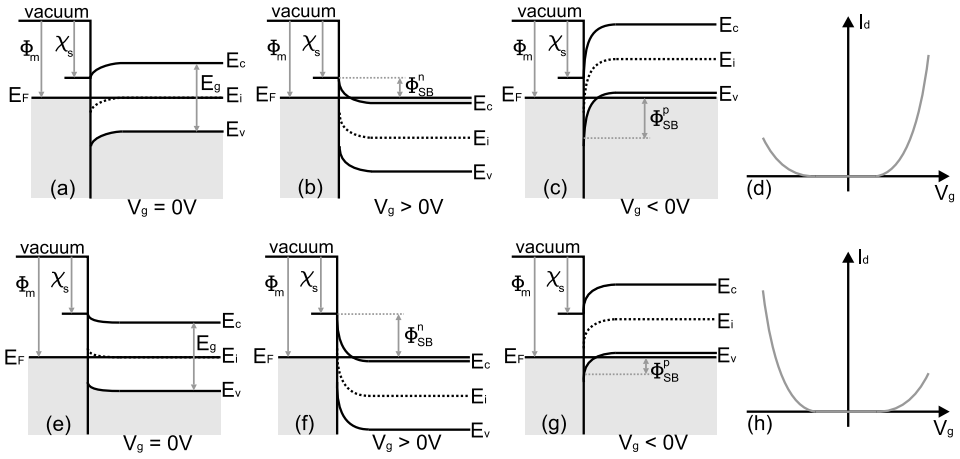
Figure 2.5: Energy diagrams at the interface between a intrinsic s-SWNT and a metal with low (a-c) and high (e-g) workfunction (WF) at different V_g. Schematic $I_d V_g$ characteristic for low (d) and high (h) WF contact metal. For a metal with low WF, $\phi_{SB}^p > \phi_{SB}^n$ and vice versa for a metal with high WF. Courtesy of C. Roman.

When a s-SWNT is contacted by metal electrodes Schottky barriers (SBs) arise at the metal-SWNT interface with depletion regions decaying within the SWNT. In contrast to planar Si devices, Fermi level pinning is believed not to be present in metal-SWNT junctions due to the non-planar shape of the SWNT [58]. As such, the contact metal with its WF strongly influences the SBs at the metal-SWNT interface. This opens the possibility of avoiding the formation of SBs for electrons or holes by choosing the appropriate metal as contact material.

Fig. 2.5(a-c) show the energy diagrams at the interface between a metal with low work function (e.g. Al, $\phi_{Al} \approx 4.2$ eV) and an intrinsic s-SWNT. ϕ_m is the metal WF ($\chi_s < \phi_m < \chi_s + E_g/2$) , χ_s is the electron affinity of the SWNT, E_F, E_i, E_v and E_c is the Fermi energy, the intrinsic Fermi energy, and the energy of the valence and conduction band edges, respectively. ϕ_{SB}^n denotes the SB for the electrons and ϕ_{SB}^p is the SB for holes. Quantum mechanical tunneling through the barrier ϕ_B is one component of the electrical transport across a metal-SWNT interface with barriers while thermionic emission (at T > 0 K) over ϕ_B is the other contribution. As such, quantum mechanical tunneling depends on the width and thermionic emission on the height of the barrier ϕ_B.

For $V_g > 0$ V the bands in the energy diagram of Fig. 2.5 (b) are moved downwards, which brings the Fermi level closer to the conduction band within the bulk of the SWNT. At the metal-SWNT interface the band edges are not moved with respect to E_F. For a contact metal with a small WF a reduced barrier ϕ_B^n results

<div style="text-align: right">Energy
Diagram

Electrical
Transport
across Barrier

$V_g > 0$ V</div>

13

for electrons while the barrier ϕ_B^p for holes is increased. Therewith, thermionic emission of electrons is increased and at the same time it is decreased for holes. Once E_c lines up with E_F, $\phi_B^n = \phi_{SB}^n = \phi_m - \chi_s$ and $\phi_B^p = E_g$. As V_g is further increased the Fermi level is moved into the conduction band and ϕ_B^n becomes thinner. At the same time, next to thermionic emission quantum mechanical tunneling of electrons also begins and the electron current through the SWNT increases.

$V_g < 0$ V For $V_g < 0$ V the situation is shown in Fig. 2.5 (c). Upon negative V_g the energy bands are moved upwards, which brings the Fermi level closer to the valence band. As a result, ϕ_B^p becomes smaller and thinner and hole conduction is dominant. Once E_v lines up with E_F $\phi_B^p = \phi_{SB}^p = E_g + \chi_s - \phi_m$ and $\phi_B^n = E_g$. For completeness, Fig. 2.5 (e), (f) and (g) show the energy diagrams for a CNFET with a high WF contact metal (e.g. Cr, $\phi_{Cr} \approx 4.5$ eV, Au or Pd , $\phi_{Au} \approx \phi_{Pd} \approx 5.1$ eV)

n-type & p-type at $V_g = 0$ V, $V_g > 0$ V and $V_g < 0$ V, respectively. For a contact metal with low WF ϕ_B^p is larger than ϕ_B^n, while for a contact metal with high WF it is vice versa. This leads to an asymmetry of the n and p current branches in the $I_d V_g$ characteristics. $I_d V_g$ characteristics, in which the electron current branch is dominant are called n-type characteristics (Fig. 2.5(d)) while characteristics with a dominant hole current branch are denoted p-type characteristics (Fig. 2.5(h)).

2.2.3 Gate hysteresis

When V_g is cycled back and forth between $+V_{g,max}$ and $-V_{g,max}$ at constant V_{sd} to record CNFET $I_d V_g$ characteristics, the forward sweep and the backward sweep typically do not lie on top of each other but are shifted by a certain value ΔV_g. This phenomenon is known as gate hysteresis and is present in most CNFET architectures. The observed hysteretic behavior has been attributed to charge trapping in the vicinity of the SWNT during the measurement of an $I_d V_g$ characteristic [31, 59, 60]. The trapped charges create an electrical potential, which acts on the SWNT channel in addition to the applied V_g: $\phi_{ext} = V_g + V_{trap}$.

Trapped charges

Electrically active trap sites for charges in CNFETs can either be present in layers of adsorbed molecules (e.g. from the ambient [60] or residuals from the fabrication process [61]) on or near the SWNT or in the underlying/surrounding oxide layers

Classical Semiconductor Physics [31, 59]. According to classical semiconductor physics [62], in a SiO_2-Si system four different classes of trapped charges are distinguished:

- *Mobile oxide charge.* Due to impurities of positive (e.g. Na^+, Li^+, K^+, H^+) or negative ions (e.g. heavy metals).

- *Oxide trapped charge.* Caused by ionizing radiation, avalanche injection of charges, Fowler-Nordheim tunneling or other mechanisms.

- *Fixed oxide charge.* Originating from the oxidation process (oxidation temperature, cooling conditions, Si orientation).

- *Interface trapped charges.* Due to structural defects, oxidation induced defects, metal impurities or other defects due to bond breaking processes (e.g. hot electron injection).

Out of these four types of trapped charges, the interface trapped charges are in electrical communication with the underlying Si substrate and can therefore be charged or discharged. So far, attempts to reduce gate hysteresis in CNFETs have been mostly based on reducing the density of charge traps around the SWNT by keeping its surroundings as clean as possible, rather than engineering the nearby oxide layers to reduce the trap density. As such, complete encapsulation of CN-FETs to avoid contamination of the SWNT channel, typically with thin layers of oxides [63] or polymers [60] have been demonstrated to reduce gate hysteresis. Another approach is based on the deposition of self-assembled monolayers (SAMs) [64], which render the device surface hydrophobic and reduce the adsorption of H_2O molecules. Recently, Muoth *et al.* [65] achieved hysteresis free CNFETs by synthesis of SWNTs between two sharp tips, followed by a shadow-mask-assisted formation of the source and drain electrodes. Avoiding any contact of the SWNT with photoresist or any other chemicals during the device fabrication is believed to reduce the density of charge traps around the SWNT [61], leading to the observed hysteresis free operation. As we will see later in the thesis, optimizing the measurement methodology to record a CNFET $I_d V_g$ characteristic has a high potential to reduce gate hysteresis.

Hysteresis Reduction in CNFETs

Charge injection

During an $I_d V_g$ measurement, V_g values in the order of several volts are applied to the gate electrode. Due to the small thickness (typically 100 nm) of the gate oxide between the gate electrode and the SWNT channel and the small radius of the SWNT (1 nm), the electrostatic field at the SWNT surface is very high. The quasi-1-dimensional shape of an SWNT, which is an important factor for the high field strength at the CNFET channel, is a fundamental difference compared to a standard MOSFET. To estimate the electric field at a SWNT of radius r separated by a distance h from the gate electrode (at the potential V_g), we can employ the following expression (wire above conductive plane)[39]:

High Electric Field Strength

$$E = \frac{V_g}{ln(h/r)\epsilon_{oxide}r} \tag{2.6}$$

Taking $V_g = V_{g,max} = 7.5$ V, h = 100 nm, r = 1 nm and $\epsilon_{oxide} = 3.9$ the dielectric constant of SiO$_2$ we obtain E = 0.417 V/nm. Following the argumentation of Fuhrer *et al.* [39] it seems plausible to assume that at such high electric field strength, charges can be emitted from the SWNT channel and can get trapped in electrically active trap sites nearby the SWNT. A widely used mechanism to describe the charge injection at high V_g from the SWNT into trap sites is based on

Fowler-Nordheim (FN) tunneling [66]. In FN tunneling the emission of electrons is induced by electromagnetic fields and as such the FN current (I_{FN}) is a function of the electric field (E) at the potential barrier between the SWNT and its surrounding (a and b are constants):

$$I_{FN} = a \cdot E^2 exp(\frac{-b}{E}). \tag{2.7}$$

Connecting the hysteretic behavior of CNFETs and the charge trapping near the SWNT channel, the schematic in Fig. 2.6 qualitatively shows the charge trapping situation (left) and the corresponding I_dV_g characteristics (right) at different V_g. The charge trapping behavior is shown in a cross sectional view of a SWNT situated on a SiO$_2$ layer and a Si substrate, which is used as backgate. Empty charge traps in the SiO$_2$ gate oxide and in a layer of adsorbed molecules around the SWNT are indicated by empty circles. The exact location of the charge traps is not taken into account in the schematic. In addition, qualitative electrical field lines are included to clarify the concept of charge screening.

An I_dV_g measurement starts by increasing V_g from 0 V toward $V_g = + V_{g,max}$. The charge traps around the SWNT are all empty (ideal condition). The electrostatic potential felt by the SWNT $\phi_{ext} = V_g$ and the current I_d in the I_dV_g characteristic is rising (Fig. 2.6(a)). As V_g is further increased and finally reaches $+ V_{g,max}$ the electric field at the SWNT surface is large enough such that electrons are emitted from the SWNT and get trapped in the charge traps nearby the SWNT. As a consequence the I_dV_g characteristic the current I_d reaches an apparent saturation, since the applied positive V_g is partially screened by the trapped electrons near the SWNT, $\phi_{ext} < V_g = V_{g,max}$ (Fig. 2.6(b)). Once V_g is swept back ($V_g > 0$ V), the trapped electrons remain in the charge traps since the natural discharging is very slow (order of minutes) [39]. Therefore, V_g sill gets partially screened by the trapped electrons, $\phi_{ext} < V_g$ and I_d decreases faster during the backward sweep than

during the forward sweep (Fig. 2.6(c)). As soon as a large enough negative V_g is applied on the gate the trapped electrons are detrapped and the traps are partially oppositely charged (Fig. 2.6(d)). Qualitatively, the same hysteretic behavior is ob-

servable for $V_g > 0$ V as for $V_g < 0$ V but with charge carriers of opposite polarity being trapped. At the end of a V_g sweep $\phi_{ext} > V_g = 0$ V due to the remaining trapped charges near the SWNT. The gate hysteresis width (H) can be extracted from the $I_d V_g$ characteristic as the difference between the forward and the backward I_d traces (Fig. 2.6(e)).

Hysteresis modeling

In order to better understand the hysteretic behavior observed in the CNFET measurements, later in the thesis we employ a gate hysteresis model, which was proposed by Robert-Peillard *et al.* [31]. The model is based on a Fowler-Nordheim injection mechanism of charges from the SWNT channel into the underlying oxide layer. More precisely, injected charges are assumed to be trapped/detrapped within a cylinder of 3 nm radius around the SWNT (inset Fig. 2.7). The model simulates the dynamics of the charge trap filling level upon applying V_g. Also in the model, the potential seen by the charge carriers in the SWNT channel is called the external potential (ϕ_{ext}) and is the sum of the applied V_g and the potential created by the filled charge traps (V_{trap}). In this model, H is directly extracted from plots of V_g versus ϕ_{ext} (Fig. 2.7). Model parameters are the sweep rate (SR) of V_g, $+V_{g,max}$, $-V_{g,max}$, the oxide thickness and its dielectric constant. For a detailed description of the model please refer to [31].

From originally continuous V_g stimuli, the model is adapted to calculate ϕ_{ext} and to extract H not only for continuously cycled V_g but also for pulsed V_g modes, which will be introduced in section 3.2.2. In the model all charge traps are distributed within a narrow cylinder around the SWNT. However, in reality the active trap states are likely to be spatially more spread. The device geometry in the model is not based an a planar but on a coaxial gate (see inset of Fig. 2.7), in which case the oxide thickness is just an effective parameter. Further, the employed Fowler-Nordheim injection characteristic may not be valid for SWNTs in all operation regions. While these limitations may prevent the model from being quantitative, it will be shown later that it behaves qualitatively correct.

Model Adaption

2.3 CNFETs as NO$_2$ gas sensors

One of most the popular device concepts for SWNT based chemical sensors are CNFETs with one or multiple SWNTs as the channel. Via electrical transport measurements through the SWNT a conductivity change upon adsorption of chemical species near or at the SWNT surface can be monitored and used as a sensor signal. Besides electrical transport measurements sensing concepts for CNT chemical sensors based on gas ionization characteristics [42], capacitive [68, 69] or
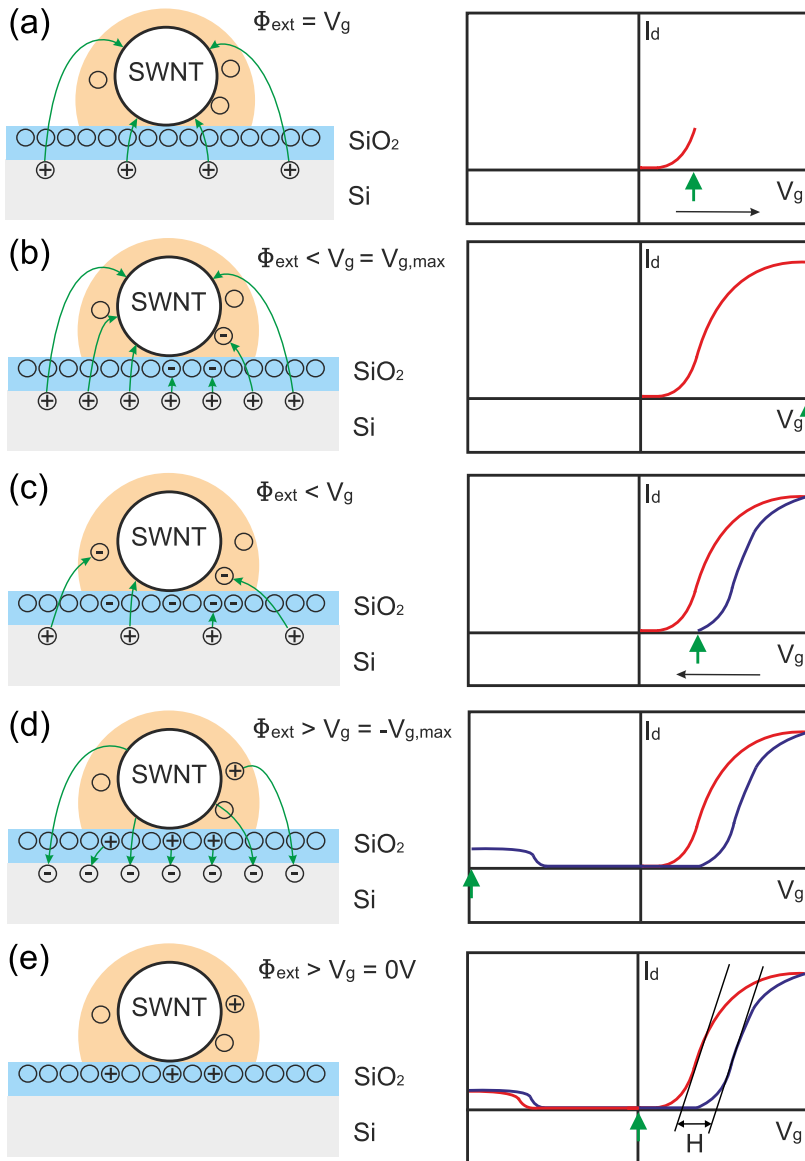
CNFET Chemical Sensors

Figure 2.6: Schematic with qualitative information about the charge trapping behavior, shown in the cross sectional views (left hand side) and the corresponding $I_d V_g$ characteristics (right hand side) at different V_g.
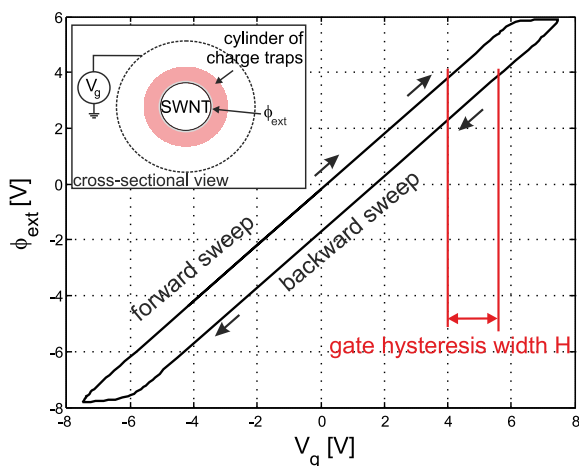
Figure 2.7: Plot of V_g versus the external potential ϕ_{ext} in steady state (potential acting on the charge carrier in the SWNT) generated with the hysteresis model. The gate hysteresis width H is extracted as the difference between the forward and backward sweep of V_g. Inset: cross-sectional view of the device geometry employed in the hysteresis model. Adapted from [67]. Copyright Institute of Physics and IOP Publishing 2010.

optical [70] readout have been demonstrated. Extensive reviews on CNTs used in (bio)chemical sensing applications can be found in [71–80].

2.3.1 SWNTs as functional material in chemical sensors

SWNTs combine several properties, which makes them highly suitable as sensitive materials used in chemical sensors. The most obvious property is probably their very high surface to volume ratio due to their hollow cylindrical structure. In fact, the surface of SWNTs is estimated to be as high as 1600 m^2/g [81]. All carbon atoms, which are incorporated in the SWNT side wall, are surface atoms and are in direct contact with the environment. Chemical species, which either physisorb or chemisorb at the large surface of SWNTs can immediately interact with the SWNT carbon atoms and do not have to diffuse into the material in order to affect bulk atoms. SWNT based chemical sensors can be operated at room temperature without additional heating, which is often inevitable in other chemical sensor concepts to increase and tune the chemical reactivity between the target analyte and the sensitive material [82, 83]. This opens the possibility to design very low power sensor devices by employing SWNTs as sensitive material. From a structural point of view strong sp^2 bonds between the carbon atoms hold the SWNT together, which render SWNTs chemically quasi-inert. As such,

Surface to Volume Ratio

Chemical Inertnes

SWNT based chemical sensors, which feature long lifetimes and can be operated in harsh environments, can be envisioned. Furthermore, due to their small size many SWNT based sensor structures can be incorporated on the same substrate, forming sensor arrays . This can help in increasing the sensor signal reliability via signal averaging and at the same time possibly reduce sensor costs.

2.3.2 NO$_2$ gas sensing mechanisms

There are two regions in CNFETs, which are proposed by simulation and experiments to be sensitive to NO$_2$, namely the SWNT-metal interface and the SWNT body. With the metal-SWNT interface SB modulation is related while the SWNT body is associated with doping or charge transfer between NO$_2$ molecules and the SWNT. There is still an ongoing debate as to which of the proposed NO$_2$ gas sensing mechanisms is dominant in CNFETs. A conclusive and universally valid answer to this question might be difficult since the fabrication process and the exact sensor architecture heavily influence the present sensing mechanisms.

Doping of the SWNT body

NO$_2$ is an electron accepting molecule. Adsorbed on the SWNT channel NO$_2$ molecules are proposed to withdraw electrons from the SWNT and as such induce hole doping [15]. A good overview on efforts spent on theoretical investigation into the interaction between SWNTs and NO$_2$ is given in [74]. Ab-initio calculations predict an electron transfer of about 0.1e per NO$_2$ molecule from the SWNT to NO$_2$ [84–86]. The charge transfer corresponds to a shift of the charge neutrality level E_F in the SWNT. In the case of adsorbed NO$_2$ it is shifted closer to the valence band (p-doping). This picture is valid for relatively low SWNT surface coverage with NO$_2$. The signature of doping is a rigid shift of the I$_d$V$_g$ characteristic, as shown in Fig. 2.8. For very high coverage of the SWNT with NO$_2$ the band structure of the SWNT can be changed. More precisely, new electrical states may become available within the bandgap or new gaps maybe induced [87].

A model to theoretically predict shifts of V_{th} in dependence of NO$_2$ concentration levels and vice versa would be a very useful tool. However, modeling results strongly depend on the properties of the actual CNFET sensor devices. First, the charge transfer between NO$_2$ molecules and SWNTs depends on the SWNT type [84–86] and has been calculated for only distinct SWNT types so far. On the experimental side, the exact SWNT type is mostly unknown due to lack of compatibility of the sensor structures to Transmission Electron Spectroscopy (TEM) to assign the SWNT chirality. Second, the actual state of the SWNTs, which is typically
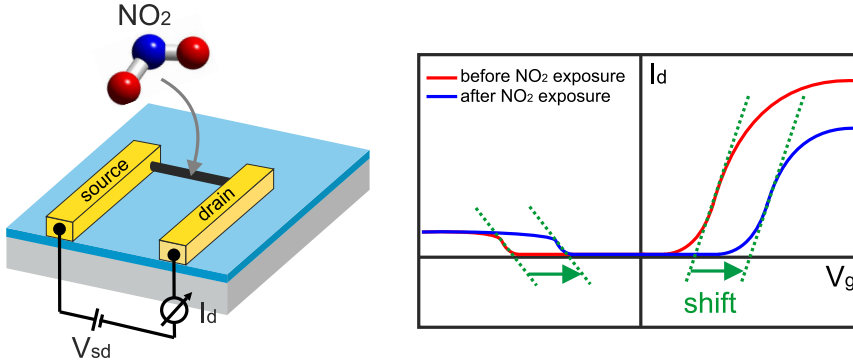
Figure 2.8: Upon adsorption of NO$_2$ molecules onto the SWNT body, charge transfer between NO$_2$ and the SWNT takes place. As a result, the Fermi level (E_F) is shifted closer to the valence band. The I$_d$V$_g$ characteristic is subject to a rigid positive shift upon NO$_2$ exposure.

unknown in experiments, is also crucial for the gas sensing properties. As such, defects in CNTs sidewalls [88–91] and processing residuals [92] (e.g. photoresist) on the CNTs were shown to impact the sensing behavior. Third, in calculations to describe the interaction of NO$_2$ and CNTs, typically short segments of CNTs are considered and the source and drain metal contacts are not taken into account. Muoth *et al.* [65] demonstrate in their study, that the actual geometry of the metal contacts heavily influences the gate capacitance along the SWNT channel. All these limitations inhibit quantitative mapping of shifts of V_{th} in dependence of NO$_2$ concentration levels and vice versa so far.

Schottky barrier modulation

The second gas sensing mechanism is related to the SWNT-metal interface. As we have seen in the section 2.2.2, the barriers for the injection of electrons (ϕ_B^n) and holes (ϕ_B^p) from the metal electrodes into the SWNT channel are dependent on the metal workfunction and the SWNT electron affinity (χ_s). NO$_2$ molecules adsorbed at the SWNT-metal interface region may modify the SBs [93]. This happens due to additional electrical dipoles induced by the adsorbed gas, which change the intensity of the pre-existing dipole at the metal surface [94]. In the case of NO$_2$ gas adsorption the barrier heights at the contacts are reduced for holes and increased for electrons. As a result, the current I_d of the n-branch in an I$_d$V$_g$ characteristic decreases while the p-branch increases. The I$_d$V$_g$ characteristic seems to be subject to a rotation, which is the signature of SB modulation [95], as shown in Fig. 2.9.
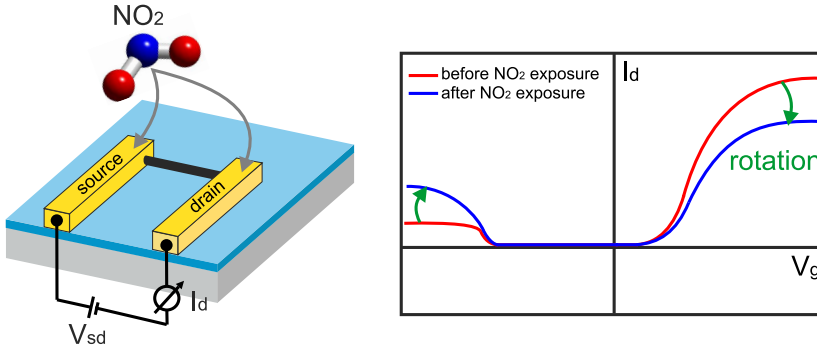
Figure 2.9: Upon adsorption of NO_2 molecules on the metal-SWNT interface region, the metal workfunction is changed. As a result, the barrier heights at the contacts are reduced for holes and increased for electrons. The current I_d of the n-branch in a I_dV_g characteristic decreases while the p-branch increases.

2.3.3 State-of-the art

In this subsection a short state-of-the-art overview, dedicated to CNFET based NO_2 gas sensors, is presented. Three different classes of CNFETs are discussed in the following: First, CNFETs with pristine SWNT channels, second, with chemically functionalized SWNT channels and third, partially passivated CNFETs.

Typically, CNFET chemical sensors can be operated in two modes:

- ChemFET. The sensor signal is extracted from I_dV_g characteristics, which are recorded by applying a constant V_{sd} bias, cycling V_g between $\pm\, V_{g,\text{max}}$, while the current I_d is monitored. The gate threshold voltage (V_{th}) is typically used as the sensor signal extracted from I_dV_g characteristics.

- ChemiResistor. At constant V_{sd} bias the current I_d is continuously monitored and used as the sensor signal at a fixed V_g (typically $V_g = 0$ V). This operation mode is often used to acquire a transient sensor signal.

Pristine SWNTs

Individual SWNT

The first CNFET employed as chemical sensor for NO_2 gas detection was presented by Kong *et al.* [15] in 2000. Their CNFET architecture was based on an individual s-SWNT as the channel, in-situ grown on SiO_2/Si substrates. Upon exposure to 200 ppm of NO_2 at toom temperature (RT) they observed a positive shift of V_{th} of several volts in the I_dV_g characteristic. They attributed the observed shift to charge transfer between NO_2 and the SWNT channel. The smallest

NO$_2$ concentration detected in this study was 2 ppm. Upon heat treatment at 200 °C for 1 h in air the sensor was recovered. Sensor recovery at RT was slower than in the heated case and took about 12 h. This first publication on CNFETs employed as chemical sensors has been cited so far more than 2300 times (winter 2011). It can be seen as the cornerstone for a huge number of continuative studies for CNFETs employed as chemical sensors. Since then, several specific aspects of a CNFET as chemical sensor have been experimentally and theoretically investigated, e.g. the role of defects in CNTs on their gas sensing properties [88–91], the influence of the SiO$_2$ underneath a SWNT on the NO$_2$ gas sensing behavior [96] , the effect of SWNT growth conditions on the final gas sensitivity [97], or the influence of contamination in SWNTs on the interaction with gases [92] to name just a few studies. Besides CNFETs with individual SWNTs as channel, devices with thin films of SWNTs contacted by (interdigitated) electrodes have also been demonstrated. Such devices are often operated in the ChemiResistor mode and do not show a pure semiconducting $I_d V_g$ characteristic due metallic SWNTs present in the SWNT thin film. As the gas sensitive surface is considerably higher in devices based on a SWNT thin films than in a CNFET based on an individual SWNT, they usally feature a lower limit of detection (LOD). Li *et al.* [98] demonstrated detection of 44 ppb of NO$_2$ with a device based on a cast SWNT thin film between interdigitated electrodes. The sensor was operated as ChemiResistor and showed fast NO$_2$ detection within seconds and recovery within minutes at RT.

SWNT Thin Film

Functionalized SWNTs

In addition to CNFETs with pristine SWNT channels, many studies have been performed in which the SWNT channels are chemically functionalized. Chemical modification of the SWNT can help to improve the sensors' sensitivity and selectivity to the target analyte. Also in the case of NO$_2$, several materials deposited onto SWNTs have been shown to improve the sensing performance. Qi *et al.* [99] fabricated arrays of SWNTs bridging across prefabricated metal electrodes. Then they coated the sensor surface with the polymer polyethyleneimine (PEI) by immersing the device in a PEI/methanol solution. After heat treatment to evaporate the solvent, the sensors were exposed to NO$_2$ and a concentration less than 1 ppb (parts-per-billion) of NO$_2$ was detectable. Since the PEI coating makes the SWNT electron rich it enhances the binding affinity for the electron-withdrawing NO$_2$. On the other hand, functionalizing the SWNT surface with nafion Qi *et al.* observed that the sensitivity to NO$_2$ was blocked, which enabled the possibility to detect other gases more selectively, e.g. NH$_3$. Other groups [100–102] decorated their CNT devices with metal nano particles. Due to the differences in catalytic

Polymers

Metal Nano Particles

activity of different metals, nanoparticles can help to improve the sensor selectivity.

Partially passivated CNFETS

In CNFETs employed as chemical sensors, it might be helpful to use passivation layers to protect delicate parts of the CNFETs (e.g. metal contacts) from corrosive environments. In addition, by shielding and exposing only distinct parts of CNFETs, information about the sensing mechanisms for NO_2 sensing might be gained and the sensor architecture can be optimized accordingly. So far, experiments to elucidate the dominant (NO_2) chemical sensing mechanisms led to rather inconclusive results [93, 103–105]. Zhang *et al.* [93] investigated CNFETs partially passivated with a thick layer of polymethylmethacrylate (PMMA) and SU8 for NO_2 detection and found chemical modifications at the interface between the CNT and the electrodes to be responsible for NO_2 sensing. In contrast, by using CNFETs partially passivated with silicon monoxide (SiO), Bradley *et al.* [103] found that NH_3 rather affects the CNFET channel than the contact-CNT interfaces. Heller *et al.* [104] performed a study on identifying the mechanism of biosensing with CNFETs partially passivated with PMMA. They found the majority of their experiments to be explainable by effects occurring at both the contact-CNT interfaces and the CNFET channel. While PMMA can be easily spin coated onto substrates and is affected by heat, oxides and nitrides are deposited in more complex and expensive processes such as atomic layer deposition (ALD) or sputtering but are thermally stable up to several hundred degrees Celsius. Concerning the sealing properties, PMMA and silicon monoxide were reported to be permeable for gaseous species [93, 103], while passivation layers for CNFETs made of aluminum oxide or silicon nitride are known to lead to air-stable devices [63, 106, 107].

Summary

The table in Fig. 2.10 contains representative examples of CNFET NO_2 sensors with pristine and chemically functionalized SWNTs and CNFETs with (partial) passivation layers. It contains sensor key characteristics, such as the employed CNT type, sensor operation mode, target analyte(s), limit of detection (LOD), response time and sensor reversibility. From this listing we can summarize what NO_2 sensing performance can be expected with CNFETs sensor technology. For CNFETs with pristine SWNT channels a minimum LOD of about 44 ppb NO_2 and a response time in the range of 600 s is reported while for CNFETs with chemically functionalized SWNT channels much lower LOD of 1 ppb NO_2 with response times between 60 and 120 s was shown. The sensors can all be recovered by heat

LOD &
Response Time

24

treatment within a time in the order of 1 h or non specified UV exposure time. The power consumption of the CNFET during NO$_2$ sensing is not mentioned in the respective studies. However, considering typical V_{sd} bias values in the order of 100 mV and observed I_d current levels of several μA, we obtain a typical power consumption in order of 1 μW (without heating during sensor recovery phase). For CNFETs based on SWNT thin films the power consumption might be slightly higher due to the higher electrical conductance compared to one individual SWNT as channel.

Power Consumption

CNT type	Operation mode	Chemical Functionalization	Passivation material	Passivation configuration	Target analyte	Limit of detection (LOD)*	Response time [s]	Reversibility	Reference
SWNT	ChemFET ChemiResistor	-	-	-	NO2, NH3	2 ppm (NO2)	<600	yes (heating @ 200 °C)	Kong et al.
SWNT	ChemFET ChemiResistor	-	-	-	NO2	180 ppm	120 - 960	yes (heating @ 120 °C, UV)	Helbling et al.
SWNT	ChemFET ChemiResistor	-	-	-	NO2	6 ppm	960 - 1800	yes (heating @ 120 °C, UV)	Helbling et al.
SWNT	ChemFET	-	Aluminum oxide	FP, CP	NO2	100 ppb	minutes	Yes (heating @ 110 °C)	this work
SWNTs	ChemiResistor	-	-	-	NO2, Nitrotoluene	44 ppb (NO2)	600	yes (UV)	Li et al.
SWNTs	ChemFET / ChemiResistor	PEI, Nafion	-	-	NO2, NH3	1 ppb (NO2)	60-120	yes (UV)	Qi et al.
SWNTs	ChemFET	Polypyrrole	-	-	NO2	N/S	600-1800	yes	An et al.
SWNTs	Chemiresistor	PABS	-	-	NH3, NO2, H2O	20 ppb (NO2)	600	yes	Zhang et al.
SWNTs	Chemiresistor	Au	-	-	NO2	4.6 ppb	N/S	yes (UV)	Young et al.
SWNT	ChemFET	-	Polymethylmethacrylate (PMMA)	FP, CP	NO2	N/S	N/S	yes (heating @ 100°C)	Zhang et al.
SWNT	ChemFET	-	Polymethylmethacrylate (PMMA)	CP, CHP	NO2, NH3	0.5 ppm (NO2)	N/S	yes	Liu et al.
SWNTs	Chemiresistor	-	Silicon monoxide	FP, CP	NH3	N/S	N/S	N/S	Bradley et al.
SWNT	FET	-	Aluminum oxide	FP	-	-	-	-	Kim et al.
SWNT	FET	-	Silicon nitride	FP	-	-	-	-	Kaminishi et al.
SWNT	FET	-	Silicon nitride	CP	-	-	-	-	Peng et al.

Figure 2.10: Listing of representative examples of CNFET NO$_2$ sensors with pristine and functionalized SWNT channels and partially passivated devices. Abbreviations: FP - fully passivated, CP - contact passivated, CHP - channel passivated. * Note: In some studies the limit of detection (LOD) is not explicitly reported. In such case the lowest NO$_2$ concentration tested is listed.

2.3.4 Comparison with commercial off-the-shelf NO$_2$ sensors

When looking for NO$_2$ gas sensing technologies other than CNFETs, we find a large number of different sensor working principles and applied sensitive materials. Gas chromatography and optical detection are usually very sensitive but at the same time also very expensive methods and involve bulky equipment [108]. NO$_2$ detection based on nanowires of different materials [109–113] and surface acoustic waves (SAW) sensors [114, 115] is still in its exploratory state and has not been commercialized yet. Instead, commercially off-the-shelf (COTS) available discrete NO$_2$ gas sensors are conductometric sensors based on metal oxides [13, 14] and amperometric gas sensors (electrochemical cells) [10–13]. In Fig. 2.11 a small selection of commercially available NO$_2$ sensors of different manufacturers is shown. The sensor parameters are taken from the respective sensor datasheets. Compared to the CNFET NO$_2$ sensors listed in Fig. 2.10 more sensor specifications are given for the commercial sensors as they are characterized in more detail. A good comparison of CNT based chemical sensors to commercially available chemical sensors can be found in [74].

In amperometric gas sensors, NO$_2$ molecules enter the sensor cell via a diffusion barrier and are electrochemically reduced at the first electrode. Then they move across the electrolyte and reach the second electrode, where they re-oxidize. This results is a small electrical current between the electrodes, which is proportional to the NO$_2$ gas concentration and is used as the sensor output signal [116, 117]. A major issue with this type of sensor is its limited lifetime, which is specified to be at most 24 months due to the consumption of the metal electrode during sensor operation [118]. Depending on the employed sensor model different NO$_2$ sensing ranges up to hundreds of ppm can be covered, as seen from Fig. 2.11. In conductometric sensors, as NO$_2$ molecules reach the metal oxide surface (e.g. SnO$_2$, ZnO, WO$_3$, Fe$_2$O$_3$, TiO$_2$ [9]) they react with the oxygen at the metal oxide surface, reducing the electrical conductivity of the sensitive layer since NO$_2$ is a electron acceptor. The conductivity change upon NO$_2$ adsorption is proportional to the NO$_2$ concentration and employed as the sensor signal. The reactivity and the diffusion of the gas molecules into the sensitive material is typically controlled by heating the sensors [119]. This type of sensors usually has a long lifespan of several years but suffers from high power consumption in the order of tens of mW due to the sensor heating.

From this short performance overview of COTS NO$_2$ sensors it appears that CNFET NO$_2$ sensors have a high potential to combine the advantages and at the same time avoid the disadvantages of both metal oxide and electrochemical sensors. First, improved lifetime can be expected from CNFETs compared to electro-

Electro-chemial Cells

Metal Oxide based Sensors

Conclusion

chemical sensors due to the intrinsic stable structure of SWNTs. Second, reduced power consumption by orders of magnitude compared to heated metal oxide sensors can be envisioned since CNFETs can be operated at RT. The NO_2 sensitivity range is comparable for both CNFETs and COTS NO_2 sensors. The response time of CNFETs with pristine SWNT channels are about 10 times longer than those of COTS sensors but by using chemical functionalization the response time of CN-FETs can also be reduced to about 1 minute, as seen in the study of Qi *et al.* [99].

	NO2-A1	NO2-AE	A3OZ EnviroceL	NO2 – 68 09 655	EC4-20-NO2	MiCS-2710	AS-MLN
Manufacturer	Alphasense	Alphasense	City Tech	Dräger	e2v Tech	e2v Tech	Applied Sensor
Working principle	Electrochemical	Electrochemical	Electrochemical	Electrochemical	Electrochemical	Metal oxide	Metal oxide
Sensing range	0 - 20 ppm	0 – 200 ppm	0 - 10 ppm	0.3 – 10 ppm	0 – 20 ppm	0.05 – 5ppm	0.1 – 2 ppm
Resolution	< 0.02 ppm	< 0.1 ppm	0.02 ppm	0.1 ppm	0.1 ppm	N/S	N/S
Response time t_{90}	< 40 s (10 ppm)	< 25 s (10 ppm)	< 40 s	< 15 s (t_{63})	< 35 s	N/S	seconds
Temperature range [°C]	-20 to 50	-20 to 50	-20 to 50	-40 to 65	-20 to 50	-30 to 85	-40 to 120
Humidity range [% r.h.]	15 - 90	15 - 90	15 - 90	5 - 95	15 - 90	15 - 90	0 - 95
Power consumption [mW]	N/A	N/A	N/A	N/A	N/A	43	35
Sensor lifetime	24 months	24 months	24 months	18 months	24 months	N/S	years

Figure 2.11: Listing of commercially-off-the-shelf (COTS) available NO$_2$ sensors.

3 Methodology

3.1 CNFET sensor fabrication process

The entire fabrication process of the CNFET gas sensors is conducted in the clean-room laboratories FIRST-Hönggerberg and FIRST-CLA of ETH Zurich. The fabrication process is based on many little process steps, which were developed and further improved by two generations of PhD students [17–19] of the MNS group. With specific adjustments and enhancements the process fabrication flow was then adapted in this project for the fabrication of CNFET based gas sensors. A detailed description of the applied SWNT growth process can be found in [20, 120, 121]. In appendix A the detailed run sheet of the fabrication process is given.

3.1.1 Substrate preparation

Starting point for the fabrication of the sensors is a 4-inch wafer of highly p-doped silicon of 625 μm thickness with a 200 nm (first generation) and 100 nm (second generation) thick thermally grown SiO_2 on top (grown in the clean room facilities at Ecole Polytechnique Fédéral de Lausanne (EPFL)). By means of an ESEC 8003 dicing saw a pattern of 6 $\times$ 6 mm^2 squares is halfway cut (cutting depth 300 μm) into the wafer. During the dicing procedure the top surface with the SiO_2 is protected by a layer of AZ4533 photoresist from dust and debris. The wafer is then carefully broken along the cuts into chips of 12 $\times$ 12 mm size. By processing 12 $\times$ 12 mm chips four 6 $\times$ 6 mm chips are processed in parallel, which reduces fabrication time. At the very end of the fabrication process each 12 $\times$ 12 mm chip is further broken along the cuts into 6 $\times$ 6 mm final chip size, see Fig. 3.1. After the dicing procedure the protective layer of photoresist is removed and the chips are cleaned in solvent baths in the order of acetone, 1-Methyl-2-pyrrolidone (NMP), acetone and isopropanol (IPA). Finally the chips are blow dried with N_2. Note that the solvent cleaning of the 12 $\times$ 12 mm chips should not be assisted by ultrasonic treatment since this can break the halfway cut chips.
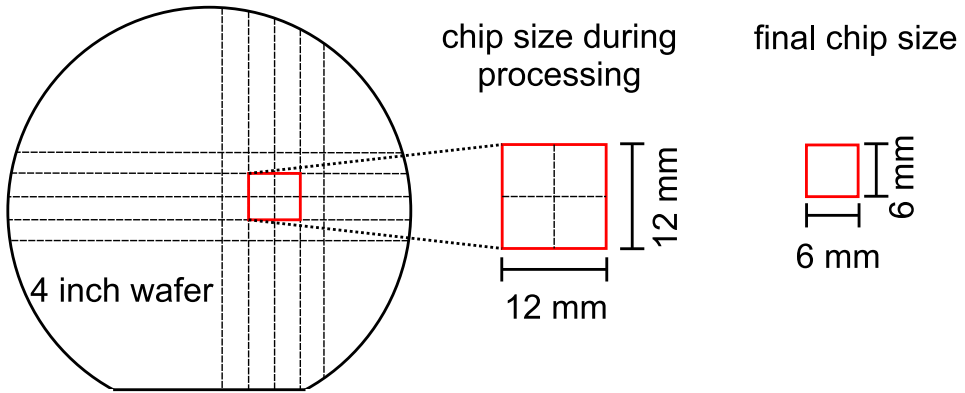
Figure 3.1: Illustration of the wafer dicing process and the two different chip sizes.

3.1.2 Catalyst particle adsorption and SWNT synthesis

Individual SWNTs are synthesized on the highly doped silicon substrate SiO_2 layer from Ferritin-based iron catalyst nanoparticles in a low pressure chemical vapor deposition (LPCVD) process. Ferritin is a protein, which can store iron ions in its core [122, 123] and therefore can serve as shell to form nanoparticles with very narrow diameter distributions [124]. The detailed description of the preparation of a Ferritin catalyst solution can by found in [20].

Iron loaded Ferritin proteins are adsorbed onto the SiO_2 by fully covering a chip with Ferritin catalyst solution for 1 min. Then, the chip is dipped into DI water for 1 min to stop the adsorption process. The Ferritin catalyst particles are then calcined on a hot plate at T > 600 °C in ambient air for 5 min, which leaves iron oxide particles on the chips, see Fig. 3.2

The density of adsorbed catalyst particles on the substrate to obtain the desired density of SWNTs (about 10 SWNTs on $(50\ \mu m)^2$) has to be adjusted for every Ferritin solution before every SWNT growth run.

Before SWNT synthesis is started, the LPCVD reactor is pumped below 10^{-5} bar and the iron oxide particles are reduced in H_2 (at 370 mbar) for 10 min. SWNT growth is then performed by injecting 60 mbar H_2 and then increasing the pressure to 217 mbar by injecting CH_4 at a temperature of 850 °C for 15 min. Fig. 3.3 shows grown SWNT(s) on the substrate.
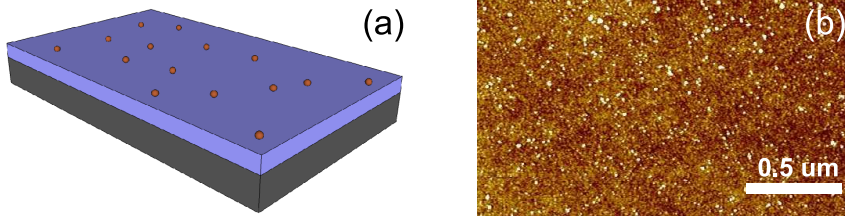
Figure 3.2: 3D illustration (a) and AFM scan (b) of adsorbed Ferritin based catalyst nano particles on the substrate.
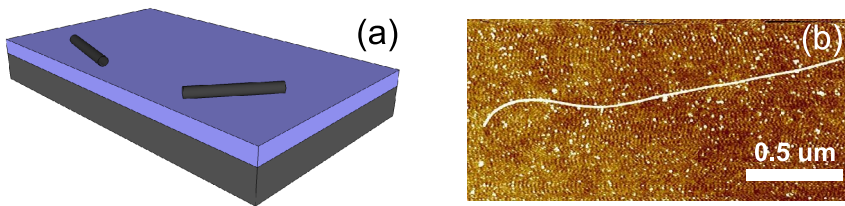
Figure 3.3: 3D illustration (a) and AFM scan (b) of grown SWNT(s) on the substrate.

3.1.3 Bond pad formation

In order to later electrically connect the CNFET devices with the measurement equipment, metal bonding pads are formed, as seen in Fig. 3.4 This is done by standard photolithography, subsequent physical vapor deposition (PVD) of Cr and Au (2 and 40 nm) in a Leybold Univex 500 and metal liftoff. For the liftoff, the chips are immersed in hot NMP at 50 °C for at least 12 hours followed by rinsing in acetone (10 min) and IPA (5 min) and N_2 drying.

Figure 3.4: 3D illustration (a) and microscopic image (b) of the bond pads.

Figure 3.5: 3D illustration (a) and microscopic image (b) of the marker structures, which are used as reference to locate the SWNTs.

3.1.4 AFM marker formation

In order to be able to locate and later electrically contact the randomly grown SWNTs on the chip, metal markers serving as re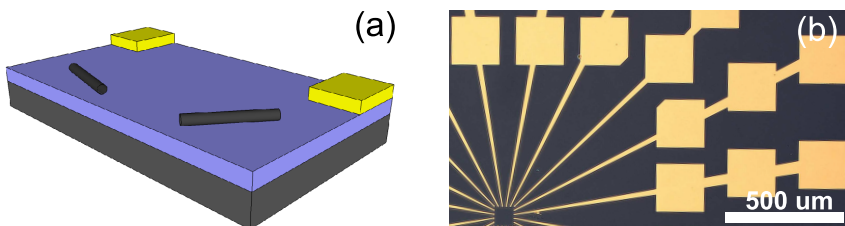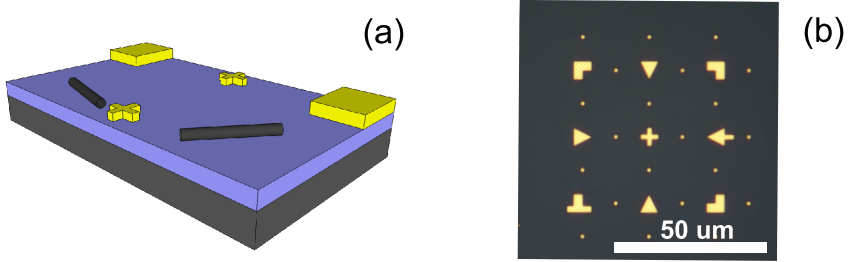ference structures are deposited (Fig. 3.5). The markers need to be well defined in size and shape and are therefore formed by electron (e-beam) lithography (Raith 150), subsequent PVD of Cr and Au (2 and 40 nm) and metal liftoff. A good liftoff profile with e-beam lithography can be achieved by spin coating a double layer of resist onto the chip: a layer of the copolymer methyl methacrylate and methacrylic acid (P(MMA/MAA)) with a molecular weight of 950K (1:1) in ethyllactate, followed by a layer of polymethyl methacrylate (PMMA) 950K (1:1) in chlorobenzene. Each layer is individually prebaked at 180 °C for 15 min to remove the solvents. The markers structures are exposed with an e-beam area dose of 450 $\mu C/cm^2$ and developed in methyl isobutyl ketone (MIBK):IPA (1:3) for 1 min, then immersed in IPA for 1 min to stop the development and N_2 blow dried.

3.1.5 SWNT location and selection by AFM

The randomly grown SWNTs are located on the chip by atomic force microscopy (AFM) (MFP-3D from Asylum Research). AFM scanning is a rather slow imaging methodology (tapping mode with 20 μm/s scan speed) but it gives a precise map of the SWNTs and the metal markers revealing the SWNTs' location, orientation and diameter information. For reliable SWNT localization an AFM scan of (10 μm)^2 requires a resolution of about 1000 scan points and lines. The MFP-3D allows 4092 scan points and lines at the maximum per single scan. However, the midsection of the chip, where the AFM markers are located, is (50 μm)^2 in size. Since we can not cover the midsection of the chip by a single scan, we perform four AFM scans of (30 μm)^2 with 3072 scan points and lines with 2 μm overlap to reach the required resolution. The four AFM scans are automatically performed
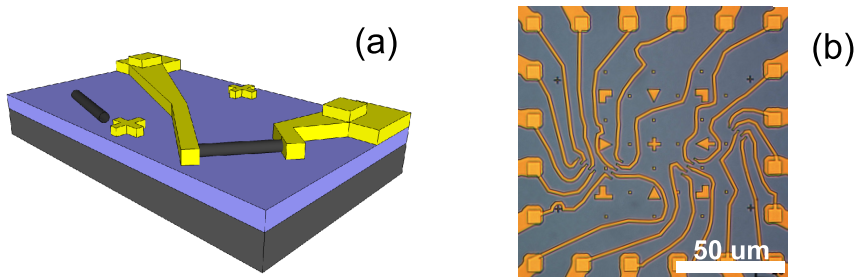
Figure 3.6: 3D illustration (a) and microscopic image (b) of the metal leads, which electrically contact the SWNTs.

by a script.

By analyzing the AFM scans with Image Metrology's SPIP, suitable SWNTs for the CNFET sensors are selected. Selection criteria are: Diameter between 2 and 2.5 nm, clear separation from other SWNTs to allow reliable electrical contacting and straightness to achieve repeatable SWNT channel lengths.

3.1.6 Electrical contact formation

Based on the AFM map the source and drain metal leads of the CNFET sensors are formed by e-beam lithography, subsequent PVD of Cr and Au (2 and 40 nm) and metal liftoff. The AFM scan with the SWNTs and the AFM markers are overlaid with the marker template in CorelDraw software. Then, the previously selected individual SWNTs with suitable length, orientation and diameter are transfered into the marker template. The modified marker template with the drawn SWNTs is then imported into a CAD software (Tanner L-Edit), where the source and drain contacts are added and finally exported as GDS-II file for the e-beam lithography. The electrical contacts are exposed with an e-beam area dose of 450 $\mu C/cm^2$ and developed in methyl isobutyl ketone (MIBK):IPA (1:3) for 1 min, then immersed in IPA for 1 min to stop the development and N_2 blow dried. A SWNT with electrical contacts is shown in Fig. 3.6.

3.1.7 ALD Al$_2$O$_3$ passivation

Immediately after the liftoff of the electrical contacts, the CNFET devices are passivated with 40 nm of atomic layer deposited (ALD) Al_2O_3 [125–127]. The Al_2O_3 deposition takes place in a Picosun Sunale R-150B reactor at 150 °C with water and trimethylaluminum (TMA) as alternately injected precursors and N_2 as purge gas. The SiO_2 surface features hydroxyl groups, which react with the first injected pre-
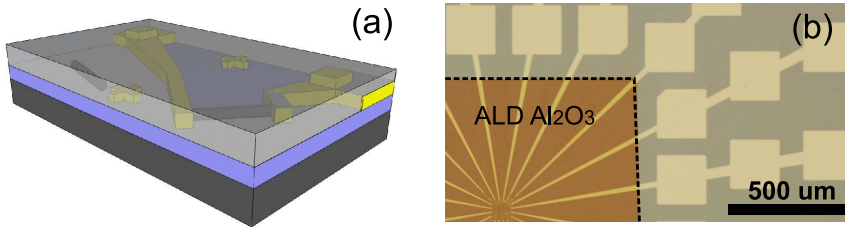
Figure 3.7: 3D illustration (a) and microscopic image (b) of the sensor chip with deposited layer of ALD Al$_2$O$_3$.

cursor TMA. After exposure to water, acting as the second precursor, new hydroxyl groups are formed, reacting with the TMA in the next cycle. After 460 cycles of alternating precursor exposure an ALD Al$_2$O$_3$ of about 37 nm is formed (characterized by ellipsometry).

After the ALD process the entire chip, including the bond pads, is covered with Al$_2$O$_3$. However, for a reliable wire bonding process the Al$_2$O$_3$ layer has to be removed from the bond pads. This is done by etching the Al$_2$O$_3$ away in 6 % buffered hydrofluoric acid (BHF) for 20 s while the Al$_2$O$_3$ layer at the middle section of the chip is protected by a mesa of AZ4533 photoresist.

3.1.8 Window etching

In order to provide access for the target analyte to the gas sensitive SWNT channel, a well-defined rectangular opening of size 0.5 μm $\times$ 1 μm is etched into the passivation layer between the metal contacts with 6 % BHF through an e-beam-structured polymer etch mask. The etch mask consists of a spin coated 100 nm thick layer of pure P(MMA/MAA) 950K. The windows are exposed with an e-beam area dose of 180 μC/cm^2 and developed in methyl isobutyl ketone (MIBK):IPA (1:3) for 1 min, then immersed in IPA for 1 min to stop the development and N$_2$ blow dried. After development the etch mask is baked at 150 °C for 2 min to harden it and improve its adhesion to the SiO$_2$, especially at the edges of the developed windows. Under constant movement of the chip in BHF the windows are etched into the Al$_2$O$_3$ layer within 20 to 25 s. After etching the chip, it is immediately rinsed in turbulent DI water for 5 min. The etch mask is stripped in hot NMP (at 50 °C) for 10 min, acetone for 10 min and IPA for 5 min and finally dried with N$_2$. The final device is shown in Fig. 3.8.
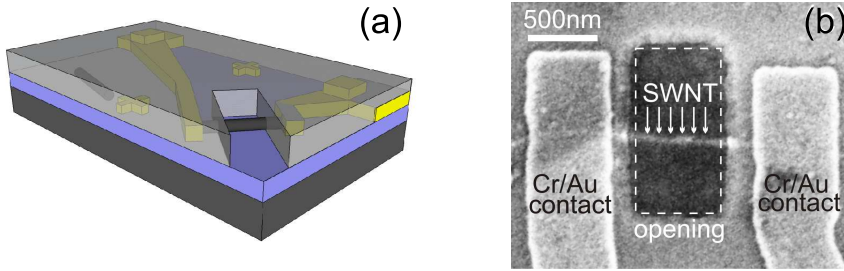
Figure 3.8: 3D illustration (a) and scanning electrode microscopy (SEM) image (b) of a final CNFET sensor, with a window etched into the Al_2O_3 passivation layer above the SWNT channel.

3.1.9 Die- and wire bonding

At this state of the fabrication process the 12×12 mm^2 chips are broken along the cuts into 6×6 mm^2 pieces, which are bonded into ceramic packages. The ceramic package is cleaned in acetone and then IPA for 5 min each and dried with N$_2$. A small drop of photoresist AZ4533 is placed into the package and the excess photoresist is soaked up with a clean room swab. Then the 6×6 mm^2 chip is placed onto the photoresist drop and gently positioned in the middle of the package. After baking the package with the chip for 2 min at 110 °C the photoresist has hardened and the chip is glued into the package. The advantage of using photoresist for die bonding instead of using a glue is that the photoresist can easily be dissolved again by solvents, such as NMP or acetone, and thereby the chip can be removed from the package. This way, the very same chip can be electrically characterized at different stages of the fabrication process.

The wire bonding is performed with a Delvotec FEK 5425 wedge-wedge wire bonder. The wire used is an Al wire of 30 μm diameter. The bonding parameters, especially the bonding force, the ultrasonic power and the ultrasonic time are rather critical. On one hand choosing high values for these parameters leads to strong and reliable bonds between the wire and the pads on the chip. On the other hand if these parameter values are chosen too high, the thin SiO$_2$ layer might be penetrated, causing electrical shortening of the pads and the highly doped Si substrate, which is used as back gate electrode. In order to electrically connect the back gate, wire bonds are made to the edge of the chips, where no gate oxide but only thin native oxide is present. By slightly increasing the aforementioned critical bonding parameters strong and reliable bonds can be made to the Si back gate electrode.

A schematic view of the final CNFET chemical sensor structure and a microscope image of a sensor chip bondend into a package are shown in Fig. 3.9. While
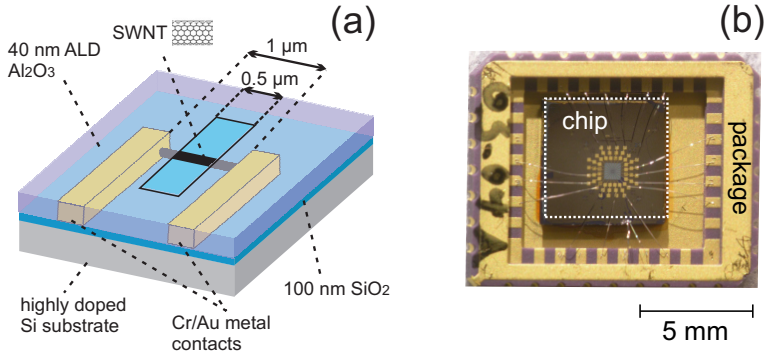
Figure 3.9: Schematic view (a) of the final CNFET chemical sensor structure and a microscope image (b) of a sensor chip bondend into a package.

the gas sensitive CNT channel is exposed to ambient, the degradation-prone metal contacts are passivated by a thin layer of ALD Al_2O_3.

3.2 CNFET electrical characterization

In this section the measurement setup for the electrical characterization of the CNFET devices and its different operation modes is presented. It is a home-built setup, which offers great expandability to implement and automate experiments. The signal generation and acquisition is performed by means of a National Instruments Data Acquisition Card (NI DAQ) and the measurement setup is based on only a few external components. This makes it very compact and easily transportable, which is important since the CNFET characterization in NO_2 gas are performed at Siemens AG in Munich.

3.2.1 Measurement setup

For electrical characterization of the CNFET devices gate characteristics are recorded: A constant voltage bias (V_{sd}) is applied to the source and drain metal contacts. The gate voltage (V_g) is applied to the highly doped silicon substrate, serving as back gate electrode and is cycled from 0 V to $+V_{g,max}$, then to $-V_{g,max}$ and back to 0 V. A LabView-controlled National Instruments DAQ card (NI PCI-6289) is used to generate V_{sd} (additionally lowpass filtered, $f_c = 7$ Hz) and V_g. At the drain contact of the CNFET, I_d is amplified (typically $G = 10^6$) by a high bandwidth, low noise current-to-voltage amplifier (Femto DHPCA 100) and fed back to the DAQ card. Immediately after the CNFET measurements all electrical
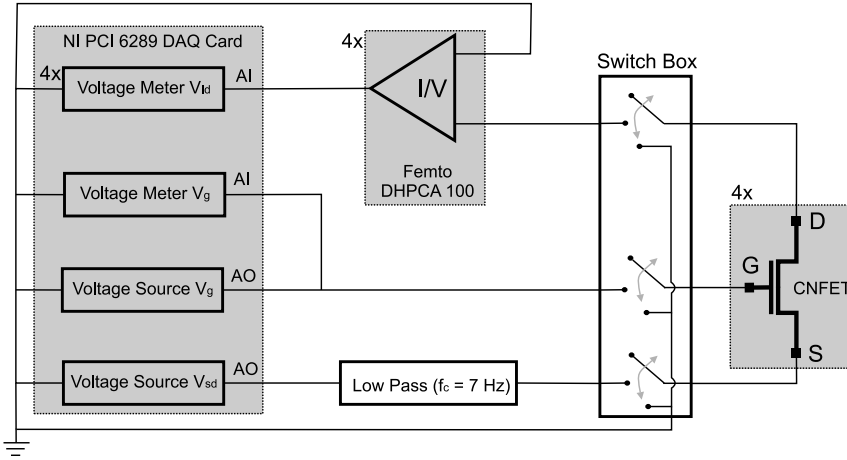
Figure 3.10: Schematic of the used measurement setup for the electrical characterization of the CNFETs. V_{sd} and V_g are generated on the DAQ card. I_d is amplified by low noise current-to-voltage converter and also acquired by the DAQ card.

connections to the measurement setup can be put to ground potential by a switch box. This is necessary to avoid electrostatic discharge when changing the electrical connections between different CNFET devices. The schematic of the electrical measurement setup is shown in Fig. 3.10. In addition, the setup features four amplifiers and input channels and can therefore record the output current I_d from four different CNFETs at the same time. This feature improves the efficiency of the experiments, especially for long gas adsorption and desorption experiments. Immediately after each measurement the recorded data is displayed in the LabView measurement software and stored in text files for further processing. A detailed description of the LabView program can be found in [128].

3.2.2 V_g strategies

The measurement setup can be operated in three different V_g modes:

- Continuous mode: V_g is incremented and decremented in small steps, which leads to a quasi-continuous voltage sweep, as shown in Fig. 3.11(a);

- Pulsed p++ mode: V_g is a sequence of short voltage pulses of the same duration but varying amplitude. The pulses of the same polarity are part of the same half of the V_g waveform period, as shown in Fig. 3.11(b);

- Pulsed p+- mode: V_g is essentially applied as in the p++ mode but with each

positive voltage pulse being followed by a pulse of equal amplitude and duration but negative polarity, as shown in Fig. 3.11(c).

For both pulsed measurement modes p++ and p+- V_g is returned to 0 V for 100 μs (t_{low}) between two consecutive voltage pulses of duration t_{high}. I_d is measured shortly before the end of every voltage pulse (t_{acq} = 90 % t_{high}).

3.3 NO$_2$ exposure

3.3.1 Gas mixing setup

The characterization of the CNFET sensors in NO$_2$ gas is performed at Siemens AG in Munich with their custom-built gas mixing setup. A schematic of the gas mixing setup is shown in Fig. 3.12. The gases are stored in large gas cylinders. The carrier gas in our case is synthetic dry air, a mixture of oxygen (O$_2$) and nitrogen (N$_2$), which is mixed in the ratio 2:8 according to the standard atmospheric gas composition. The desired concentration of nitrogen dioxide (NO$_2$) gas is added to the carrier gas and gets mixed with the carrier gas in a collective gas line. The exact amounts of the respective gases are controlled by computer controlled mass flow controllers (MFCs), which are calibrated for the respective gases. In front of and after each MFC there are pneumatic valves to open or close individual gas lines. In order to add humidity to the gas mixture, a sideline of the N$_2$ gas line, which is also controlled by a MFC, is guided through a heated DI water bubbler system. The piping after the bubbler system is heated and kept at a slightly higher temperature than the bubbler itself to avoid condensation within the steel piping. Before the gas stream reaches the measurement chamber with the CNFET sensors, it passes through a high power heating tube, which can be optionally used to heat the gas stream. The aluminum gas measurement chamber, where the CNFET sensor chips are placed, is situated on a hotplate and can be additionally heated. Immediately in front of the measurement chamber a humidity and temperature sensor are installed, also within and after the measurement chamber the temperature of the gas stream can be monitored. After passing the measurement chamber, the NO$_2$ content of the gas stream is analyzed in a chemiluminescent NO$_x$ analyzer (API Model 200A) before it is fed into the exhaust system of the building. The total flow of the gas mixing system is set to 1 - 1.5 l/min. The entire gas mixing setup is controlled via a custom made software, which allows long and sophisticated gas profiles. Depending on the concentration level of the NO$_2$ source cylinder, a wide range of concentration levels starting from about 50 ppb up to several hundred ppm of NO$_2$ can be added to the carrier gas. If the target concentration level is set below 50 ppb of NO$_2$, the NO$_x$ analyzer reveals a

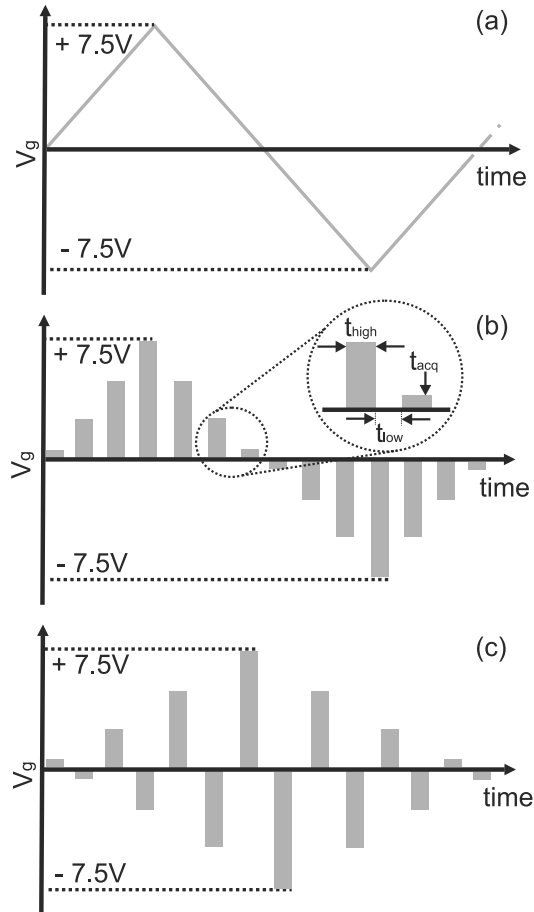**Figure 3.11:** With the measurement setup the gate voltage (V_g) can be applied in three different modes to the gate electrode: (a) continuous V_g; (b) pulsed V_g (p++) with voltage pulses of the same polarity being part of the same half of the V_g waveform period and (c) pulsed V_g (p+-) with voltage pulses of alternating polarity. Adapted from [67]. Copyright Institute of Physics and IOP Publishing 2010.
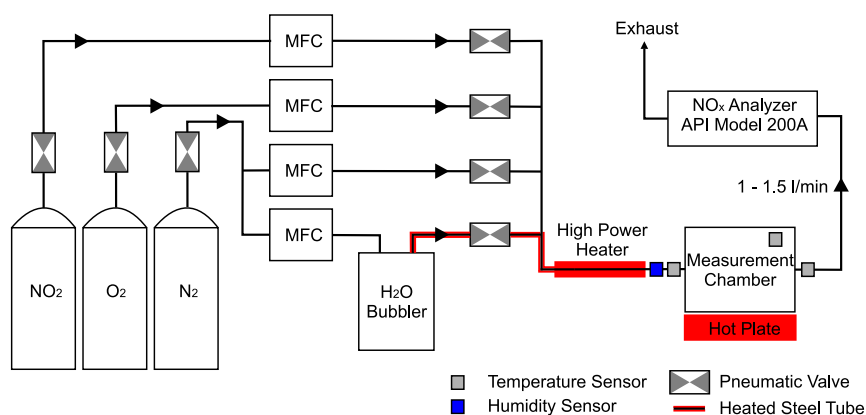
Figure 3.12: Schematic of the gas mixing setup at Siemens AG in Munich. Down to 50 ppb of NO_2 are mixed to the synthetic dry air (80 % N_2 and 20 % O_2) by means of mass flow controllers (MFCs). If desired humiditiy can be added to the gas stream. The temperature of the gas stream is measured in front of, within and after the measurement chamber. The relative humidity is monitored immediately in front of the measurement chamber. Before the gas stream is fed to the exhaust system, its NO_2 content is analyzed.

very unstable NO_2 content in the gas stream. In this low concentration region the MFC of the NO_2 line is at its lower specified flow limit. In addition its control loop is too slow, which causes large spikes in the concentration profile when switching from one concentration level to the next. Beside the three gas lines for O_2, N_2 and NO_2 the gas mixing setup at Siemens features many more lines for various other gases. Before a new measurement session was started the entire mixing unit was flushed at high flow rate with N_2 for at least two hours to clean the mixing unit. During the NO_2 measurements all additional gas lines were closed.

3.3.2 Gas measurement chamber

During experiments with NO_2, the CNFET chips are placed in an airtight home-built aluminum chamber. As shown in Fig. 3.13a, it consists of a bottom part, a middle part and a lid. The bottom part hosts the chip socket, the electrical feed-throughs to connect the CNFETs to the electrical measurement setup and a temperature sensor to record the temperature during experiments, as seen in Fig. 3.13b. The middle part of the chamber features two diagonally arranged gas connections while the lid also holds a gas connection. The chamber has a volume of about 30 ml. Considering the used flow rates of 1 to 1.5 l/min, the entire volume of the measurement chamber is theoretically exchanged within about 1 to 2 s. Such a fast gas exchange rate is necessary to ensure that during NO_2 experiments the pure gas
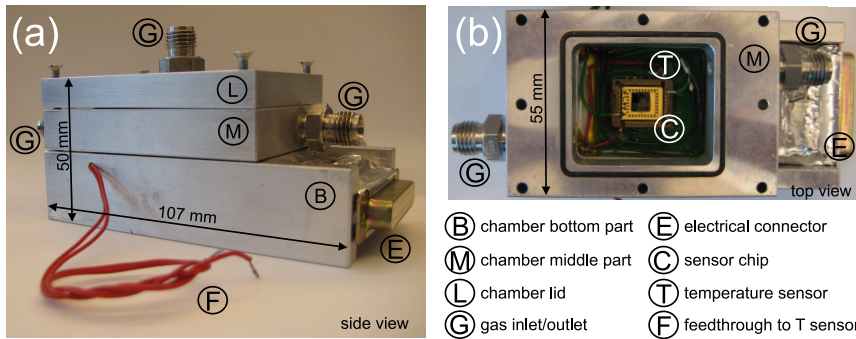
Figure 3.13: Photography of the gas measurement chamber. Side view (a) of the socket and middle part and the lid. Top view (b) of the socket and middle part (without lid).

sensing performance of the CNFET sensors can be observed without corruption originating from the gas measurement setup. During the project, two different gas inlet and outlet configurations at the measurement chamber are applied. Configuration 1: The gas inlet and outlet are both on the middle part of the measurement chamber. As a result, the gas stream flows diagonally across the chamber and parallel to the surface of the CNFET sensor chip. Configuration 2: The gas inlet is located at the chamber lid and the gas stream flows perpendicularly onto the CNFET sensor chip. The two gas connections at the middle part of the gas chamber are then used as gas outlets. Regardless of which configuration is applied, the gas sensing performance of the CNFET remains unchanged.

3.3.3 NO$_2$ concentration calibration

At the beginning of every measurement session at Siemens AG for the characterization of the CNFET sensors in NO$_2$, the gas mixing setup is calibrated for synthetic air as carrier gas and NO$_2$ as target analyte. Considering the concentration level of the NO$_2$ source bottle the theoretical NO$_2$ concentration level can be calculated for different MFC settings. For calibration, a NO$_2$ concentration step profile is executed and the gas stream is analyzed with a chemiluminescent NO$_x$ analyzer (API Model 200A). The measured and the calculated values are then compared and the settings for the MFC of NO$_2$ line are adjusted as necessary (typically up to about 20 %, especially close to the specified minimum flow rates of the MFCs) to reach the desired target NO$_2$ concentration. Once calibrated at the beginning of each measurement session and given that the NO$_2$ source bottle is not changed, the MFC settings stay valid for days until the end of the measurement session.

3.4 Measurement data analysis

The recorded measurement data is read from the stored text files, further analyzed and plotted by using several modular MATLAB scripts.

- Data filtering
  The recorded $I_d V_g$ characteristics are smoothed using a Savitzky-Golay filter of polynomial order 2 and varying frame size depending on the number of recorded samples and noise level. In order to avoid filtering artifacts at the beginning and the end of a $I_d V_g$ characteristic, the data set of length k is tripled to obtain a new data set of length 3k. The newly created data set is then filtered and its middle part (k:2k-1) is extracted as the smoothed $I_d V_g$ characteristic. To demonstrate the impact of the applied filtering strategy, a typical example of a raw and filtered $I_d V_g$ characteristic is shown in Fig. 3.14.

- V_{th} extraction
  V_{th} values are extracted from the $I_d V_g$ characteristics as described in [63]. The current I_d is linearly interpolated at the maximum transconductance (dI_d/dV_g) of the forward (-$V_{g,max}$ to +$V_{g,max}$) and backward branch (+$V_{g,max}$ to -$V_{g,max}$) to determine $V_{th,forward}$ and $V_{th,backward}$ on the V_g axis.

- Gate hysteresis width
  The gate hysteresis width is calculated as the difference between $V_{th,backward}$ and $V_{th,forward}$.
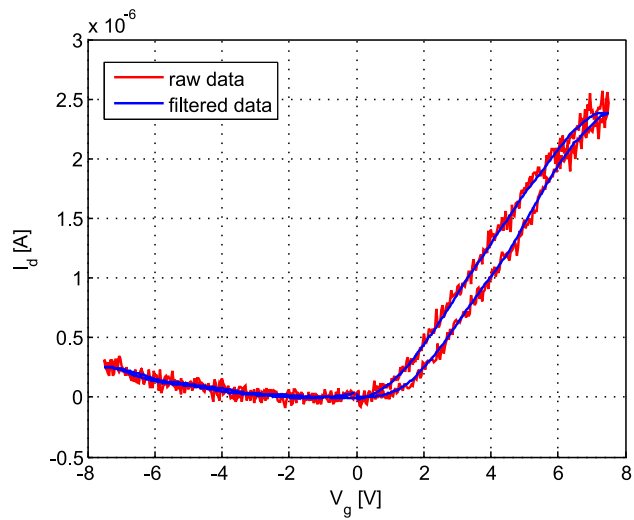
Figure 3.14: Representative example of an $I_d V_g$ characteristic plotted from raw and filtered data (frame size = 10% of the total number of data points, filter order = 2. V_{sd} = 300 mV.

4 CNFET NO$_2$ sensor with passivated metal contacts

In this chapter a new CNFET NO$_2$ sensor structure is proposed and tested, which features ALD Al$_2$O$_3$ passivated metal contacts and pristine SWNT channels, exposed to the ambient via well-defined windows in the Al$_2$O$_3$ passivation layer. The motivation to introduce and characterize an enhanced CNFET sensor structure are two major issues associated with as-prepared CNFET NO$_2$ sensors. Namely, CNFET on-current degradation over time and the presence of SB modulation as NO$_2$ gas sensing mechanism, which was found by others [95] to be not as reproducible as sensing mechanisms dedicated to the SWNT bulk. These two issues are explained in the first part of the chapter. In the following the proposed CNFET sensor structure is subject to several tests to systematically validate that it fulfills basic sensor requirements. As such, the sealing properties of the ALD Al$_2$O$_3$ in high concentration of NO$_2$ are tested, a NO$_2$ sensitivity test and a sensor recovery check are performed, followed by the confirmation of improved long-term stability compared to as-prepared CNFET devices. All I$_d$V$_g$ characteristics shown in this chapter are recorded with continuous V_g sweeps.

Parts of this chapter were published in [129].

Content

4.1 Introduction

In the past, the majority of experiments in CNFET studies in microelectronics and sensors were conducted in laboratory conditions (controlled atmosphere and temperature) and presented data was often acquired in a rather short period of time, when long-term device stability does not appear to be an issue. However, when envisioning CNFETs as building-blocks for any kind of real-life applications, operation over a long period of time in uncontrolled ambient conditions and therewith device long-term stability may become a very important aspect.

4.1.1 CNFET on-state degradation

Helbling *et al.* [63] presented a study in which they investigated the long-term

Metal Contact Degradation

stability of non-passivated, as-prepared CNFET devices. After storing the devices for a few days in ambient conditions, they observed a substantial decrease of the p-type on-state current over time (Fig. 4.1), which finally resulted in inoperative devices. In the study they discuss two different origins for the on-conductance degradation: first, metal contact degradation, leading to contact barrier increase between the SWNT channel and the metal leads. Second, defects generated in the SWNT channel, causing additional electron scattering centers. By analyzing $I_d V_g$ characteristics measured on different days after device fabrication they found that over time the overall CNFET conductance decreased, independent of V_g. This can be understood as the signature of an additional series resistance at the metal leads, which might be caused by increased injection barriers for carriers due to continuous oxidation of the metal contacts. Defects in the SWNT channel on the other hand, would affect the density of states non-uniformly, resulting in device conductance changes dependent on V_g. This was not observed in the measurement data. They finally proposed that oxidation of the metal leads is the major degradation mechanism of non-passivated CNFETs.

4.1.2 ALD Al$_2$O$_3$ passivation layer

Criteria   Considering the findings of Helbling *et al.*, one possible solution to achieve long-term device stability in ambient conditions is based on blocking corrosive species from reaching the CNT-metal leads interface. A suitable passivation layer for CNFETs has to fulfill several criteria. First, the passivation layer has to be a pinhole-free, conformal and efficient diffusion barrier for corrosive species, such as O$_2$ and H$_2$O, to block their access to the delicate CNT-metal leads interface. Second, the passivation material has to be non-conductive, in order to prevent shorting the source and drain metal leads. Third, the layer deposition method has to be plasma-free in order to prevent damage to the SWNT channel and should be a low temperature process in order not to harm the metal leads. Finally, the deposition process should allow a good controllability of the deposition thickness.

ALD Al$_2$O$_3$ A promising deposition technique for CNFET passivation layers, fulfilling all the above listed requirements, is atomic layer deposition (ALD) of oxides [130, 131]. Helbling *et al.* have studied long-term stability of ALD Al$_2$O$_3$ passivated CNFETs and found that CNFETs encapsulated by 100 nm of ALD Al$_2$O$_3$ show stable CNFET metrics, such as on-state conductance, gate hysteresis width and the location of the gate hysteresis, over a measured period of 260 days. This observation can be explained by the fact that the ALD deposition process takes place in a reactor chamber at 150°C, at low pressure (11 Pa) and in a flow of N$_2$ as carrier gas. Under these conditions most H$_2$O and O$_2$ molecules are removed from the CNFET
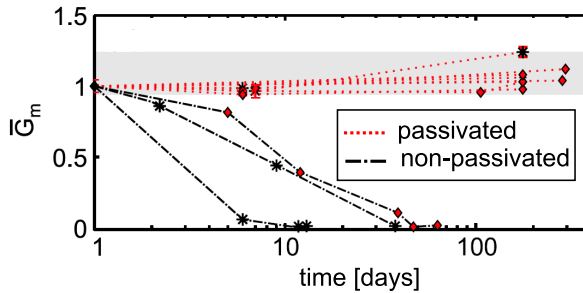
Figure 4.1: Normalized on-state conductivity versus time of non-passivated and fully passivated CNFETs with 100 nm ALD Al_2O_3. Adapted from [63]. Copyright Institute of Physics and IOP Publishing 2009.

surface. The resulting Al_2O_3 layer is conformal and pinhole-free and acts as a diffusion barrier for O_2 and H_2O and therefore can efficiently protect CNFETs from environmental influences, especially the delicate interfaces at the CNT channel and metal leads.

4.1.3 Proposed sensor structure

In the past, thin layers of several different materials, such as polymethyl methacrylate (PMMA)[60, 93], nitrides [106] and oxides [103], have been used to fully or also partially encapsulate CNFET devices. The focus of these studies was often not on achieving device long-term stability but on elucidating sensing mechanisms in CNFET chemical sensors by partial encapsulation of distinct sensor regions. As mentioned already in section 2.3.2 the results from these investigations are not conclusive so far. Heller *et al.* [95] performed a study on identifying the mechanism of biosensing with CNFETs partially passivated with PMMA. They found most of their experiments to be explainable by effects dedicated to both the interface between the SWNT channel and the metal leads, as well as to the SWNT channel. In addition, they found that SB modulation, happening at the interface between the SWNT channel and the metal leads, appeared less consistent and reproducible than the doping effect occurring at the SWNT channel.

Reliable Sensing Mechanism

The results from Helbling *et al.* about device long-term stability and from Heller *et al.* about sensing mechanisms suggest that a CNFET NO_2 sensor device with impermeably passivated metal contact areas could be the most suitable design choice. First, this device architecture can be expected to have improved long-term stability compared to unpassivated devices since the degradation prone contact regions of the CNFET are protected from the ambient. Second, a device with pas-

Proposed Sensor Structure

sivated contact regions employs only the SWNT channel as gas sensitive part and the less reproducible sensing mechanism of direct SB modulation is inhibited. The fabrication process for the proposed CNFET NO$_2$ sensors is detailed in section 3.1. Fig 4.3(a) and (b) show a schematic and an illustration based on atomic force microscopy (AFM) data of the enhanced CNFET NO$_2$ sensor, respectively. The SWNT channel is exposed to the ambient and is employed for NO$_2$ sensing.

4.2 Validation of the proposed sensor structure

4.2.1 Al$_2$O$_3$ sealing test in NO$_2$

Motivation

Helbling *et al.* showed that a thin layer of ALD Al$_2$O$_3$ efficiently seals CNFETs from ambient air and renders them long-term stable for at least hundreds of days. However, this solution to seal a CNFET and protect it from its ambient is not necessarily compatible with every CNFET application. This applies especially for CNFETs operated as chemical sensors, which are exposed to other and/or higher concentrated chemical species than normally present in ambient air. In the proposed CNFET sensor structure, ALD Al$_2$O$_3$ has to protect the passivated metal SWNT interfaces from NO$_2$.

Results

For the purpose of the passivation layer in the CNFET NO$_2$ sensors a Al$_2$O$_3$ thickness of about 40 nm is chosen. A layer of this thickness should be already pinhole free and can be more easily etched during the window opening process than a layer of 100 nm thickness as it was used by Helbling *et al.* In order to test whether 40 nm of ALD Al$_2$O$_3$ is an efficient barrier to block NO$_2$ molecules from a CNFET, a sealing test of the passivation layer in NO$_2$ is performed. For this experiment fully passivated CNFETs with 40 nm of ALD Al$_2$O$_3$ are exposed to 80 ppm of NO$_2$ in synthetic dry air as carrier gas for 90 minutes. 80 ppm of NO$_2$ is considered being a high concentration since it exceeds many times the maximum NO$_2$ concentrations to which the CNFET sensors are exposed in the following detection experiments. Fig. 4.2 shows the I$_d$V$_g$ characteristics of the same device in synthetic dry air before and after NO$_2$ exposure (black squares and red circles). Even after NO$_2$ exposure, the two characteristics are essentially identical.

Discussion

No Shift of I$_d$V$_g$ Characteristics

Had NO$_2$ molecules reached the CNFET surface despite the ALD Al$_2$O$_3$ passivation layer we would have expected a rigid shift of the I$_d$V$_g$ characteristic, a
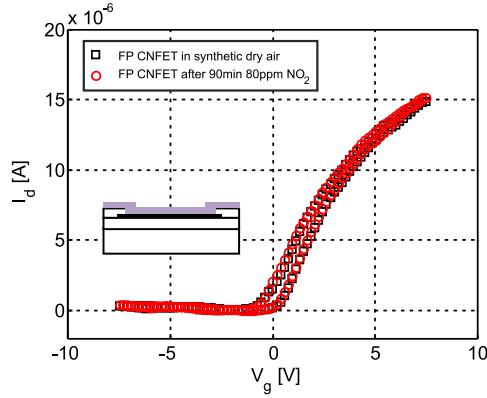
Figure 4.2: Gate characteristics of a fully ALD Al_2O_3 passivated CNFET in synthetic dry air (black squares), after 90 min exposure to 80 ppm of NO_2 (red circles). V_{sd} = 300 mV. Adapted from [129]. Copyright American Institute of Physics 2009.

change of the on-state currents or a combination of the two effects, as explained in section 2.3.2. Since this was not observed it can be concluded that the 40 nm ALD Al_2O_3 passivation layer is capable of efficiently blocking NO_2 in concentrations up to 80 ppm from reaching the CNFET. This opens the possibility to create partially passivated devices with 40 nm ALD Al_2O_3 to expose only selected areas of a CNFET to NO_2.

Besides the main results we observe that upon passivation of CNFETs with ALD Al_2O_3 they typically change from polar p-type to polar n-type [63]. As shown by Heinze *et al.* [132] the continuous desorption of oxygen by placing unpassivated CNFETs in a vacuum chamber turns polar p-type CNFETs gradually into polar n-type devices and again back to polar p-type as the devices are again exposed to ambient. This phenomenon is attributed to a change in the energy band alignment at the interface between the metal contact and the SWNT channel upon adsorption of NO_2 (Fig. 2.5) [133–135]. The adsorption of oxygen on the metal-SWNT interface can be understood to cause a decrease of the metal workfunction ϕ_s and/or increase of the SWNT electron affinity χ_s. The $I_d V_g$ characteristics in Fig. 4.2 represents a typical n-type $I_d V_g$ characteristic of a fully passivated CNFET. It features almost no hole conductivity, which is the signature of a semiconducting SWNT with large SBs for holes. The minimum resistance (V_g = 7.5 V) is around 20 kΩ, revealing the high quality electrical contacts of our CNFETs. The CNFET on-state is not reached within the given gate voltage range mainly due to the thick gate oxide.

Device Type
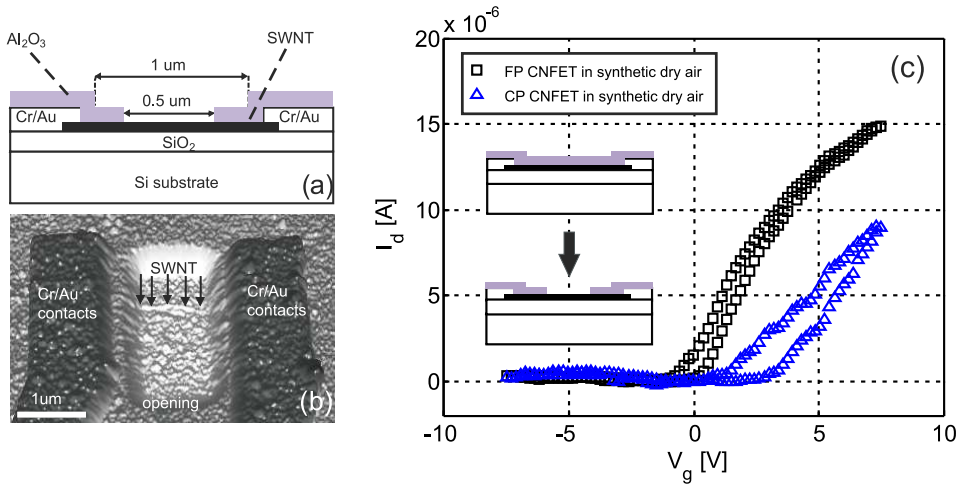
Figure 4.3: Schematic view (a) and 3D AFM data (b) of a CNFET with open SWNT channel and ALD Al_2O_3 passivated metal contacts. (c) CNFET device before (black squares) and after (blue triangles) etching a window at the CNT channel into the ALD Al_2O_3 passivation layer. Adapted from [129]. Copyright American Institute of Physics 2009.

4.2.2 Window opening above the SWNT channel

Motivation

In order to turn a fully passivated CNFET into a CNFET chemical sensor, the passivation layer has to be selectively removed at the middle section of the SWNT channel. The removal is done in a wet etching step with hydrofluoric acid (HF), as described in detail in section 3.1.8. As HF etches both SiO_2 and ALD Al_2O_3 isotropically and with very poor selectivity , the etching step is a timed process step. Changes in the I_dV_g characteristics upon opening the window above the SWNT channel can be used as indicators as to whether the etching step was successful or not.

Results

Impacts of Window Opening

After successfully etching a 0.5 μm wide and 40 nm deep opening (Fig. 4.3(a) and (b)) into the passivation layer, the same CNFET with contacts still passivated, continues to feature distinct n-type behavior without p-type conduction, as seen in Fig. 4.3(c). The I_dV_g characteristic suffers though a few changes: the gate threshold voltage (V_{th}) is positively shifted, the subthreshold swing is decreased and the gate hysteresis is broadened (Fig. 4.3(c)).

Discussion

Conservation of the n-type behavior upon removing the Al_2O_3 layer above the SWNT channel is a very strong indication for the proper sealing of the metal contacts from the environment, especially from oxygen molecules by the applied Al_2O_3 passivation layer [107]. If the etching time is too long or the etching mask is badly aligned with respect to the source and drain metal contacts, the Al_2O_3 passivation layer at the SWNT-metal interface can be partially removed (results not shown). As a result, I_dV_g characteristics turn into polar p-type after the etching step, which indicates that at least parts of the SWNT-metal interface are exposed to ambient air and the device can not be used as CNFET NO_2 sensor.

Proper Sealing

The positive shift in the gate threshold and decrease in the subthreshold swing might be explained by the change in the dielectric interface at the SWNT after the removal of the Al_2O_3. By means of a two-dimensional finite element method analysis, the change in the gate capacitance (wire above conductive plate) prior and after removal of the Al_2O_3 passivation layer at the CNT can be estimated. The analysis reveals a substantial decrease in the gate capacitance after removal of the Al_2O_3 by a factor of about two, which may explain the decreased subthreshold swing and the shift of V_{th}. The positive shift of V_{th} can also be attributed to oxygen doping of the exposed SNWT channel, as shown by Donghun *et al.* [136]. The broadening of the gate hysteresis can be attributed to an increased density of charge traps due to H_2O molecules, which can now adsorb on the exposed CNFET channel [60]. If these changes in the I_dV_g characteristic are not observable after the window opening step, it is very probable that the SWNT channel is still covered with ALD Al_2O_3. This might be due to a too short etching time or surface wetting issues, which hinder the HF from reaching the ALD Al_2O_3 surface.

Decreased Gate Capacitance

Oxygen Doping

Charge Traps

4.2.3 NO_2 sensitivity test

The next step is to test whether CNFETs with exposed SWNT channels and ALD Al_2O_3 passivated metal contacts are still sensitive to NO_2. This is necessary since so far CNFETs employed as NO_2 gas sensors have been mostly unpassivated in which both proposed NO_2 sensing mechanisms due to the metal-SWNT interface and the SWNT body are present. Moreover, there exists a study by Zhang *et al.* [93], in which partially passivated CNFETs are employed for NO_2 detection. They find chemical modifications at the interface between the CNT channel and the metal leads to be responsible for NO_2 sensing. From a fabrication point of view it also needs to be clarified whether the deposition of ALD Al_2O_3 layer and the following partial removal in the window etching process (see section 3.1.8) do not chemically modify the SWNT channel [137, 138], which could render it

Motivation
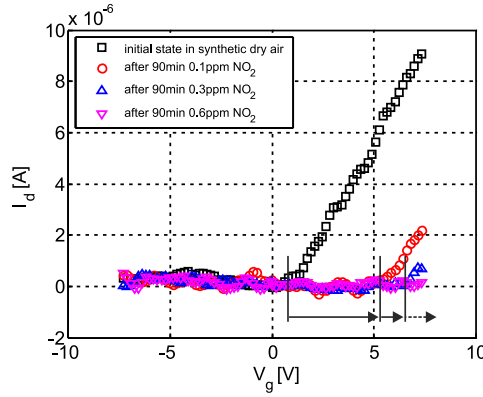
Figure 4.4: $I_d V_g$ characteristics (one current branch only) of a CNFET with exposed CNT channel and ALD Al$_2$O$_3$ passivated metal contacts in synthetic dry air and upon exposure to 0.1, 0.3 and 0.6 ppm of NO$_2$. V_{sd} = 300 mV. Adapted from [129]. Copyright American Institute of Physics 2009.

insensitive to NO$_2$.

Results

The NO$_2$ sensitivity test consists of a NO$_2$ concentration profile with steps of 0.1, 0.3, and 0.6 ppm and 90 min duration in synthetic dry air (80% N$_2$ and 20% O$_2$) as carrier gas. Before the first, after the last and between all NO$_2$ concentration levels flushing periods with synthetic dry air, also of 90 min duration are applied. Fig. 4.4 shows CNFET $I_d V_g$ characteristics in synthetic dry air and upon exposure to the NO$_2$ concentration profile. The CNFET $I_d V_g$ charcteristics are recorded at the very end of every concentration level. This ensures that the NO$_2$ adsorption process at the SWNT channel has reached steady state, which seems reasonable since 90 min is several fold above reported response times in CNFET based NO$_2$ sensors [15, 139]. Note that the shown $I_d V_g$ characteristics are recorded with continuous V_g and show a substantial gate hysteresis. To make the shifts of V_{th} better visible only the forward sweep from V_g = -7.5 V to V_g = + 7.5 V of the $I_d V_g$ charaterisitcs is shown. Upon NO$_2$ exposure two main observations can be made from the $I_d V_g$ characteristics: first, concentration-dependent positive shifts of V_{th} (ΔV_{th}(0.1 ppm) $\approx$ +4.5 V and ΔV_{th}(0.3 ppm) $\approx$ +1.5 V). For a concentration of 0.6 ppm NO$_2$ V_{th} is shifted outside the range of the applied V_g[-7.5, +7.5] V. Second, the current I_d for negative V_g remains unchanged upon NO$_2$ exposure (no hole conduction onset).

Positively Shifted V_{th}

54

Discussion

The shifts of the gate characteristics can be explained by an effect taking place at the CNFET channel. In a theoretical study, electron charge transfer from the SWNT to the adsorbed NO_2 molecules was suggested to cause hole doping, which can result in the observed positive V_{th} shift. In unpassivated CNFETs, NO_2 molecules can also adsorb on the source and drain metal contacts, which can cause a modification of the metal/SWNT energy band alignment and thereby make the SBs more transparent for holes. However, for our CNFETs with passivated contacts, hole conduction ($V_g < 0$ V) remains unchanged. It seems that for our CN-FETs with passivated metal contacts, effects on the exposed CNFET channel, such as hole doping due to adsorbed NO_2 gas molecules, are the dominant NO_2 sensing mechanisms. The etching step to open the window into the passivation layer is capable of removing the ALD Al_2O_3 around the SWNT channel to provide access to the NO_2 molecules. The CNFET sensor structure with exposed SWNT channel and protected metal contacts is still sensitive to NO_2 with observed LOD (0.1 ppm NO_2) very well comparable or even lower than minimum concentration levels measured in (unpassivated) CNFET NO_2 sensors with pristine SWNT channels (2 ppm NO_2 [15], 6 ppm NO_2 [96], 0.5 ppm NO_2 [105]).

Charge Transfer

LOD

4.2.4 CNFET sensor recovery from NO_2 exposure

Due to the naturally perfect lattice structure of a SWNT side wall, NO_2 molecules are expected and confirmed by ab-initio calculations to physisorb rather than chemisorb onto a semiconducting (10,0) SWNT [84–86]. On the other hand, if the SWNT has vacancy defect sites, strong chemisorption type interactions between NO_2 and the SWNT are possible [90, 91], which may render NO_2 adsorption onto the SWNT hardly reversible. We therefore have to check by a NO_2 desorption experiment whether the $I_d V_g$ characteristics of our CNFET sensors can be recovered from NO_2 exposure.

Motivation

Results

NO_2 detection and the recovery behavior of a CNFET sensor with passivated metal contacts is shown in Fig. 4.5. Upon exposure to 0.3 ppm of NO_2, the gate characteristic is positively shifted. After flushing the measurement chamber for 90 min with synthetic dry air, the gate characteristic is negatively shifted but the initial state is not completely recovered. However, after heating the sample on a hotplate to 110 °C for 30 min and storing the device for 24 h in ambient air, the $I_d V_g$ characteristic shows almost complete recovery.

Heat Treatment
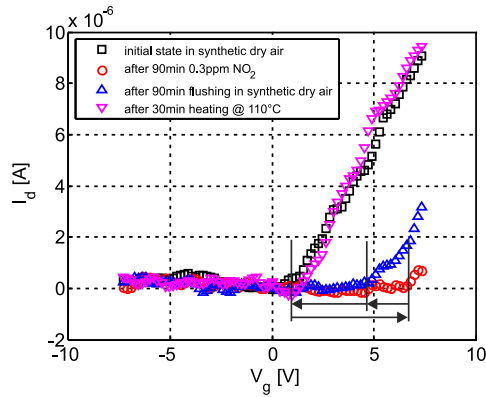
Figure 4.5: CNFET sensor gate characteristic in synthetic dry air, upon exposure to 0.3 ppm of NO$_2$, after partial recovery by flushing for the 90 min with synthetic dry air and after heat treatment at 110 °C for 30 min and device storage in ambient conditions for 24 h. V_{sd} = 300 mV. Adapted from [129]. Copyright American Institute of Physics 2009.

Discussion

Thermally Activated Process

Slow molecular desorption of NO$_2$ gas seems to be the origin of the observed negative shift, which results in partial recovery of the $I_d V_g$ characteristic at room temperature. Since adsorption and desorption of gas molecules are usually thermally activated processes, the molecular desorption rate can be increased by heating the CNFET sensors and complete sensor recovery can be achieved in a shorter time. Another method to increase the NO$_2$ desorption rate is the exposure of the sensor to ultra violet (UV) light. The desorption experiment shows that CNFET sensors with passivated contacts are resettable and can be reused for NO$_2$ detection. Accelerated chemical sensor recovery is achieved upon heat treatment (tested 1h at 110 °C versus 24h at room temperature). These findings are in good agreement with the result of the very first study on CNFETs for NO$_2$ sensing by Kong *et al.* [15], which reports sensor recovery within 1h by heat treatment at 200 °C and several hours at RT.

4.2.5 Improved long-term stability

Stability Metrics

Compared to the thorough long-term stability study performed by Helbling *et al.* of fully passivated CNFETs with well-defined performance metrics, no such detailed investigation with a large number of devices was performed for the CNFETs with passivated contact regions. First, for CNFETs with SWNT channels exposed to the ambient it is more difficult to define performance metrics, which
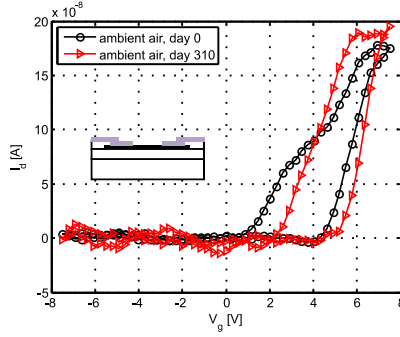
Figure 4.6: $I_d V_g$ characteristics of a CNFET sensor with exposed SWNT channel and passivated metal contacts in ambient air recorded at day 0 and 310. $V_{sd} = 30$ mV.

reliably reflect the long term stability of the devices. The gate hysteresis width, the threshold voltage and also the maximum on-state current are naturally subject to fluctuations if the device is not stored in perfectly controlled environment (composition of the gaseous atmosphere, humidity level and temperature). Second, only a few devices were available to study the long-term stability since many devices did not reach their full living expectation. Some of them were either damaged during transportation between Zurich and Munich, presumably due to electrostatic discharge during handling or due to extensive heat treatment during recovery cycles.

Results

In Fig. 4.6 $I_d V_g$ characteristics of a CNFET sensor with exposed CNFET channel and passivated contacts are shown, recorded at day 0 and day 310 after fabrication (maximum time measured) in ambient air. It can be seen that the characteristic recorded at day 310 shows positively shifted V_{th} values ($\Delta V_{th} \approx +1$ V) in the forward and backward sweep compared to the characteristic measured at day 0. Nevertheless, ignoring the small V_{th} shift, I_d current levels of both $I_d V_g$ characteristics are comparable. The on-state current ($I_d(V_g = 7.5$ V)) of the $I_d V_g$ characteristic recorded at day 310 has not dropped compared to the $I_d V_g$ characteristic at day 0.

Constant I_d Level

Discussion

The small shift of V_{th} might explained by the adsorption of any gaseous species (e.g. change of the ambient humidity level) on to the exposed SWNT channel

Unchanged Injection Barriers

during the long storage in ambient air between the measurements or by natural V_{th} fluctuations. The almost constant on-state current of the two $I_d V_g$ characteristics indicates that the injection barriers for electrons at the interface between the SWNT and the metal contacts have not increased after 310 days. This is in strong contrast to the observations made by Helbling *et al.* with non-passivated CNFETs, which showed significant drop of the on-state conductance within days to weeks. Since this very CNFET was successfully used for NO$_2$ sensing and its $I_d V_g$ characteristic shows a clearly positive V_{th} and substantial gate hysteresis, we can be relatively sure that its SWNT channel is exposed to ambient air. No thorough long-term stability study with a large number of devices was performed for CN-FETs with passivated contacts. However, the few devices, which were available to study the long-term behavior, show significantly improved long-term stability in terms of their on-state current compared to non-passivated devices.

4.3 Summary and conclusion

Device Stability

In this chapter we have first looked at the issue of long-term stability of as-prepared CNFET devices. While the on-state conductance in unpassivated CNFETs degrades within days and weeks, CNFETs fully passivated with 100 nm ALD Al$_2$O$_3$ were found by Helbing *et al.* to be stable in ambient conditions over more than 260 days. Analyzing the $I_d V_g$ characteristics of unpassivated CNFETs, an increase of the injection barriers over time at the metal-SWNT interface seems to be the most probable degradation mechanism, presumably due to continuous metal oxidation.

ALD Al$_2$O$_3$

Atomic layer deposition (ALD) of oxides was shown to be a very suitable method to form passivation layers of CNFETs. The deposition of ALD Al$_2$O$_3$ results in pinhole-free, conformal and non-conductive layers of well controllable thickness. Moreover, ALD can be performed without plasma and high process temperatures which could harm the CNFET devices. In contrast to other passivation methods, such as spin coating of polymer layers (PMMA, SU8), ALD Al$_2$O$_3$ can achieve airtight passivation layers.

Sensing Mechanisms

As the dominant sensing mechanism of NO$_2$ and other chemicals is still under debate, Heller *et al.* [95] found the sensing mechanism associated with the SWNT bulk in CNFETs operated as biosensors to be more reproducible then the sensing mechanism at the metal contacts.

Based on the findings about CNFET long-term stability and the results about the reproducibility of sensing mechanisms in CNFETs, an enhanced CNFET structure for NO$_2$ sensing was proposed: a CNFET with ALD Al$_2$O$_3$ passivated metal contacts and exposed SWNT channel.

Subsequently, the proposed CNFET sensor structure and was subject to several tests. 40 nm of ALD Al_2O_3 was found to properly block NO_2 molecules from reaching buried CNFET devices. Even after 90 min exposure of 80 ppm NO_2 the I_dV_g characteristic remained unchanged. Further, the window etching into the passivation layer at the SWNT channel was investigated. The devices continue to feature polar n-type I_dV_g characteristic, which is a strong indication that the metal contacts are still properly sealed from oxygen even after exposing the SWNT channel to ambient. In the NO_2 sensitivity test, the CNFET sensor was exposed to a step profile of NO_2, namely 0.1, 0.3 and 0.6 ppm of NO_2 for 90 min each, interrupted by flushing intervals with synthetic dry air of also 90 min duration each. The I_dV_g characteristics were subject to concentration dependent positive shifts of V_{th} upon NO_2 exposure, which is in agreement with proposed sensing mechanisms at the SWNT channel. No p-type current onset was observed upon NO_2 exposure, which suggests that direct SB modulation is inhibited as sensing mechanism in the proposed CNFET sensor structure. The measured LOD of 0.1 ppm of NO_2 can compete with state-of-the-art CNFET sensors with pristine SWNT channels. In a NO_2 desorption experiment it was shown that the proposed CNFET sensor structure can be refreshed. The sensors can be reset in ambient air within about 24 hours or sensor recovery can be accelerated by heat treatment. Finally, it was reported that the CNFET sensors with passivated metal contacts show superior long-term stability compared to unpassivated CNFETs. As the I_dV_g characteristics of a CNFET NO_2 sensor at day 0 and 310 reveals, even after months, the on-state current levels remain mostly unchanged.

Sensor Testing

5 Hysteretic effects in CNFET NO$_2$ sensors

The I_dV_g characteristics shown in chapter 4 are all recorded with continuously swept V_g and show considerable gate hysteresis between the forward and backward V_g sweeps (see e.g. Fig. 4.6). The gate hysteresis is believed to be caused by charge injection from the SWNT channel into charge traps near the SWNT channel at high V_g, as introduced in section 2.2.3. When extracting V_{th} as the sensor output signal at different gas concentrations in the presence of hysteresis, common practice [15, 74] has been to use V_{th} of one branch only, as it is also done in chapter 4, or the mean value of the two branches. However, only a measure not corrupted by hysteresis can properly reflect the gas-sensing mechanism and one such measure is the intrinsic V_{th}.

Charge Traps

V_{th} Sensor Signal

Solutions to reduce the gate hysteresis in CNFETs have already been considered, such as complete encapsulation of CNFETs, typically with thin layers of oxide [63] or polymers [60], or the deposition of selfassembled monolayers (SAMs) [140], which render the device surface hydrophobic. The encapsulation of CNFET devices is aimed at keeping the CNFET surface clean from adsorbates, which potentially act as charge traps and can cause increased gate hysteresis. Nevertheless, in particular for CNFETs operated as chemical sensors, these measures either completely block access of the analytes to the sensitive SWNT channel or at least are very likely to change the adsorption and desorption properties of the analytes due to modification of the sensor surface chemistry. Instead, a method for hysteresis reduction, which comes along without structural or chemical modifications of the CNFET NO$_2$ sensor, would be desirable. Lin *et al.* [59] have demonstrated a method to reduce gate hysteresis in CNFETs in ambient air, which is purely based on the electrical measurement method to record I_dV_g characteristics. In brief, the proposed method is based on pulsed V_g sweeps instead of continuous V_g sweeps. If the V_g pulses are short enough (in the range of 1 ms duration), the time for the charge traps near the SWNT to be filled is reduced and thereby the I_dV_g characteristics can become essentially hysteresis-free.

Hysteresis Reduction

In this chapter we first test the pulsed V_g measurement mode for hysteresis reduction in our CNFET NO$_2$ sensors in synthetic dry air. In addition, another pulsed mode, based on pulses of alternating polarity, is proposed and also tested in syn-

Content

thetic dry air. The measurement results are also compared to data obtained from the hysteresis model introduced in section 2.2.3. In the second part of this chapter the pulsed V_g methods are tested for NO$_2$ sensing to verify that the V_g pulses do not interfere with the NO$_2$ adsorption and desorption process. Finally, pulsed V_g waveforms are demonstrated to erase electrical history in CNFET devices, which can be used to initialize a CNFET sensor before every measurement of the I$_d$V$_g$ characteristics.

Parts of this chapter were published in [67, 141, 142].

5.1 Pulsed V_g sweeps for hysteresis reduction in dry air

Motivation

Intrinsic V_{th} Reducing gate hysteresis and hence obtaining a better estimate for the intrinsic V_{th} has been shown by Lin *et al.* [59] by using pulsed instead of continuously swept V_g. A good estimate for the intrinsic V_{th} is very important since the CNFET gas sensors rely on V_{th} as their sensor output signal. The CNFET devices employed by Lin *et al.* were non-encapsulated, as opposed to our CNFET NO$_2$ gas sensors, which have passivated metal contacts and an exposed midsection of the CNFET channels.

In this section we investigate whether pulsed V_g sweeps can be used to reduce gate hysteresis in CNFET sensors with open SWNT channels and ALD Al$_2$O$_3$ passivated metal contacts in dry air conditions.

Results

Pulse Time t_{high} The CNFET I$_d$V$_g$ characteristics shown in Fig. 5.1(a) are recorded for voltage pulses with t_{high} = 50, 10 and 0.5 ms for the p++ pulse mode. The different pulse modes are introduced in the methodology section 3.2.2. The extracted mean hysteresis width for the pulse time t_{high} = 50 ms is about 1.15 V (100 %), which is reduced for shorter pulse times to 0.55 V (48 %) for t_{high} = 10 ms and to about 0.15 V (13 %) for t_{high} = 0.5 ms. Indeed, this confirms the observation of Lin *et al.* that reducing the V_g pulse duration reduces gate hysteresis width H in the I$_d$V$_g$ characteristics.

Trap states in the dielectric and/or adsorbates close to the SWNT channel have been proposed to be the main reason for gate hysteresis observed in CNFET characteristics. With this picture in mind, shorter V_g pulses leave less time for the traps to be filled and thus lead to reduced hysteresis. Nevertheless, in the p++ mode a rather large number of consecutive V_g pulses of the same polarity are applied to the gate (see inset in Fig. 5.1(a)), which, according to the assumed me-
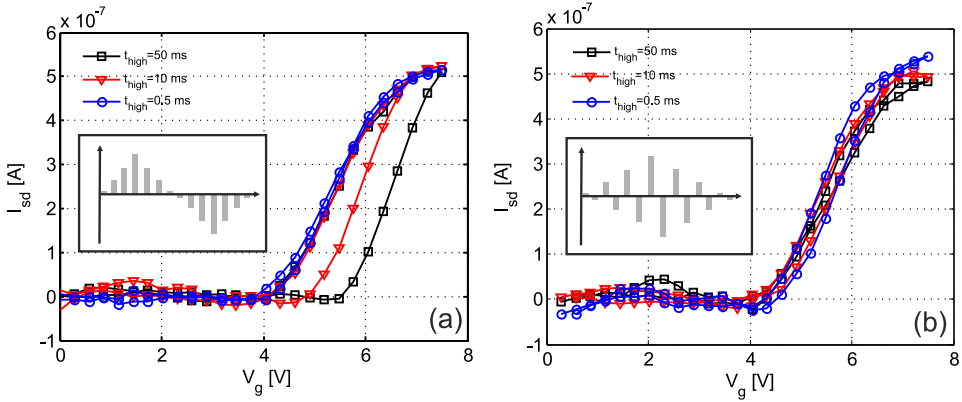
Figure 5.1: Gate characteristics of a CNFET sensor in synthetic dry air recorded with pulsed p++ V_g sweeps (a) and p+- V_g sweeps (b). Adapted from [67]. Copyright Institute of Physics and IOP Publishing 2010.

chanism, may still cause accumulation of trapped charges. In order to check this widely used explanation of hysteresis reduction, a different pulsed measurement mode, labeled p+- and illustrated the inset of Fig. 5.1(b), is proposed.

According to the assumed hysteresis mechanism in steady state, by applying after each positive V_g pulse a pulse of the same duration and amplitude but of negative polarity, the charge traps filled during the positive V_g pulse should be again discharged during the immediately following negative one. As a consequence the gate hysteresis should become independent of t_{high} and the sweep rate (SR) of the applied V_g pulses. Fig. 5.1(b) shows the I_dV_g characteristics recorded in synthetic dry air with the p+- mode for the pulse times t_{high} = 50, 10 and 0.5 ms. Indeed, in contrast to the characteristics recorded with the p++ mode, the observable hysteresis is almost independent from t_{high} and the observed gate hysteresis is constant at around 0.3 V.

New Pulsed Mode

In Fig. 5.2 the extracted gate hysteresis width H in dry air and the values obtained with the hysteresis model (introduced in section 2.2.3) for both pulsed measurement modes p++ and p+- for t_{high} = 50, 10, 5, 1 and 0.5 ms are shown. The error bars take into account the double standard deviation obtained from results of eight different CNFET characteristics. The dashed lines connect the hysteresis mean values. For the p++ mode a clear trend of smaller gate hysteresis for shorter V_g pulses is visible for both measurements and simulation results. For t_{high} = 10 and 5 ms (in the middle of the t_{high} range) the model predicts a more aggressive reduction of the gate hysteresis, while good agreement of the measurements and the model is achieved for the hysteresis at t_{high} = 50, 1 and 0.5 ms. For the mea-

p++ vs. p+- vs. Hysteresis Model
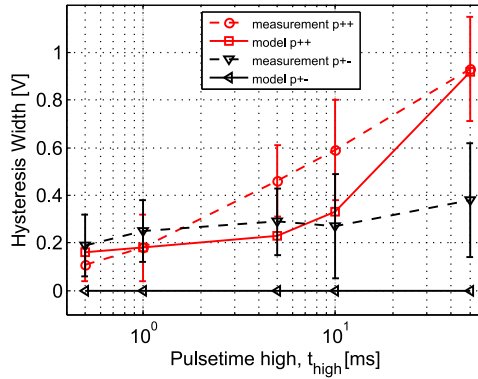
Figure 5.2: Hysteresis width H versus pulse time high (t_{high}) for the p++ and p+- modes measured data and simulation results. Adapted from [67]. Copyright Institute of Physics and IOP Publishing 2010.

surements with the p+- mode the gate hysteresis is nearly independent from the pulse time t_{high} (except for t_{high} = 50 ms), compared to the gate hysteresis with the p++ mode. This trend is confirmed by the model, which, however, predicts no gate hysteresis at all for all applied pulse times t_{high}. The standard deviation of the measurement data for the p++ and p+- mode are similar for all V_{th} pulses, except for t_{high} = 0.5 ms, it is about twice as large with the p+- mode compared to the p++ mode. The mean minimal hysteresis width H is comparable for both pulsed modes: 0.11 V for the p++ mode and 0.19 V for the p+- mode.

Discussion

p++ vs. p+-   The hysteretic behavior of CNFETs has been attributed to impurities and structural defects in the gate stack dielectrics but also adsorbed molecules close to the SWNT channel, which act as traps for charges emitted by the SWNT at high gate potentials. By applying V_g in the form of short voltage pulses, the time for charge traps to be filled is shortened and the gate hysteresis is reduced. In the p++ mode a rather large number of consecutive V_g pulses of the same polarity is applied to the gate which, according to the assumed hysteresis mechanism, may still cause accumulation of trapped charges. In contrast in the p+- mode, by applying after each positive V_g pulse a pulse of the same duration and amplitude but of negative polarity, the charge traps filled during the positive V_g pulse are discharged by the following negative one. As a consequence the gate hysteresis becomes independent of t_{high}.

From the measurement and simulation results shown in Fig. 5.2, we see that the rather simple hysteresis model gives a good qualitative representation of the hysteretic behavior of our CNFETs. The disagreement between the model and the CNFET measurements for the mid-range of t_{high} (5 and 10 ms) in the p++ mode are likely to stem from the model limitations enumerated in the methodology section 2.2.3. Basically, both the field emission model and the spatial distribution of the charge traps influence the profile of the hysteresis characteristic. Further refinements are thus required to render the model quantitative. However, a more severe disagreement concerns the p+- mode, for which the measurement data shows residual hysteresis while the model predicts zero hysteresis (Fig. 5.2). We speculate that the residual gate hysteresis in the measurements is coming from $1/f$ V_{th} fluctuations due to fluctuating charge trap filling levels in the vicinity of the SWNT channel. This mechanism is closely related to the model proposed by Tersoff *et al.* [143] to explain $1/f$ I_d fluctuations in CNFETs. Intuitively, one would expect V_{th} fluctuations of the forward and backward sweep to result in a fluctuating hysteresis width of both negative and positive sign, averaging to 0 V. However, throughout all measurement data only positive or close to zero gate hysteresis was observed (see e.g. Fig. 5.2). The model itself is not taking into account any charge fluctuations and is only a rate equation, giving the average evolution of the charge trap filling level in time. To see how hysteresis width fluctuations and filling level fluctuations relate, we artificially perturbed the steady state filling level symmetrically in positive and negative directions. With these perturbed initial conditions, the model always results in non-negative gate hysteresis, in agreement with the measurement data. Consequently, averaging over fluctuating non-negative hysteresis widths can result only in a positive residual hysteresis. Assuming that the proposed mechanism, explaining the residual gate hysteresis, is valid, then further lowering of the pulse time t_{high} in the p++ mode would not result in any further hysteresis width reduction. The hysteresis widths measured with the two pulsed modes roughly intersect at t_{high} = 0.5 ms, as can be seen in Fig. 5.2. It would then be interesting to lower t_{high} below 0.5 ms and see whether the two pulsed measurement modes saturate to the same residual hysteresis level. This would be an additional argument in favor of the proposed noise-induced residual hysteresis. Unfortunately, amplifier bandwidth limitations currently hinder us from testing this hypothesis.

Hysteresis Model

$1/f$ V_{th} Fluctuations

Summary

Pulsed V_g sweeps can be used to reduce gate hysteresis in dry air conditions in CNFET sensors with exposed CNT channels and ALD Al_2O_3 passivated metal contacts. In addition to the state-of-the-art p++ V_g mode, a new V_g waveform of

alternating polarity pulses (p+-) is proposed and successfully tested for hysteresis reduction. Compared to the p++ mode, the p+- sequence shows very similar hysteresis reduction capabilities but with highly relaxed constraints with regards to the pulse duration. According to the hysteresis model, the residual hysteresis is likely to be due to charge fluctuations in the vicinity of the SWNT channel.

5.2 Pulsed V_g for hysteresis reduction during NO$_2$ sensing

Motivation

We have seen in the previous section that pulsed V_g sweeps (p++ and p+-) can be used to reduce gate hysteresis in CNFET sensors with passivated metal contacts and exposed CNT channel in synthetic dry air. However, the pulsed methods have not yet been systematically investigated for the purpose of hysteresis reduction in the chemical sensing context. While Chang *et al.* [144] reported long V_g pulses (of the order of several seconds) to cause analyte desorption and to refresh CNT-based sensors, very recently Ervin *et al.* [145] identified the apparent sensor refreshing to be a measurement artifact coming from gate hysteresis. Thus, it is necessary to check whether short gate pulses reduce gate hysteresis in CNFET chemical sensors but do not interfere with analyte adsorption and desorption processes.

Analyte
Desorption

Results

In the following NO$_2$ gas detection experiment, CNFET sensors are exposed to 50, 100, 200 and 1000 ppb of NO$_2$. The $I_d V_g$ characteristics of a CNFET sensor captured with continuous V_g sweeps are shown in Fig. 5.3(a), upon pulsed p++ sweeps ($t_{high} = 0.5$ ms) in Fig. 5.3(b) and upon pulsed p+- sweeps ($t_{high} = 0.5$ ms) in Fig. 5.3(c). The $I_d V_g$ characteristics show a positive, concentration-depended shift upon exposure to NO$_2$, independent of the applied V_g sweeping mode. While the $I_d V_g$ characteristics recorded with continuous V_g sweeps show substantial gate hysteresis, the characteristics measured with pulsed V_g sweeps (p++ and p+-) are essentially hysteresis-free. In Fig. 5.3(d), the minimum V_{th} value of the forward sweeps and the maximum V_{th} value of the backward sweeps for each mode are extracted. Connecting the data points encloses a certain area (shaded area in Fig. 5.3(d)), within which V_{th} is fluctuating for each measurement mode. While the largest area of uncertainty for the position of V_{th} is observed for the continuous mode, the two pulsed modes show sensor characteristics (note the two different y axes) with small enclosed areas. The concentration-dependent positive shifts of V_{th} measured with both pulsed modes are smaller compared to the shifts observed

Positive
V_{th} Shifts

Area of
Uncertainty

with the continuous mode.

Discussion

All CNFET $I_d V_g$ characteristics, most notably the heavily shifted characteristics upon exposure to 200 and 1000 ppb of NO_2, show a current I_d, which seems to saturate for V_g close to + $V_{g,max}$. This apparent I_d saturation is, in our opinion, not a common FET saturation, but is observed due to enhanced field emission from the SWNT into the underlying oxide traps at high V_g. Assume that initially at $V_g = 0$ V no charges are trapped. For small positive V_g the electric field (E) at the SWNT channel is too small for electron injection to take place. For larger positive V_g and hence also larger E, electron injection from the SWNT channel into the oxide begins. The trapped electrons partially screen the applied positive V_g, which is equivalent to a decreased gate coupling. As qualitatively seen from simulation results (Fig. 5.4) for the continuous mode, ϕ_{ext} starts to saturate for 5.9 V < V_g < 7.5 V to about 5.85 V. Consequently, no further increase of I_d should be observable in the CNFET gate characteristic and I_d seems to be in saturation, which is indeed measured. Since fewer charges get trapped with the pulsed modes, the electrostatic shielding of V_g is less pronounced than with the continuous mode. ϕ_{ext} then saturates to a higher value of around 6.2 V for 6.6 V < V_g < 7.5 V, as seen in Fig.5.4 (dashed versus continuous line). This translates into an improved gate coupling with the pulsed modes, leading to a compression of the CNFET characteristics along the V_g axis. This has some practical advantage since large shifts of V_{th} due to high NO_2 concentrations are still visible within the applied V_g window [-7.5 V, +7.5 V] (enhanced measurement range), as is indeed observed in Fig. 5.3(d).

Apparent I_d Saturation

Improved Gate Coupling

Shaded areas in Fig. 5.3(d) were initially intended to represent uncertainty areas for the intrinsic V_{th} location. By changing the measurement mode from continuous to pulsed, the gate hysteresis is reduced but not without changing the gate coupling, as discussed above. Indeed, as can be observed for the pulsed modes their shaded areas are located at the lower end or outside the shaded area of the continuous mode. Then, V_{th} of the forward or backward sweep or the average of the two is not approximating the intrinsic V_{th} well. Using any V_{th} derived from a continuous mode characteristic (with significant hysteresis) as sensor output signal is not necessarily an invalid procedure but the physical meaning of such signals demands further clarification. In contrast, extracting V_{th} from pulsed mode characteristics produces a better approximation of the intrinsic V_{th}, which physically reflects the Fermi level shifts due to gas exposure as discussed in section 2.3.2.

Intrinsic V_{th}
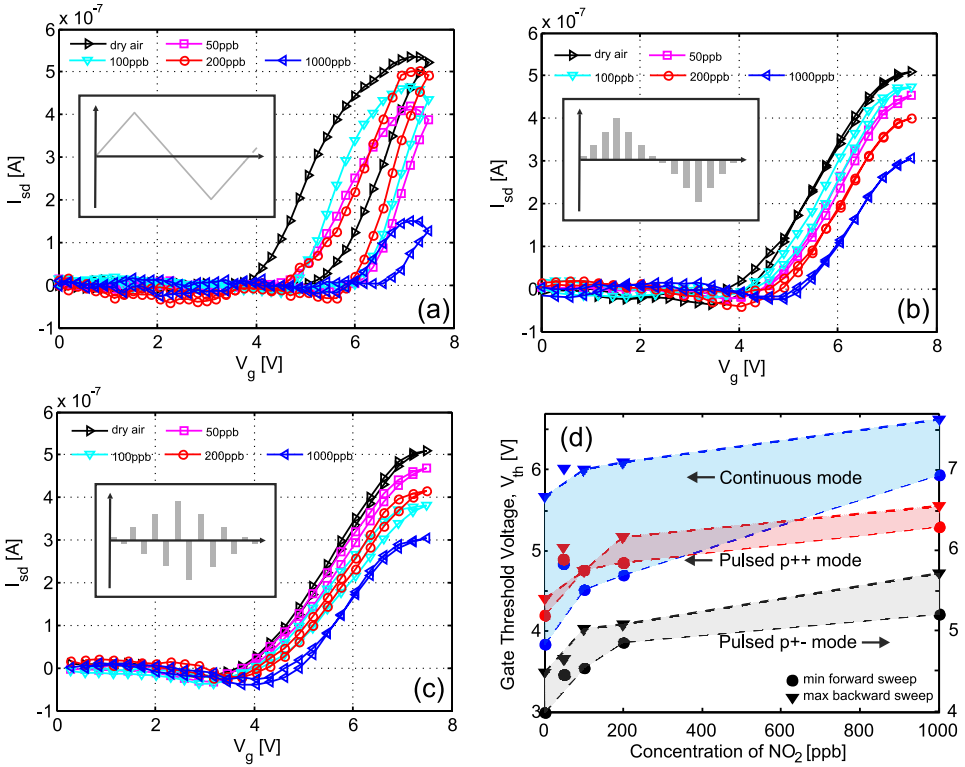
Figure 5.3: CNFET $I_d V_g$ characteristics recorded with continuous (a), pulsed p++ (b) and pulsed p+- (c) sweeps (t_{high} = 0.5 ms) upon exposure to synthetic dry air, 50, 100, 200 and 1000 ppb of NO_2. V_{sd} = 30 mV. (d) NO_2 concentration levels versus min/max V_{th} values extracted from CNFET characteristics recorded with continuous V_g, the p++ mode and the p+- mode (t_{high} = 0.5 ms). The right axis is shifted downwards by 1 V with respect to the left axis for clarity to avoid overlap of the shaded areas of the p++ and the p+- modes. Adapted from [67]. Copyright Institute of Physics and IOP Publishing 2010.
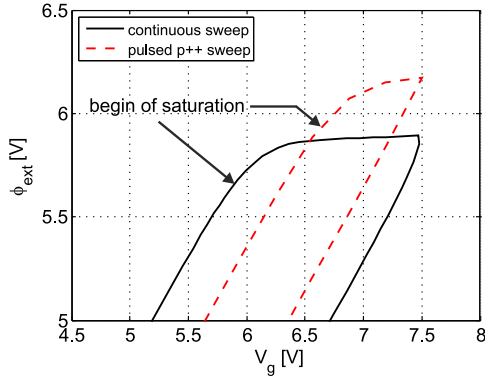
Figure 5.4: Zoom-in of a plot of V_g versus the external potential ϕ_{ext} generated with the hysteresis model for continuous and pulsed (p++) V_g. Since fewer charges are trapped and therewith the electrostatic shielding of V_g is smaller with the pulsed compared to the continuous mode, higher ϕ_{ext} can be achieved, leading to an improved gate coupling. Adapted from [67]. Copyright Institute of Physics and IOP Publishing 2010.

Chang *et al.* [144] have shown sensor recovery achieved with long V_g pulses. However, opposed to those reported results, in all measured CNFETs with encapsulated contacts no negative shift of V_{th}, which would be the signature of sensor reset, is observed, even though the pulse waveforms are repeated for several times. Referring to the study by Chang *et al.*, Ervin *et al.* [145] recently published a study in which they conclude that the apparent sensor refreshing is most probably due to a gate hysteresis artifact. Indeed, as we will see in the following section 5.3, applying relatively long V_g pulses of negative polarity and high amplitude to the gate electrode, discharges electrons from the traps close to the SWNT channel. The additional electrostatic potential created by the trap states leads to a rigid negative shifts of the $I_d V_g$ characteristic, which is exactly the same signature we would expect from NO_2 desorption. Our measurement data also supports the finding by Ervin *et al.* that the reported sensor refreshing by V_g pulses is an artifact caused by gate hysteresis effects. To refresh our CNFET NO_2 sensor they can be stored in ambient for about 24 hours or heated for accelerated NO_2 desorption, as described in section 4.2.4.

Apparent Sensor Refreshing

Hysteresis Artifact

Summary

Pulsed V_g sweeps can be used for hysteresis reduction and measurement range enhancement (due to an enhanced gate coupling) in CNFET NO_2 sensors. Due to the reduced gate hysteresis with pulsed V_g sweeps, extraction of the intrinsic

V_{th}, used as sensor output signal, becomes more reliable than with continuous V_g sweeps. Thus, pulsed V_g sweeps can lead to more clearly interpretable sensor output signals and more repeatable sensor operation. No resetting of the CNFET $I_d V_g$ characteristics upon applying short V_g pulses was observed with our devices.

5.3 CNFET sensor initialization

Motivation

Gate Hysteresis

As we have seen so far, CNFETs typically suffer from substantial gate hysteresis supposably due to trapped charges in the vicinity of the SWNT channel. At high gate voltages, the electric field is enhanced at the SWNT channel due its small diameter as explained in section 2.2.3. At these very high electric fields strengths electrons are emitted from the SWNT channel and can get trapped in the underlying gate oxide or in layers of adsorbed molecules on the SWNT channel (e.g. H$_2$O). When measuring the I$_d$V$_g$ characteristics of a CNFET $V_g$is swept back and forth between - $V_{g,max}$ and + $V_{g,max}$. During V_g sweeps, since they consist of both positive and negative V_g values, the charge traps near the SWNT channel are partially filled and partially emptied. When the CNFET measurements are paused and after a certain time started again, the charge trap traps are in an unknown state, since they are naturally slowly detrapped again at V_g = 0 V [39]. Trapped charges

Trapped Charges

create an electrostatic potential, which acts in addition to the applied V_g on the CNT channel and becomes apparent as a rigid shift of I$_d$V$_g$ characteristics. This phenomenon is especially a problem for CNFET based sensors, which rely on the threshold voltage as their sensor signal. In this section we demonstrate the effectiveness of V_g pulse sequences for the purpose of initialization and erasure of electrical history in hysteretic CNFETs.

Experiment

V_g Pulse Sequence

The applied V_g sequence to test the electrical initialization of CNFETs is shown in Fig. 5.5. It consists of a charging pulse (CP), probe (Px) TAPs and initialization (Ix) TAPs. TAPs stands for Triangular Ambipolar Pulses and is essentially one p+-sweep. The CP has a constant amplitude (+/- 7.5 V) and variable duration (t_c = 1, 10, 100 ms and 1 s). As such, a CP is supposed to emulate electrical device history. Px TAPs are supposed to probe V_{th} and have an amplitude as small as possible in order to not affect the electrical device state, while still allowing for reliable extraction of V_{th} from the I$_d$V$_g$ characteristics. Ix TAPs are supposed to erase the device history. Each Ix TAP is followed by a Px TAP to probe V_{th} and hence the electrical state of the CNFET. With this sequence the progress of electrical initialization
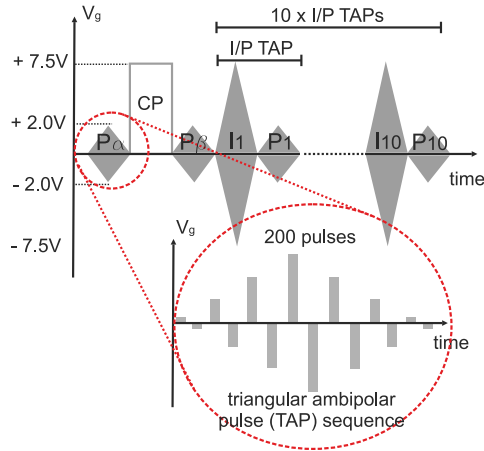
Figure 5.5: Schematic of the applied gate voltage (V_g) sequence used for the study of electrical initialization. It consists of a charging pulse (CP), probe (Px) triangular ambipolar pulse (TAP) sequences and initialization (Ix) TAPs. The CP has a constant amplitude (+/- 7.5 V) and variable duration (t_c = 1, 10, 100 ms and 1 s). As such, a CP is supposed to emulate device history. Px TAPs are supposed to probe V_{th} without affecting the electrical device state, whereas Ix TAPs are supposed to erase the device history. TAPs consist of 200 pulses of 0.5 ms each and maximum amplitudes of +/-2 V and +/-7.5 V for Px and Ix, respectively. Between two consecutive pulses V_g returns to 0 V for 0.1 ms. Adapted from [142]. Copyright Elsevier Ltd 2010.

can be checked and the number of required Ix TAPs for full electrical initialization can be determined. The electrical initialization is tested with fully passivated CNFETs. First, because fully passivated CNFETs are less prone to unwanted environmental influences such as changes in the ambient atmosphere and changes of the humidity level, than CNFETs with exposed SWNT channels. Second, V_{th} of fully passivated CNFETs is close to 0 V. This allows Px TAPs of rather small amplitude. On the contrary, CNFETs with exposed SWNT channels typically feature V_{th} values in a range between + 2 and + 4 V due to a decreased oxygen doping, as explained in section 4.2.2. In order to be able to reliably extract V_{th} values from such devices V_g sweeps between +/- 5 V are required. A V_g sweep of such high amplitude is not suitable as Px TAP since it would influence the charge trap filling level around the SWNT channel imposed by the CPs and distort the outcome of the experiment.

Fully Passivated CNFET
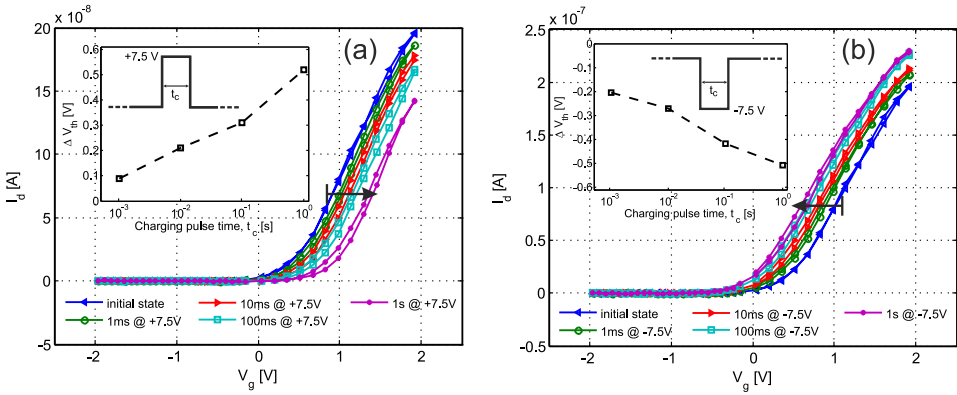
Figure 5.6: CNFET gate characteristics before and after positive (a) and negative (b) CPs of 7.5 V amplitude and t$_c$ = 1, 10, 100 ms and 1s. V_{sd} = 30 mV. Adapted from [142]. Copyright Elsevier Ltd 2010.

Results

V_{th} shifts

In Fig. 5.6 the effect of positive and negative CPs applied to the back gate electrode on a CNFET $I_d V_g$ characteristic is shown. The characteristic recorded before the CPs are applied (Pα) reflects the initial electrical state of the CNFET. The characteristics measured during the PS (Pβ) after the CPs of 1, 10, 100 and 1000 ms duration show the impact of the CPs. Positive (negative) CPs cause positive (negative) shifts of V_{th}, which monotonically depend on the CP duration t$_c$ (see inset of Fig. 5.6(a,b)). Fig. 5.7 displays the shifts of V_{th} (extracted values from Fig. 5.6) upon applying the entire pulse sequence shown in Fig. 5.5 of each four positive and negative CPs. The initial states (Pα) fluctuate within a band of about +/- 0.1 V. As seen in Fig. 5.6 positive (negative) shifts of V_{th} are visible upon positive (negative) CPs. After the first I TAP, almost all V_{th} values are restored, except for the negative CP of t$_c$ = 1000 ms duration. At the latest after the second I TAP, all V_{th} values are restored completely. For the subsequent I/P TAPs the extracted V_{th} values fluctuate within a similar band as before the CPs were applied of about +/- 0.1 V.

Discussion

Shifts of V_{th}

The shifts of V_{th} in Fig. 5.6(a) and (b) can be understood assuming a simple charging/discharging mechanism of the charge traps near the SWNT channel. Upon positive CPs the charge traps near the SWNT channel get partially filled with electrons. These trapped electrons contribute an additional negative potential,
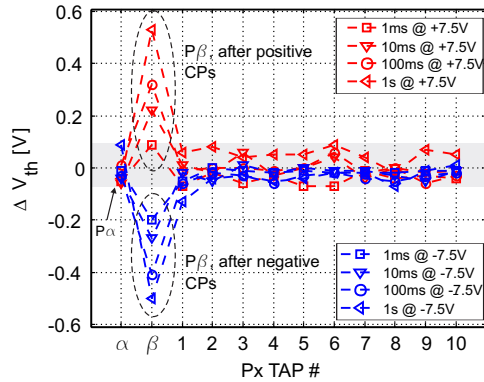
Figure 5.7: ΔV_{th} after applying the V_g sequence shown in Fig. 5.5. (Labels on x-axes are defined in Fig. 5.5). Adapted from [142]. Copyright Elsevier Ltd 2010.

which appears as a positive V_{th} shift in the gate characteristics during the following probe sweep (Pα). For negative CPs the charge traps are partially emptied, which creates a positive electrostatic potential in addition to the applied V_g, causing a negative shift of the $I_d V_g$ characteristic.

We believe that the dependency of V_{th} shifts on the charging time t_c comes from the distribution of SWNT-charge trap distances, with further traps being filled only at longer CPs. This understanding is in good agreement with Trap Spectroscopy by Charge Injection and Sensing (TSCIS) techniques where charge injection times are varied to determine the physical charge injection distance. With this information the charge trap distribution can be obtained, which is typically necessary to understand performance and reliability of flash-type memory devices [146].

Charging Time

The V_{th} fluctuations observed before and after the CPs (Fig. 5.7) can be understood by considering intrinsic potential fluctuations from charge traps close to the SWNT channel. In a CNFET, the SWNT channel is extremely narrow and a single charge can be within a few nm of every point across the cross section of a SWNT channel [143], highly affecting the current in sections along the channel.

V_{th} Fluctuations

Summary

Independent of the polarity and the duration t_c (tested from 1 ms to 1 s) of the CPs, the I TAPs (p+- sweeps) have been demonstrated to erase the device's electrical short-term history completely. Therefore, I TAPs can be used to electrically initialize CNFETs before each probing of V_{th} as sensor output.

5.4 Summary and conclusion

Synthetic Dry Air

In summary, we first have successfully tested pulsed V_g sweeps for hysteresis reduction in our CNFET sensors in synthetic dry air, resulting in essentially hysteresis-free $I_d V_g$ characteristics for $t_{high} \leq 1$ ms. Following the concept of charge trapping as the proposed main reason for gate hysteresis, a new pulsed waveform was introduced. It consists of pulses of alternating polarity (p+-) and was found to be more efficient in reducing gate hysteresis compared to the original p++ mode, especially for longer pulse times ($t_{high} > 1$ ms). Additionally, the comparison of the measurement results and data obtained from a hysteresis model revealed good qualitative agreement.

NO₂ Sensing

In the second set of experiments the pulsed V_g modes were applied for hysteresis reduction during NO₂ sensing. The $I_d V_g$ are almost hysteresis-free and show concentration-dependent positive shifts upon NO₂ exposure, as it is observed in $I_d V_g$ characteristics recorded with continuously swept V_g. Due to an improved gate coupling with the pulsed V_g mode, the shifts are smaller than with the continuous V_g mode, which results in an enhancement of the sensor measurement range. Upon the applied V_g pulses no sensor reset was observed.

Sensor Initialization

Finally, the p+- waveforms were demonstrated to to erase short-term electrical history in CNFET sensors and can therefore be used to electrically initialize CNFET devices before extracting V_{th} as the sensor output signal. As such, electrical initialization may help to improve the sensor's reliability and repeatability.

At the end of this chapter we have established a method to reduce gate hysteresis, which is fully compatible with NO₂ sensing and as such comes without any structural and chemical changes of the CNFET sensors. It significantly improves the reliability of the sensor device by allowing a more precise estimate for the intrinsic position of V_{th}, which is primarily the sensor output signal.

6 Influence of external parameters

6.1 Introduction

Most experiments on CNFET (chemical) sensors have been conducted in well controlled laboratory conditions (controlled (inert) atmosphere, vacuum) or in some studies the exact conditions were not clearly specified. One environmental parameter, which is known to play an important role for any kind of real-life application, is the ambient humidity level. It was shown by Kim *et al.* [60] that with increasing ambient humidity level, gate hysteresis in $I_d V_g$ characteristics of PMMA-coated CNFETs increases gradually. They attributed the increase of hysteresis to an increasing number of permeating H_2O molecules through the PMMA layer at higher humidity levels. H_2O can then act as charge traps in the vicinity of the SWNT channel, causing increased gate hysteresis. Except the study by Kim *et al.* no systematic experimental investigation on the influence of adsorbed H_2O molecules on CNFET $I_d V_g$ characteristics has been conducted yet. Humidity

Another external parameter by which CNFET sensors are potentially influenced in real-life applications is temperature. Most experiments for CNFET sensors have been conducted at RT. To explore fundamental physical properties of SWNTs, CNFETs have been typically electrically characterized at cryogenic temperatures [147, 148]. However, this low temperature regime is not relevant for CNFETs operated as chemical sensors. Instead, the temperature range above RT is relevant for CNFET chemical sensors. Due to the essentially chemically inert structure of SWNTs, they can be envisioned being highly suitable as sensing material employed in sensors operated in harsh and as such maybe also hot environments. Temperature

In this chapter we first explore the influence of humidity on $I_d V_g$ characteristics of CNFET sensors in synthetic air and also during NO_2 sensing. In the second part the influence of temperature (T = 300 - 390 K) on a fully passivated CNFET is investigated. Both parts are incomplete in the sense of being full cross-sensitivity studies with respect to humidity and temperature. This chapter focuses mainly on the first order effects of humidity and temperature on $I_d V_g$ characteristics. Content

Parts of this chapter were published in [149].

6.2 Influence of humidity

6.2.1 Synthetic air

Motivation

Kim *et al.* reported increased gate hysteresis with increasing relative humidity level in their CNFETs. We first want to check whether increased gate hysteresis upon exposure to humidity is also observed in our CNFET sensor structures with synthetic air as carrier gas. As we have seen in chapter 5 pulsed V_g sweeps can be used to reduce gate hysteresis in dry conditions. We also want to check whether pulsed V_g modes are capable to reduce gate hysteresis in humid environment. Whether adsorbed H_2O molecules have any additional effects on the I_dV_g characteristics than increased gate hysteresis was not addressed by Kim *et al.* According to an ab-initio study by Sung *et al.* [150], H_2O seems not to interact with the SWNT channel via charge transfer. This theoretical result needs to be verified in experiment, as H_2O induced shifts of I_dV_g characteristics would be very likely to interfere with the signature of NO_2 adsorption/desorption.

Pulsed V_g

Experiment

The CNFET NO_2 sensors are exposed to relative humidity (r.h.) levels (60 min duration each) of 0, 10, 20, 30, 40, 50 and 60 % with synthetic air as carrier gas at RT. In between two humidity levels the measurement chamber is flushed with synthetic dry air for 60 min. The I_dV_g characteristics are recorded with continuous V_g and with both pulsed p++ and p+- modes, as introduced in section 3.2.2.

Results

The I_dV_g characteristics measured with continuous V_g is shown in Fig. 6.1(a). The gate hysteresis width for 0 and 30 % r.h. is significantly smaller (H ≈ 0.5 V) compared to the gate hysteresis width upon exposure to 60 % r.h. (H ≈ 4 V). In Fig. 6.1(d) the extracted hysteresis values for all humidity levels are given with a clear trend of increasing gate hysteresis upon increasing humidity level. For both pulsed modes, the extracted gate hysteresis is smaller for all humidity levels compared to the continuous V_g sweeps (Fig. 6.1(b) and (c)). Both pulsed modes show comparable hysteresis reduction performance, as observed in dry conditions (section 5.1), Upon 50 and 60 % r.h. the p+- mode appears to be slightly more efficient in reducing gate hysteresis than the p++ mode, as seen in Fig. 6.1(d) The I_dV_g characteristics at 60 % r.h. despite the V_g measurement mode seem to be negatively shifted along the V_g axis.
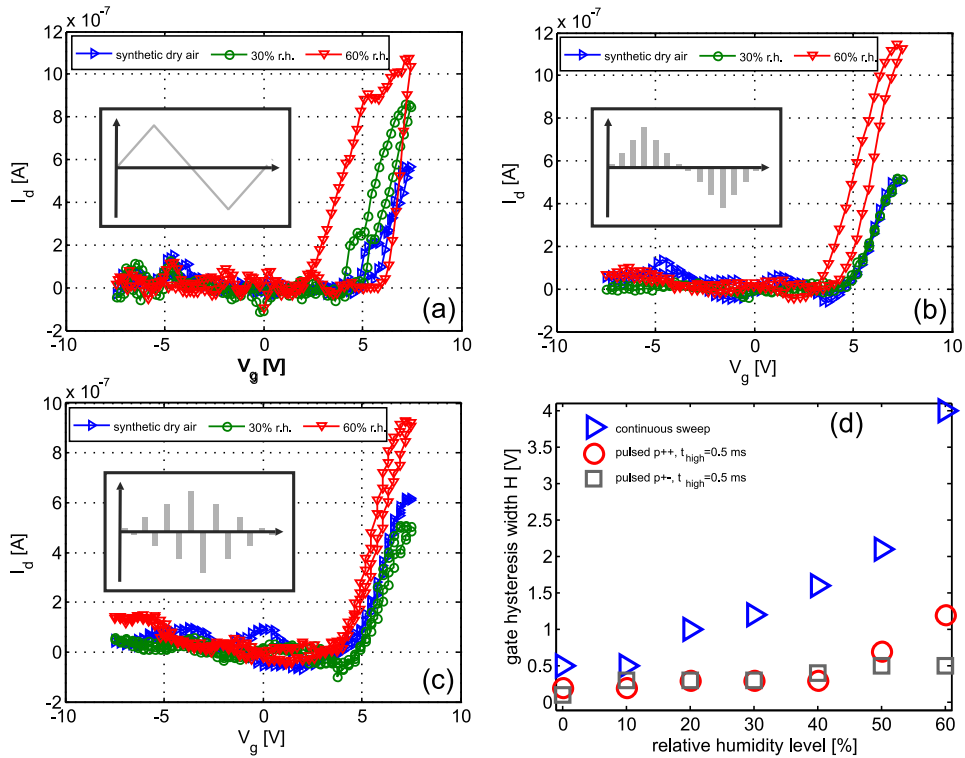
Figure 6.1: CNFET $I_d V_g$ characteristics recorded with continuous (a) pulsed p++ (b) and p+- (c) V_g mode (t_{high} = 0.5 ms) upon exposure to 0, 10, 20, 30, 40, 50 and 60 % relative humidity with synthetic air as carrier gas. The humidity levels are of 60 min duration each, interrupted by 60 min of flushing with synthetic dry air. For the sake of clarity only the $I_d V_g$ characteristics for 0, 30 and 60 r.h. are show in each plot. Extracted gate hysteresis values for all applied humidity levels and V_g modes (d).

Discussion

In agreement with the results observed by Kim *et al.*, the CNFET NO_2 sensors also show increased gate hysteresis upon exposure to increasing humidity levels for continuously swept V_g. Following their discussion, H_2O molecules adsorbed on or near CNFET channels seem to act as charge traps, causing hysteresis in the $I_d V_g$ characteristics of CNFET NO_2 sensors.

p++ vs. p+- As previously demonstrated in section 5.1 by applying V_g in the form of short voltage pulses, the time for charge traps to be filled is shortened and the gate hysteresis is reduced. For the humidity levels of 50 and 60 % r.h. both pulsed modes, but especially the p++ mode, show slightly increased gate hysteresis. This is most probably due to an increased density of charge traps near the SWNT resulting from more adsorbed H_2O molecules at higher humidity levels. The differences of the two pulsed p++ and p+- modes with respect to hysteresis reduction capability will be discussed in more detail in section 6.3.1.

V_{th} shifts We now want to discuss shifts of the $I_d V_g$ characteristics along the V_g axis upon H_2O adsorption. In the course of this study, some CNFET sensors were observed, which responded with positive shifts of the $I_d V_g$ characteristics upon exposure to humidity, some with negative shifts and some devices did not show any change at all. As such, the negative shifts of the $I_d V_g$ characteristics upon exposure to 60 % r.h. in Fig. 6.1 can not be considered a typical case. Similar to shifts of $I_d V_g$ characteristics induced by NO_2 adsorption, the observed shifts could be the signature of doping of the SWNT due to H_2O adsorption. This issue has been investigated by numerous theoretical studies so far with mostly contradicting results. However, in the latest ab-initio study by Sung *et al.* [150] about the effect of H_2O adsorption on CNFETs, they find that H_2O molecules affect the electronic structure of a SWNT deep in the valence band but should have a negligible effect on the electronic structure near the Fermi level. They conclude that charge transfer between H_2O molecules and a (10,0) s-SWNT is not a relevant mechanism of the physisorption of H_2O on a SWNT. Considering the results of Sung *et al.* and our observations of non-monotonic shifts of $I_d V_g$ characteristics upon humidity exposure, it seems that the interaction between the H_2O and SWNTs is of indirect nature possibly via an increased density of charge traps upon H_2O adsorption. As we will see in the next chapter, fluctuations of the filling level of charge traps can translate into considerable fluctuations of V_{th}. This phenomenon might be responsible for the observed positive and negative shifts upon H_2O adsorption.

Summary

The $I_d V_g$ characteristics of CNFET NO_2 sensors, recorded with continuous V_g, show increased gate hysteresis with increasing humidity level. On the other hand, pulsed V_g sweeps, especially pulsed p+- V_g sweeps, can be used to mostly reduce gate hysteresis at high humidity levels, demonstrated up to 60% r.h. The observed shifts of the CNFET gate characteristics upon humidity exposure are not understood yet and require further investigations. Based on our findings and the results from theoretical investigations concerning charge transfer between H_2O molecules and SWNTs, which would results in monotonic shifts of $I_d V_g$ characteristics, seems not to be a relevant interaction mechanism.

6.2.2 NO_2 detection in moderate humidity

Motivation

Since we have seen in the previous section that the pulsed p+- V_g sweeps are efficient in reducing gate hysteresis in humid conditions, we now want to check whether hysteresis-free NO_2 detection with CNFET sensors is possible in moderate humidity conditions. One reason for doing this is that the H_2O molecules adsorbed near the SWNT channel may change NO_2 adsorption on the SWNT channel, which may render the CNFET NO_2 sensors insensitive.

Experiment

After exposure to synthetic dry air for two hours the CNFET NO_2 sensors are exposed to 40 % r.h. in synthetic air for five hours to ensure steady state conditions. In the following, levels of 50, 100, 200, 400 and 800 ppb of NO_2 of 60 min duration each are added to the humid carrier gas.

Results

Fig. 6.2(a) shows CNFET $I_d V_g$ characteristics recorded with pulsed p+- sweeps (t_{high} = 0.5 ms) upon exposure to humid air (40 % r.h.) and NO_2 concentration levels . The $I_d V_g$ characteristics are essentially hysteresis-free and show NO_2 concentration dependent positive shifts as it was also observed in dry conditions (section 5.2). Fig. 6.2(b) shows V_{th} values (extracted from Fig. 6.2(a)) for the different NO_2 concentration levels. Starting from exposure to dry air conditions, the $I_d V_g$ characteristic is first negatively shifted when the CNFET sensor is exposed to humid air (40 % r.h.). The sensor characteristic shows a small area of uncertainty, comparable to NO_2 detection in dry conditions with pulsed V_g sweeps (Fig. 5.3).
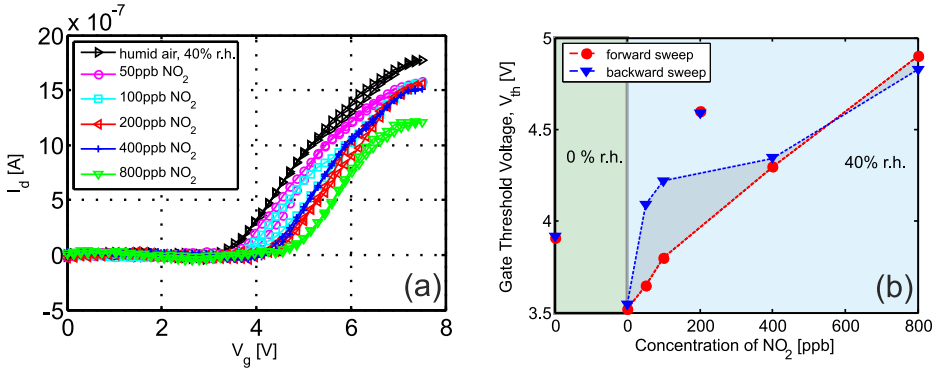
Figure 6.2: (a)CNFET $I_d V_g$ characteristics recorded with pulsed p+- sweeps (t_{high} = 0.5 ms) upon exposure to synthetic humid air (40 % r.h.), 50, 100, 200, 400 and 800 ppb of NO_2. V_{sd} = 30 mV. (b) NO_2 concentration levels versus min/max V_{th} extracted from CNFET $I_d V_g$ characteristics shown in (a).

Discussion

The CNFET sensors seem to feature qualitatively similar NO_2 detection behavior (with similar range of limit of detection (LOD) and sensitivity) in dry and moderately humid conditions. As such, the access for NO_2 molecules to the SWNT channel does not appear to be hindered by adsorbed H_2O molecules at 40 % r.h. The concentration dependent shifts of the $I_d V_g$ characteristic indicate that charge transfer between NO_2 molecules and the SWNT can still take place in the presence of humidity.

In Fig. 6.2(b) an outlier in the sensor characteristic for a NO_2 concentration of 200 ppb can be seen. This outlier might be explained by intrinsic V_{th} fluctuations, which will be discussed in the next chapter.

Summary

CNFET sensors show qualitatively similar NO_2 detection behavior in moderately humid conditions (40 % r.h.) and in dry air. The access for NO_2 molecules appears not to be hindered by adsorbed H_2O molecules and charge transfer between NO_2 molecules and the SWNT seems to be still present as sensing mechanism, as the rigid shift of V_{th} upon NO_2 exposure suggests.
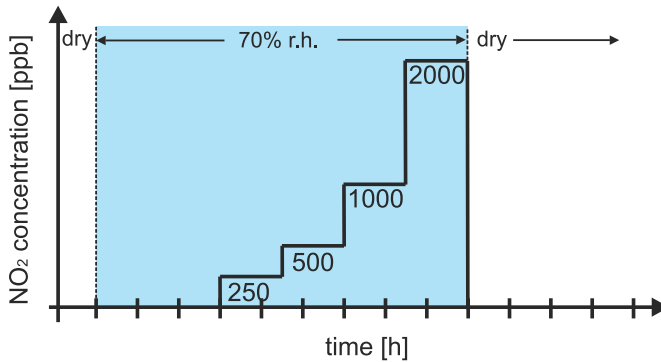
Figure 6.3: Schematic of the experiment of NO_2 sensing in high humidity.

6.2.3 NO_2 detection in high humidity

Motivation

In some real-life applications the CNFET NO_2 sensors may also be exposed to high (> 60% r.h.) humidity levels. We have seen that at moderate humidity the CNFET sensors show similar NO_2 detection performance as in dry conditions. However, it is documented in literature that at high humidity levels, but still far below 100 % r.h., molecular condensation of H_2O molecules on surfaces starts [151–154]. It needs to be verified whether molecularly condensated H_2O molecules on the chip and near the SWNT channel are compatible with the operation of our devices as NO_2 sensors.

Experiment

A schematic of the experiment of NO_2 sensing in high humidity is shown in Fig. 6.3. The CNFET NO_2 sensors are exposed to synthetic dry air for 1 hour followed by the addition of 70 % r.h. to the carrier gas for 9 hours. 3 hours after humidity is added, the sensors are exposed to NO_2 levels of of 250, 500, 1000 and 2000 ppb of 1.5 h duration each. After exposure to humidity and NO_2, the measurement chamber is again flushed with synthetic dry air for 4 hours. The $I_d V_g$ characteristics are measured with pulsed p+- V_g sweeps with a sampling time of 1 min.

Results

Fig. 6.4(a) shows the $I_d V_g$ characteristics of a CNFET NO_2 sensor in synthetic dry air and after 1, 3 and 7 min of addition of 70 % r.h. to the carrier gas. The

$I_d V_g$ characteristic in dry conditions is polar n-type and essentially hysteresis-free with $V_{th} \approx 3$ V. 1 min after addition of 70 % r.h. the $I_d V_g$ characterisitic shows a significantly increased gate hysteresis width (H $\approx$ 3 V) and the on-state current has dropped by about 50 % compared to the on-state current in dry conditions. After 3 min of exposure to 70 % r.h. the on-state current has further dropped by about 50 % and the n-type current branch features dips and is heavily distorted. Finally after 7 min, the n-type current branch is no longer visible and the entire $I_d V_g$ characteristic shows essentially no current.

The $I_d V_g$ characteristic for 2, 5, 7 and 9 hours of exposure to 70 % r.h. is shown in Fig. 6.4(b). I_d is linearly dependent on V_g: for $V_g > 0$ V I_d is positive and for $V_g < 0$ V I_d is neagtive. With longer exposure to humidity the measured I_d is increasing. Once the chamber is flushed with synthetic dry air I_d is again gradually decreasing in time but the CNFET $I_d V_g$ charateristic can not be restored, even after heat treatment for 1 h at 110 °C .

In Fig. 6.4(c) a SEM image of a CNFET NO_2 sensor after the entire experiment is shown. We can recognize the SWNT channel in the middle of the window in the Al_2O_3 passivation layer and the source and drain metal contacts. Different from an intact device, the metal contacts have dents, where the SWNT reaches the metal contacts (dashed circles) and also, the ALD Al_2O_3 is attacked at the SWNT channel, where it is normally covered. Further, the area near the SWNT channel is laced with particle-like debris.

Discussion

Increased Hysteresis

The polar n-type behavior, the low gate hysteresis and the positive V_{th} of the $I_d V_g$ characteristic recorded in dry conditions (Fig. 6.4(a)) are the signature of a CNFET NO_2 sensor with a SWNT channel exposed to the ambient and properly passivated SWNT metal interfaces. The substantial increase of the gate hysteresis width 1 min after addition of 70 % of r.h. to the carrier gas might be explained by a significant increase of the density of charge traps near the SWNT due to H_2O molecules adsorbed onto the SWNT or onto the underlying SiO_2. It seems that the density of charge traps is so high that even with the p+- pulsed V_g mode (t_{high} = 0.5 ms) gate hysteresis can not be suppressed anymore. The exact reason for the distorted $I_d V_g$ characteristic after 3 min and the finally completely flat characteristic after 7 min is not fully understood yet. However, with the data shown in Fig. 6.4(b) we can speculate that in the course of exposure to 70 % humidity more and more H_2O molecules adsorb on the sensor surface and start forming an increasingly conductive layer between the exposed SWNT channel and the Si substrate gate electrode. This hypothesis is supported by the high current levels of I_d measured (upon addition of humidity) and its polarity, which is changing with the
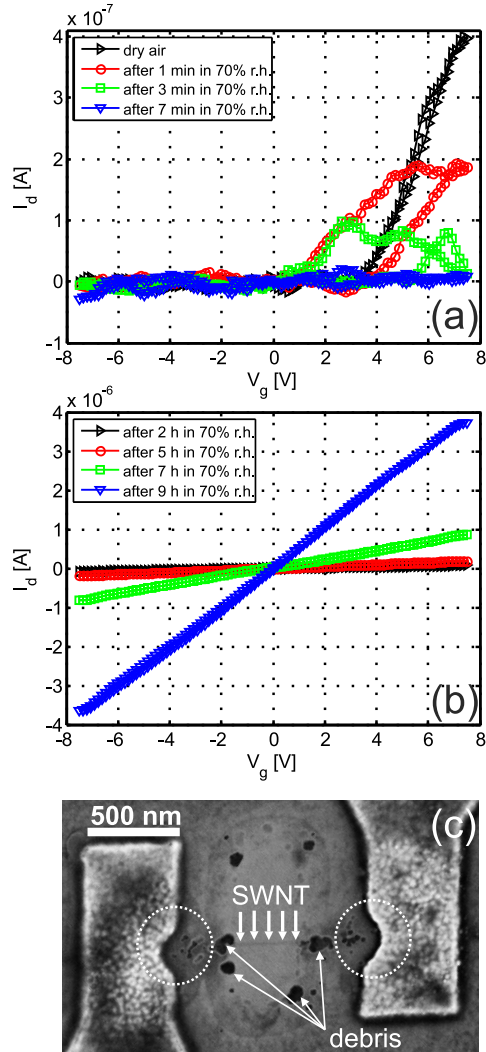
Figure 6.4: (a) CNFET $I_d V_g$ characteristics recorded with pulsed p+- sweeps (t_{high} = 0.5 ms) upon exposure to synthetic dry air and after 1 min and 7 min of addition of 70 % r.h. V_{sd} = 30 mV. (b) SEM image of a CNFET NO$_2$ sensor after the experiment.

Molecular
Condensation

polarity of V_g. Different from our general understanding affected by the macroscopic world, in which condensation of water is assumed to take place at only humidity levels close to 100 % r.h., in the microscopic regime molecular water adsorption at humidity levels far below 100 % r.h. have been reported [151–154].

Electro-
chemical
Process

While the $V_{sd} = 30$ mV, V_g reaches up to ± 7.5 V. The presence of H_2O and the fact of high electrical potential differences of several volts between the SWNT channel and the gate electrode suggests that most probably an electrochemical process takes place at the sensor surface in the presence of water. The most obvious might be electrolysis of water [155], which requires a potential difference of only 1.23 V between the anode and the cathode. As the polarity of V_g is changing with every applied pulse, the exposed section of the SWNT channel constantly switches from acting as anode and cathode. During electrolysis of water H^+ cations accumulate at the anode and OH^- anions accumulate at the cathode. As a result, the water near the anode is acidic and near the cathode it is basic. The acidic and/or basic solution may then attack the ALD Al_2O_3 layer near the SWNT channel until the source and drain metal electrodes are exposed and also get eventually attacked. This could explain the dents in the metal electrodes, as seen in the dashed circles in Fig. 6.4(c) and the debris near the SWNT.

Raman

In addition to electrical measurements, also Raman spectroscopy (data not shown here) was performed. Compared to the Raman spectrum of a section of the same SWNT passivated by ALD Al_2O_3, the spectrum of an exposed SWNT section features a G peak, which is shifted and significantly lower in intensity. These observations indicate that carbon atoms are indeed present at the assumed position of the SWNT but are not part of the sidewall of a defect-free SWNT. Defects in the sidewalls of the SWNT channel, induced during the experiment, may explain the observed gradual decrease of the on-state current within the first 7 minutes after humidity exposure (Fig. 6.4(a)).

Summary

Above 70 % r.h. the CNFET NO_2 sensors degrade to complete loss. The presented $I_d V_g$ characteristic degrades within minutes upon high level humidity exposure before NO_2 gas is added. The characteristic becomes distorted with dips in the n-type current branch until it finally shows no current anymore. From then on, the $I_d V_g$ characteristic shows a linear current-voltage dependence with negative I_d for negative V_g and positive I_d for positive V_g. This observation suggests that adsorbed H_2O molecules start to form a conductive film between the exposed SWNT channel and the Si substrate, which serves as the backgate. We speculate that an electrochemical process taking place at the SWNT channel is responsible for the

structural damages of the CNFET sensor. After the experiment, the $I_d V_g$ charac-
teristic can not be recovered anymore, despite heat treatment for 1 h at 110 °C
.

6.2.4 Summary and Conclusion

We have first exposed CNFET NO_2 sensors to 10, 20, 30, 40, 50 and 60 % r.h. with
synthetic air as carrier gas without the addition of NO_2. Similar to results reported
by Kim *et al.* [60], gate hysteresis width in our devices increases with increasing
humidity level for continuous V_g sweeps. The humidity induced increase of gate
hysteresis can be suppressed to a large extent by using pulsed V_g, especially the
p+- mode ($t_{high} = 0.5$ ms) shows good hysteresis reduction performance in humid
conditions. The observation of positive, negative and no shifts of the $I_d V_g$ cha-
racteristics upon humidity exposure and a theoretical study [150] suggest that
the interaction between H_2O molecules and the SWNT channel are not based on
charge transfer but more of indirect nature via the formation of charge traps near
the SWNT channel. However, this issue needs further clarification.

For a moderate humidity level of 40 % r.h. the NO_2 detection was successfully
tested. The p+- pulsed V_g mode ($t_{high} = 0.5$ ms) renders the $I_d V_g$ characteristics es-
sentially hysteresis-free and NO_2 concentration dependent shifts are visible. The
NO_2 detection behavior in 40 % r.h. is similar compared to dry condition with
comparable LOD and sensitivity ranges.

Exposure to 70 % r.h. reveals that NO_2 detection with our CNFET sensors is not
possible in high humidity conditions (> 60 % r.h.). Within minutes after exposure
to high humidity the $I_d V_g$ characteristics degrade completely and NO_2 induced
shifts of V_{th} can not be observed anymore. From then on I_d is linearly dependent
on the amplitude and polarity of V_g, which suggests that an adsorbed water film
electrically shortcuts the exposed SWNT channel and the gate electrode. Inspec-
tion of the CNFETs by SEM after the experiment shows that the devices suffer
structural damage: the ALD Al_2O_3 is attacked along the SWNT, the metal contacts
feature dents where the SWNT reaches the metal and the area near the SWNT is
laced with particle-like debris. It is speculated that in the presence of adsorbed
water and potential differences of several volts between the SWNT and the gate
electrode leads to an electrochemical reaction at the SWNT channel, causing the
device degradation.

These results have some implications on the operation our CNFET NO_2 sensors.
NO_2 detection at constant moderate humidity levels seems possible with perfor-
mance comparable to dry conditions. However, in an environment with changing
humidity level, humidity induced shifts of the $I_d V_g$ characteristic are likely to in-
terfere with NO_2 induced shifts of V_{th}. At high humidity levels the operation

Synthetic Air

NO_2 Detection

High Humidity Level

Implications

of the CNFET NO_2 sensors does not seem possible, unless the operation mode and/or the device structure and the used materials are optimized. To avoid the high electrical potentials at the gate completely, the CNFET sensor could be operated as ChemiResistors: monitoring I_d with constant bias V_{sd} and $V_g = 0$ V. This would however require control over the position of V_{th}, in order to make the positive NO_2 induced shifts observable at $V_g = 0$ V. A much thinner SiO_2 gate oxide or its replacement with a thin layer of a high-k dielectric could help to reduce the required V_g to operate the sensor as a FET. The replacement or coating of the ALD Al_2O_3 used as passivation layer by a highly hydrophobic material could also improve the situation, as the adsorption of H_2O molecules near the SWNT channel may be still low, even at high humidity levels. Another possibility could be heating of the CNFET sensor above 100 °C , as is the case with most metal oxide gas sensors. However, heating inevitably goes hand in hand with a substantial increase in sensor power consumption, which would cancel the main advantage of CNFET gas sensors compared to conventional gas sensing technologies.

6.3 Influence of above ambient temperature

Motivation

In most CNFET sensors the CNT channels are in contact with oxide layers, in which charges can get trapped at elevated gate voltages V_g [31, 39, 59]. As we have previously seen, trapped charges can lead to gate hysteresis in the $I_d V_g$ characteristics, which hampers reliable operation of CNFET sensors, especially for those which rely on V_{th} as sensor output, as explained in chapter 5. So far, most CNFET sensors were characterized at room temperature. However, operation at elevated temperatures might be necessary for sensitivity/selectivity tuning or thermal analyte desorption for chemical sensors or any other kind of CNFET sensor operated in hot environments. Assuming a thermally activated charge trapping mechanism [39], gate hysteresis should increase considerably at above ambient temperature. It therefore needs to be clarified whether pulsed V_g methods are still able to reduce hysteresis above ambient temperature with reasonable V_g pulse durations. In this section, we investigate the charge trapping behavior in CNFETs above ambient temperature (300 to 390 K) and check the hysteresis reduction performances for the p++ and p+- V_g pulse modes.

Thermally Activated Charge Trapping Content

Experiment

The performance of the pulsed V_g modes is characterized at steady state T = 300, 330, 360, and 390 K. The gate hysteresis is defined as the difference between

the forward threshold voltage (V_{th}) and backward V_{th}, which are extracted from $I_d V_g$ characteristics according to section 3.4. Within the investigated temperature range, uncontrolled adsorption onto an exposed SWNT channel in a CNFET or desorption of gaseous species (e.g. water) has to be expected. For this reason, the following experiments are performed with fully passivated CNFETs, which had been shown to be essentially insusceptible to fluctuations in their gaseous environment (see section 4.2.1).

Results

In Fig. 6.5(a) gate characteristics of a CNFET are shown recorded with the pulsed p++ mode (t_{high} = 50 ms) at four different temperatures T = 300, 330, 360 and 390 K. With increasing temperature the gate hysteresis width in the $I_d V_g$ characteristics is seen to qualitatively increase. In Fig. 6.5(b) the $I_d V_g$ characteristics of the same CNFET are shown measured with the p+- mode (t_{high} = 50 ms). In contrast to the p++ mode, no gate hysteresis is observable in dependence of temperature. Fig. 6.5(c) summarizes the results presented in Fig. 6.5(a) and (b), showing the extracted gate hysteresis widths for pulse times t_{high} = 0.5, 5 and 50 ms at the four studied temperatures. The graphs display the average gate hysteresis of 45 consecutive sweeps (error bars = +/- standard deviation (σ)) for the p++ (filled markers) and p+- (unfilled markers) mode. Three main observations can be made. First, gate hysteresis is increasing with increasing temperature for the p++ mode, an effect that is more pronounced for long pulse durations t_{high}. Second, there is no systematic dependence of the gate hysteresis on temperature observable for the p+- mode, in dependence of t_{high}. Third, the averaged gate hysteresis values for the p+- mode are close to 0 V and consistently smaller compared to the values extracted for the p++ V_g strategy.

One explanation for gate hysteresis in CNFETs is trapping/detrapping based on Fowler-Nordheim or other injection mechanisms of charges from the SWNT into oxide layers or into layers of adsorbed molecules close to the CNT channel [31, 39, 59, 60]. If the injection mechanism is thermally activated, charge trapping should be enhanced with temperature, resulting in increased gate hysteresis above ambient temperature. To check this hypothesis, a simple charge trapping experiment, based on the stress and sense principle [156] is performed. The applied V_g waveform is shown in Fig. 6.6: 20 consecutive positive charge pulses (CPs) (+7.5 V amplitude, t_c = 5 and 125 ms) are applied to the back gate of the same CNFET. Each CP is immediately followed by a p+- probe sweep (PS) of small amplitude (+/-2 V, t_{high} = 0.5 ms, t_{total} = 0.12 s) to probe V_{th}. The amplitude of the PS is chosen as small as possible to minimize its influence on the charge trap filling level near the CNT while still allowing for unambiguous extraction of

Gate Hysteresis & Temperature

Stress and Sense
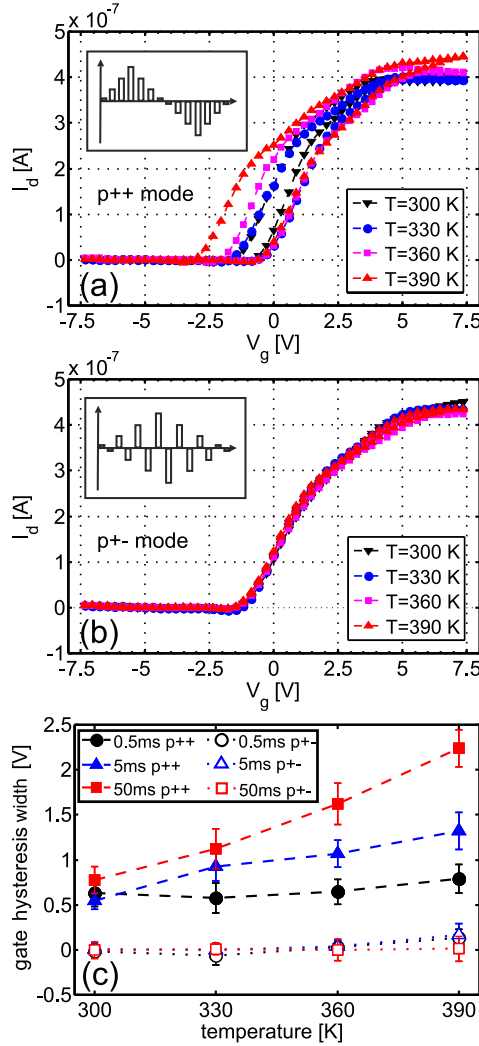
Figure 6.5: CNFET gate characteristics recorded with the p++ (a) and the p+- (b) V_g mode (t_{high} = 50 ms) at T= 300, 330, 360 and 390 K. V_{sd} = 30 mV. (c) Average (n = 45) gate hysteresis values extracted for the p++ (a) and the p+- (b) V_g mode. (Error bars = +/-standard deviation (σ)). For the p++ mode, gate hysteresis increases with temperature and pulse duration t_{high}. For the p+- mode no systematic dependence of the gate hysteresis on temperature and t_{high} is observable. Adapted from [149]. Copyright American Institute of Physics 2010.
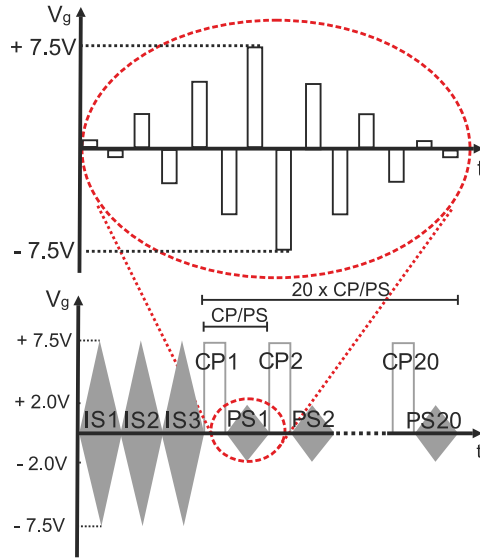
Figure 6.6: Schematic of the applied V_g waveform during the stress and sense experiment. The V_g waveform consists of initialization sweeps (ISs), charge pulses (CPs) and probe sweeps (PSs).

V_{th}. This experiment is repeated ten times at 300, 330, 360, and 390 K, and also for negative CPs (-7.5 V amplitude, t_c = 5 and 125 ms). At the very beginning of the experiment three initialization sweeps (ISs) are performed to electrically initialize the CNFETs, as explained in section 5.3.

The average of the extracted V_{th} upon positive and negative CPs (t_c = 125 ms) for the four investigated temperatures is shown in Fig. 6.7(a). From the measurement data at each temperature it seems that the probed V_{th} evolves exponentially with respect to the number of consecutive CPs. An exponential fit of the form (α-V_{th0}) (1-exp(-t/β)+V_{th0} with the parameters α, β and V_{th0} (initial V_{th}) was performed on the ensemble of ten repetitions (see the dashed lines in Fig. 6.7(a)). Qualitatively, α represents the saturation level of V_{th} and β the rate constant, showing how fast the shifts of V_{th} are evolving at each temperature. With increasing temperature (α-V_{th0}) (normalized saturation level) is increasing, as shown in Fig. 6.7(b) for two CP durations (t_c = 5 and 125 ms). The values of the rate parameter β are shown in Fig. 6.7(c) for CPs of t_c = 5 and 125 ms. From 300 to 330 K β increases, except at the value for t_c = 125 ms and +7.5 V. For T = 330 K for both negative and positive CPs and t_c = 5 and 125 ms β decreases.
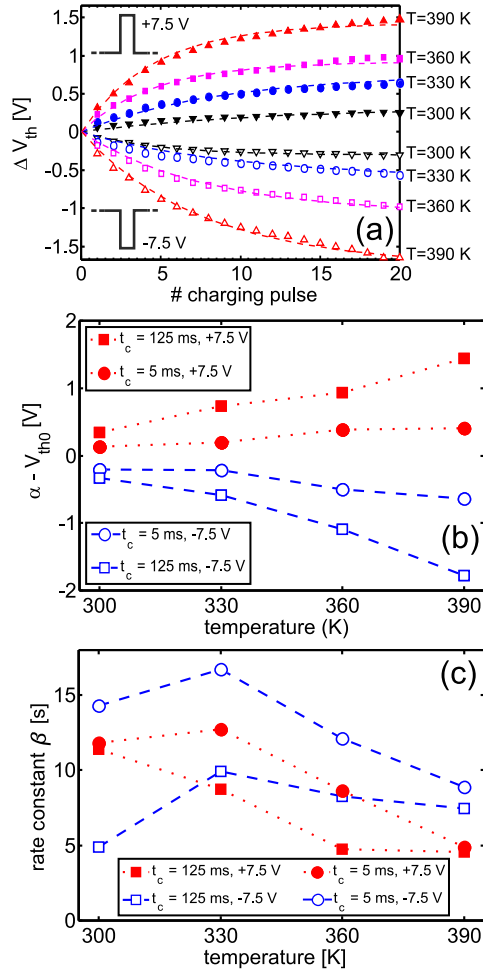
Figure 6.7: (a) Evolution of V_{th} upon 20 positive and negative CPs ($t_c = 125$ ms) at T = 300, 330, 360, and 390 K. With increasing temperature V_{th} reaches larger saturation levels. The dashed lines display exponential fits to the measurement data (see main text). Each PS consists of 200 pulses with $t_{high} = 0.5$ ms. (b) Values of the parameter (α-V_{th0}) (normalized saturation level) at 300, 330, 360, and 390 K. With increasing temperature, (α -V_{th0}) is increasing. (c) Values of the parameter β (rate constant) at 300, 330, 360, and 390 K. With increasing temperature β is roughly decreasing. See main text for description of the fitting procedure. Adapted from [149]. Copyright American Institute of Physics 2010.

6.3.1 Discussion

The temperature dependence of both the normalized saturation level (α-V_{th0}) and the rate constant β support the hypothesis of increased charge trapping with increasing temperature in the studied range.

The two parameters α and β characterize the evolution of V_{th} as sampled roughly every 1 s during the PSs after a CP. As such, they can help to understand the charge trapping behavior within the investigated temperature range. Note however, that they should not be confused with analog parameters describing the microdynamics of the charge trap filling levels. To capture the microdynamic parameters, in an ideal experiment one would apply a unit V_g step (Heaviside function) of given amplitude to the gate electrode and measure V_{th} shifts continuously in time. We would expect that the V_{th} shifts would have an exponentially saturating behavior with parameters α_0 and β_0, describing the microdynamics. However in practice, to extract V_{th}, we have to perform full V_g PSs. They consist of many ambipolar V_g pulses, which inevitably influence the charge trap filling level and are the cause for the different values of the saturation level α for $t_c = 5$ ms versus tc=125 ms. The extracted parameters α and β are on one side determined by the microdynamics (α_0 and β_0) but on the other side also by the applied V_g waveform.

We now sketch a qualitative connection between the stress and sense experiment (Fig. 6.7) and the two pulsed modes and their hysteresis behavior. The V_{th} shifts upon V_g pulses shown in Fig. 6.7(a) are consistent with changing the charge trap filling level near the SWNT channel. Filled charge traps create an additional potential, partially screening V_g, therefore resulting in gate hysteresis. A p++ sweep consists of two half periods of consecutive V_g pulses of the same polarity, which cause charge trapping and charge accumulation in the trap states near the CNT channel. Filled charge traps create an additional potential, partially screening V_g, therefore resulting in hysteresis in the gate characteristic. In a p++ sweep, considering the time between two identical V_g pulses, many pulses of the same polarity are applied to the gate. Due to the pulses of same polarity, charges are trapped and V_{th} is shifted, which leads to hysteresis in the gate characteristic. With longer pulse duration t_{high}, the total time during which V_g pulses of the same polarity are applied to the gate increases, causing more charge trapping and therefore larger gate hysteresis. Estrada *et al.* [157] suggest that the relaxation time of trapped charges decreases at higher temperature. Their measurement technique is similar to our p++ mode but with t_{low} varied instead of t_{high}. Their findings together with ours indicate that both charge trapping and detrapping dynamics increase with temperature. Due to the enhanced charge trapping with increasing temperature, the p++ mode would require challengingly short V_g pulses for hysteresis reduction above room temperature. This would require high-frequency

Impact of PSs

p++ vs. p+-

chip layout designs and wide bandwidth low noise amplification for the readout electronics.

In contrast, in the p+- mode each positive pulse is followed by a negative pulse, which means that charges trapped during the positive pulse are discharged again during the immediately following negative pulse. Considering the time between two identical V_g pulses within a p+- sweep, much less charges are built up, compared to the p++ mode due to the permanently alternating polarity of the pulses. Thus, essentially no hysteresis is observable with the p+- mode in dependence of pulse duration t_{high}, even above ambient temperature when charge trapping is enhanced.

6.3.2 Summary and conclusion

T Enhanced Charge Trapping

In summary, we have seen that charge trapping in CNFETs is enhanced with increasing temperature, which leads to increasing gate hysteresis in $I_d V_g$ characteristics. While the pulsed p++ mode is not capable of reducing the temperature induced gate hysteresis, $I_d V_g$ characteristics recorded with the p+- mode exhibit almost no gate hysteresis in dependence of the pulse width t_{high}. Therefore, the p+- instead of the p++ V_g sweep mode should be used to operate CNFET sensors, especially above ambient temperature.

Further Effects of T

After this experiment with a fully passivated CNFET it seems obvious that also NO_2 detection with a CNFET NO_2 sensor should be tested above ambient temperature. However, before we could do this investigation an important puzzle piece is missing. Varying temperature during NO_2 detection, we would expect to mostly influence the sensors' response and recovery time, as analyte adsorption and desorption depend on the gas kinetics. So far we have measured the sensor response only in steady state conditions at the very end of relatively long NO_2 levels without having any time-dependent information about NO_2 adsorption/desorption. In order to see effects related to gas kinetics we need to be able to operate the CNFET NO_2 sensors in a mode, which allows the extraction of a time transient sensor signal.

7 Defining a sensor output signal

7.1 Introduction

In the previous chapters the NO_2 detection behavior of the CNFET sensors was investigated only in steady state conditions. Namely, $I_d V_g$ characteristics were recorded in synthetic air and at the very end of every NO_2 concentration step. V_{th} values upon NO_2 exposure were compared to V_{th} values in synthetic air and the calculated difference in V_{th} was then interpreted as the sensor response to a particular NO_2 concentration level. This operation mode is suitable to characterize the basic sensing behavior. However, in real-life applications the situation might be different compared to the experiments in the lab, as the expected NO_2 concentration profile is a-priori unknown. As such, the sensors need to be operated in a mode, which allows continuous extraction of a sensor signal at a given sampling rate in order to monitor the NO_2 concentration over time.

A widely used mode to operate CNFET sensors in a continuous way to obtain a time transient sensor signal is the ChemiResitor mode, as introduced in section 2.3.3. While a constant voltage bias is applied to the source and drain electrodes, I_d is continuously monitored at $V_g = 0$ V. This operation mode only works for CNFET devices with negative V_{th}, or in other words with $I_d \neq 0$ at $V_g = 0$ V. Otherwise no change in I_d is observable upon positive NO_2 induced shifts of V_{th}. Attempts to monitor I_d at a constant $V_g \neq 0$ V fail due to the hysteretic behavior of CNFETs, as explained in chapter 5. At $V_g \neq 0$ V, charges are injected from the SWNT into nearby charge traps, creating an additional electrostatic potential, which after certain time is large enough to screen the applied V_g. As a result, I_d drifts over time toward 0 A and no NO_2 induced shifts of the $I_d V_g$ characteristic are observable.

With our CNFET sensors, which feature polar n-type $I_d V_g$ characteristics and positive V_{th} values, the classical ChemiResistor mode is therefore not applicable. The most obvious solution seems to be the consecutive recording and the extraction of a parameter from $I_d V_g$ characteristics to create a sensor output signal. This chapter addresses the issue of defining a suitable sensor output signal. We test a V_{th} based sensor signal and propose two alternative schemes to extract a sensor output from consecutively recorded $I_d V_g$ characteristics.
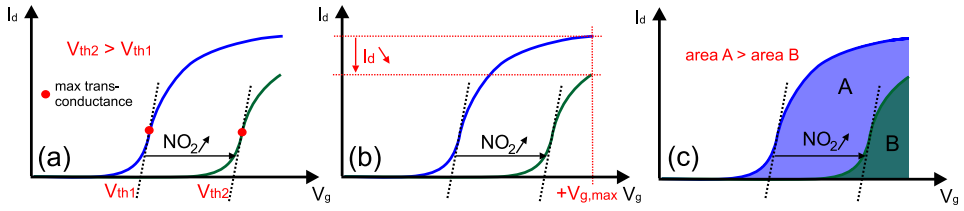
Figure 7.1: Working principle of employed readout schemes (ROSs) on $I_d V_g$ characteristics to create a sensor output signal. (a) ROS 1: extraction of V_{th}. (b) ROS 2: extraction of I_d at $V_g = V_{g,max}$. (c) ROS 3: calculation of the area enclosed by the n-type current branch and the x-axis.

7.2 Experimental

In this chapter three different readout schemes (ROSs), shown in Fig. 7.1(a)-(c), are tested to define a sensor output signal. ROS 1 is based on extracting V_{th} values from $I_d V_g$ characteristics, according to the strategy, which is described in section 3.4. In ROS 2 I_d is extracted from $I_d V_g$ characteristics at $V_g = V_{g,max} = 7.5$ V and ROS 3 is based on the calculation of the area enclosed by the n-type current branch and the x-axis. The sensor output signals are derived by employing the ROSs on $I_d V_g$ characteristics, consecutively recorded with the pulsed p+- mode ($t_{high} = 0.5$ ms) and 1 min sampling rate. Before each recording of an $I_d V_g$ characteristic, two p+- V_g sweeps are performed to electrically initialize the CNFET sensor, as explained in section 5.3. The sampling rate of 1 min is close to the maximum sampling rate of the employed measurement setup (section 3.2.1), as the storing of the measured data and the initialization of the hardware takes considerably long time compared to the V_g sweep itself. The sensor output signals are low-pass filtered by a moving average filter of the form filtered_data(i) $= \frac{1}{span} \sum_{n=i-span+1}^{i} data(n)$ with different filtering spans ranging from 5 to 40 min. All measurements are performed at RT.

7.3 Readout scheme 1

Results

We first analyze V_{th} itself (ROS 1) as a sensor output signal. According to the NO_2 sensing mechanism of charge transfer between NO_2 and the SWNT channel, a V_{th} based sensor signal has a direct physical meaning, as it mirrors the NO_2 induced shift of the charge neutrality level (section 2.3.2). The applied NO_2 profile is shown in Fig. 7.2(a). In the phase of the first four hours the measurement cham-

ber is flushed with synthetic dry air, followed by four steps of NO$_2$ of 250, 500, 1000 and 2000 ppb and 90 min duration each. After NO$_2$ exposure, the chamber is again flushed with synthetic dry air for 5.5 hours. Fig. 7.2(b) shows the non-filtered V_{th} based sensor output signal. The vertical dashed lines indicate the NO$_2$ concentration steps. During the first 4 hours the signal shows a band of fluctuation of $\Delta V_{th} \approx \pm 1$ V. From 2 h on the mean of V_{th} is at about 4 V within the band of fluctuation until the first NO$_2$ concentration is added to the carrier gas. Upon the injection of 250 ppb NO$_2$, an increase of the local V_{th} mean of about 1 V can be estimated. The addition of 500 ppb of NO$_2$ at t = 5.5 h seems not to remarkably change the sensor signal. Upon injection of 1000 and 2000 ppb of NO$_2$ into the measurement chamber the extracted V_{th} values fluctuate over a range of several volts. After exposure to NO$_2$ and upon flushing with synthetic dry air the signal fluctuations decrease considerably compared to the period of exposure to high NO$_2$ concentration. The signal is slowly decreasing at an average rate of about 0.2 V / h, which results in $V_{th} \approx 5.5$ V at the end of the experiment.

Discussion

Upon addition of 250 ppb of NO$_2$, we see a positive shift of V_{th} of about 1 V, which is comparable or even smaller than the amplitude of the singal fluctuations. This results in a small signal-to-noise-ratio (SNR), which renders the monitoring of the exact NO$_2$ concentration hardly possible. Doubling the NO$_2$ concentration does not have a remarkable change of the ROS 1 sensor signal, which seems to be dominated by large signal fluctuations. NO$_2$ Sensing

In Fig. 7.2(b) we observe that upon the injection of 1000 and 2000 ppb of NO$_2$ the V_{th} based sensor signal starts to fluctuate within several volts, which does essentially not allow the extraction of any sensing information anymore. During the experiment at t = 7.5 h $V_{th} \approx 6.5$ V. Considering the limited V_g sweep range of $V_{g,max} = 7.5$ V, only a very small onset of the n-type current branch is still visible in the $I_d V_g$ characteristic at that time. The current onset contains not enough data points to reliably determine the highest transconductance, which is needed for the extraction of V_{th}. The applied extraction strategy becomes unreliable and returns meaningless values for V_{th}. Reviewing methods to determine V_{th} from standard MOSFETs reveals that there exist numerous extraction strategies [158]. But all of them need a certain number of data points in the onset of a current branch in order to perform correctly. In this very experiment the V_{th} based sensor output signal is in saturation upon exposure to 1000 and 2000 ppb of NO$_2$. Sensor Saturation
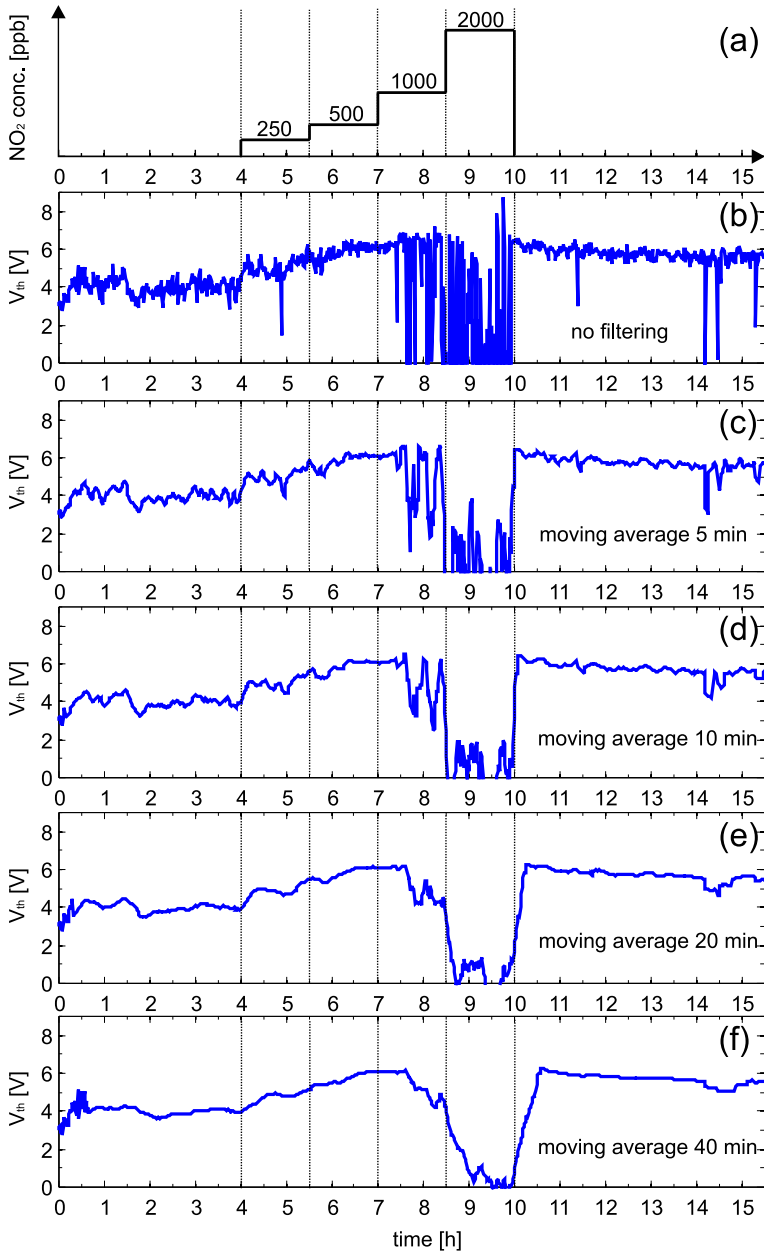
Figure 7.2: NO$_2$ concentration profile during the experiment (a). ROS 1: V_{th} based sensor output signal versus time, non-filtered (b); low-pass filtered with a span of 5 min (c), 10 min (d), 20 min (e) and 40 min (f).

7.3.1 Impact of filtering on readout scheme 1

In Fig. 7.2(b) we have seen the unfiltered ROS 1 sensor output signal, from which the exact NO_2 can not be extracted. We now want to check whether filtering of the sensor output signal can help to improve the situation. Intuitively it seems obvious that not low-pass but instead band-pass filtering is the optimum strategy to remove noise from a sensor signal since signal fluctuations of frequency below and above the expected stimulus bandwidth can essentially be removed. As the target application and thus the changing rate of the NO_2 concentration are not clearly specified in our case, the design of a dedicated band-pass filter is not possible. In addition, the sampling rate is rather low at 1 min, limited by the measurement setup. As such, we employ a low-pass moving average filter (section 7.2) to illustrate the effect of filtering on the sensor output.

Filtering
Strategy

Results

Fig. 7.2(c)-(f) show the low-pass filtered sensor output signals created by ROS 1. The larger the filtering span, the smaller the local band of V_{th} fluctuations and the better the NO_2 induced shifts of V_{th} become visible. Also from the filtered signal the detection of 1000 and 2000 ppb of NO_2 is not possible. For deeper analysis we have a look at the sensor output signal at the transition from synthetic air to 250 ppb of NO_2, shown in Fig. 7.3(a-e). During the last 2 h before the exposure to NO_2 the mean sensor signal seems to be stable without visible trend of drift. We take this period of time as calibration region to define a band of signal fluctuation with an upper and lower limit (dashed lines). As criteria for NO_2 detection, we chose the event of the sensor signal exceeding the determined upper limit of fluctuations. Vice versa if the sensor signal falls below the lower limit NO_2 desorption might be happening. According to the performed experiment, 250 ppb of NO_2 are injected into the chamber at t = 4 h. In the following, the time between the injection of NO_2 and the first detection event (when the sensor output signal exceeds the set upper limit of fluctuations), is defined as the sensor detection time. These criteria for the sensor output signal to indicate detection of NO_2 and the sensor response time, are suitable for this analysis. They should be reconsidered to fit a dedicated application. In the following, this procedure is also applied to the low-pass filtered sensor output signals (Fig. 7.3 (b-e)). Upon higher filter span the band of fluctuations in the calibration region (2 h < t < 4 h) becomes naturally smaller and the slope of the rising sensor output signal due to NO_2 (t > 4 h) becomes also smaller due to the increasing averaging effect. As a result, the detection time to 250 ppb of NO_2 according to above criteria, becomes longer for higher filter spans. A criterion, which might be used as an indication for the sensor signal's reliabi-

Detection
Time

Signal
Reliability

lity, is how many false negative detection events during the exposure of 250 ppb of NO_2 occur. In other words, how often after the first detection event of NO_2 does the sensor output signal fall again below the set detection limit. As visible from the red shaded areas in Fig. 7.3 the unfiltered and the weakly filtered (span = 5 min) sensor signals show false negative events due to signal fluctuations during the period of NO_2 exposure.

Discussion

For the V_{th} based sensor signal the selection of the appropriate filtering strategy is finally a trade-off between detection time and the sensor signal reliability. For the application of a NO_2 detector, mostly a short detection time is important. In this case, a rather low span would be preferable. On the other hand, if the detection time is not of high priority but the output signal's reliability with regards to false negative events is important a filter with large span might be the better choice. However, even the ROS 1 signal filtered with the highest filterspan of 40 min shows a band of signal fluctuations in the calibration region, which is comparable in amplitude to the NO_2 induced signal change. This observation suggests that also heavy filtering of the sensor signal might not allow the operation of our devices to monitor the exact NO_2 concentration over time. Instead, the operation as NO_2 detector seems more realistic if a sensor signal threshold value, indicating the presence of NO_2, can be defined, which is not exceeded by the signal fluctuations.

Regarding the observed tradeoff between detection time and signal reliability, the question of an optimum tradeoff is valid. Fig. 7.4 illustrates the impact of the filter span (1 to 40 min) on the detection time (left y-axis) and the number of false negative events (right y-axis) upon 250 ppb of NO_2. To achieve short detection times of 3 min, a filter span of 4 or 5 min should be selected, while for a high detector signal reliability filter spans $\geq$ 10 min are suitable to avoid false negative detection events. For this data set the minima for the detection time and the number of false negative events do not coincide at the same filter span. This analysis gives a first impression on how low-pass filtering may affect the V_{th} based output sensor signal. Note, that the results are not statistically significant since this analysis is based on one data set alone. However, a comparable experiment with a different NO_2 concentration profile revealed very similar sensor output signal behavior.

7.4 Investigating the nature of fluctuations in $I_d V_g$ characteristics

Motivation In Fig. 7.3 a band of fluctuation was defined in the calibration region (2 h $\leq$ t $\leq$ 4
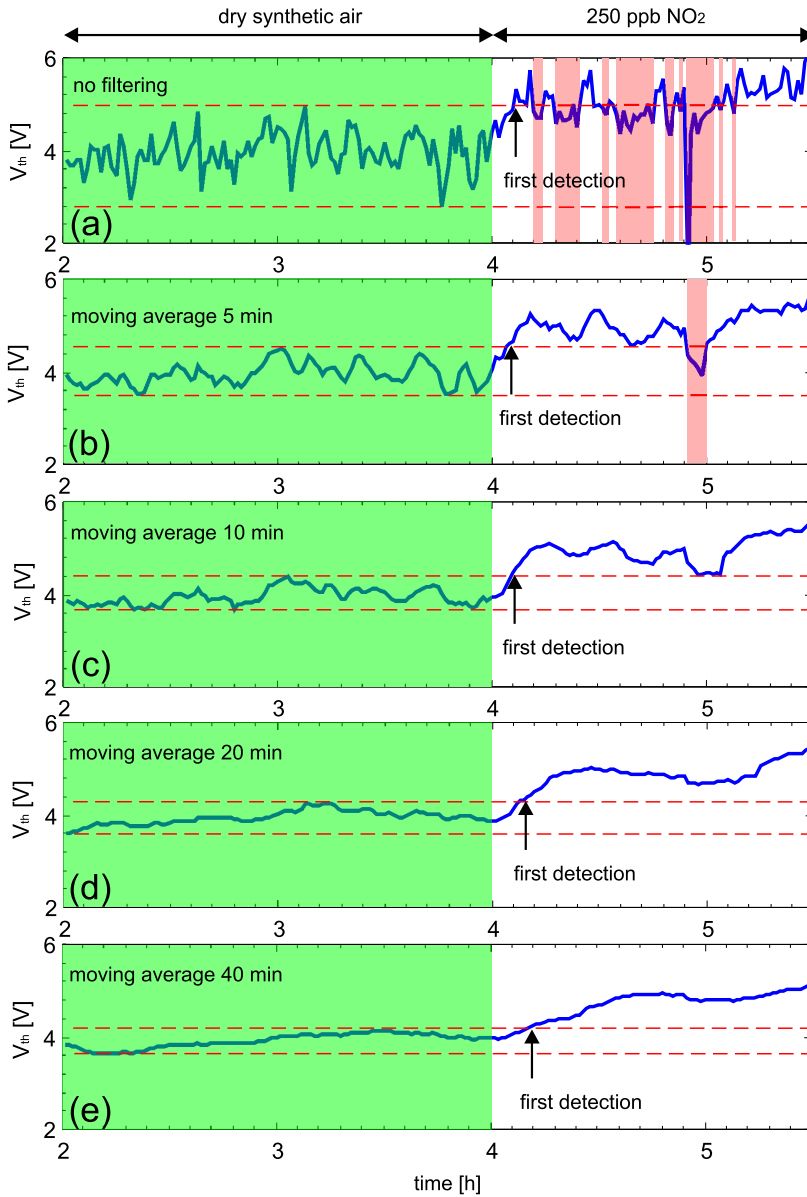
Figure 7.3: Extracted V_{th} values versus time (between t = 2 h and 5.5 h). non-filtered (a); low-pass filtered moving average with a span of 5 min (b), 10 min (c), 20 min (d) and 40 min (e).
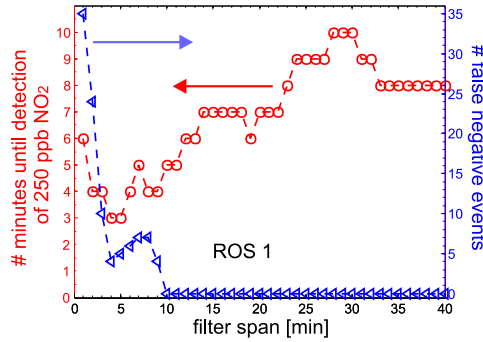
Figure 7.4: Filter span of a low-pass filter versus the detection time (left y-axis) and the number of false negative events (right axis) of the ROS 1 sensor output signal upon exposure to 250 ppb of NO_2.

h), when the mean of the V_{th} based sensor signal seemed to have reached essentially steady state. In the unfiltered signal the band of fluctuation is $\Delta V_{th} \approx 2$ V. Considering the initial value of $V_{th} \approx + 2$ V of the CNFET NO_2 sensors and the limited sweeping range of up to $+V_{g,max} = +7.5$ V, the maximum range of detectable NO_2 induced shifts of V_{th} is about 4 to 5 Volts. The observed fluctuations are thus significant and severely limit the signal-to-noise ratio (SNR). It seems thus necessary to investigate the nature of the observed fluctuations of V_{th} in more detail and especially look for any substructure or signal hidden in this noise. In other words, one has to make sure that the observed fluctuations are indeed noise.

As seen from the study by Helbling *et al.* [63] and in the NO_2 sealing test (section 4.2.1) fully passivated CNFETs are well protected from the adsorption of gaseous species from the ambient for at least hundreds of days. As such, they are a good test bench and structurally very close to the CNFET NO_2 sensors, to investigate the nature of V_{th} fluctuations observed during NO_2 detection.

Limited SNR

Results

ROS 1

In the following, fully passivated CNFETs (40 nm of ALD Al_2O_3) are characterized over 72 h with the same measurement conditions as the CNFET NO_2 sensors: p+- V_g sweeps with 1 min sampling rate. The signal created from ROS 1 is shown in Fig. 7.5. Discarding the first 500 minutes (gray shaded area) to exclude any possible initial signal drift from the analysis, a band of signal fluctuations $\Delta V_{th} \approx$ 1.1 V from a measurement period of almost 64 h is extracted. For a measurement duration of 2 h, in analogy to the calibration region of the CNFET NO_2 sensors
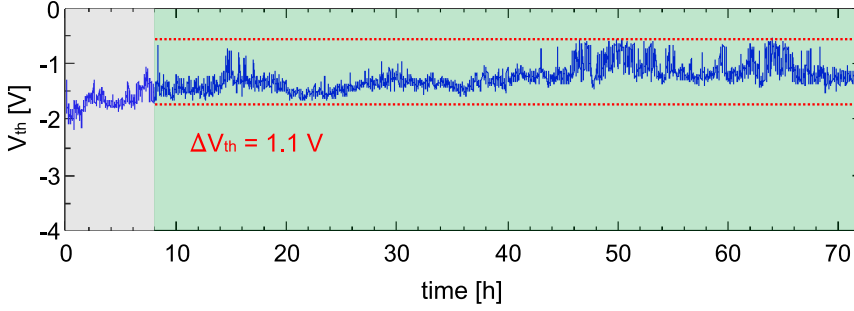
Figure 7.5: Extracted V_{th} values from $I_d V_g$ characteristics (ROS 1) of a fully passivated CN-FET device recorded at a sampling rate of 1 min over 72 h.
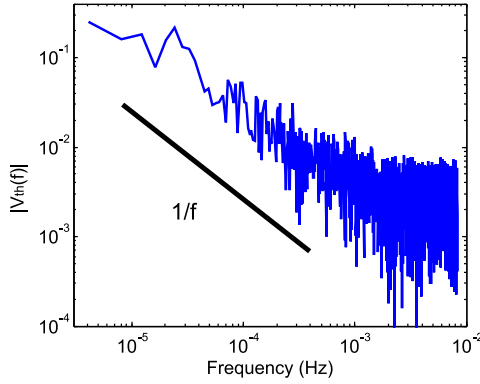
Figure 7.6: Frequency spectrum of the ROS 1 signal shown in Fig. 7.5 recorded with a fully passivated CNFET. Sampling rate 1 min, 3820 samples.

(Fig. 7.3), for the fully passived CNFET $\Delta V_{th} \approx 0.5$ V, which is by a factor of about 4 smaller then the observed fluctuations in the CNFET NO_2 sensors.

Fig. 7.6 shows the frequency spectrum of the ROS 1 signal shown in Fig. 7.5, which follows a $1/f$ trend. Frequency Spectrum

We now want to further investigate the nature of the observed V_{th} fluctuations. Fig. 7.7(a) shows the mean, the maximum and the minimum $I_d V_g$ characteristics from the entire experiment, except the first 500 min, which results in an ensemble of 3820 $I_d V_g$ characteristics. The shaded area indicates the distribution of the $I_d V_g$ characteristics, which seems to be mostly even around the mean $I_d V_g$ characteristic. The shape of the histograms of the I_d values at constant V_g (= -1, 0, 2 and 6 V), shown in Fig. 7.7(b) support this observation. All histograms are highly symmetric and bell-shaped (except the histogram at $V_g = -1$ V since $I_d \geq 0$ A). The
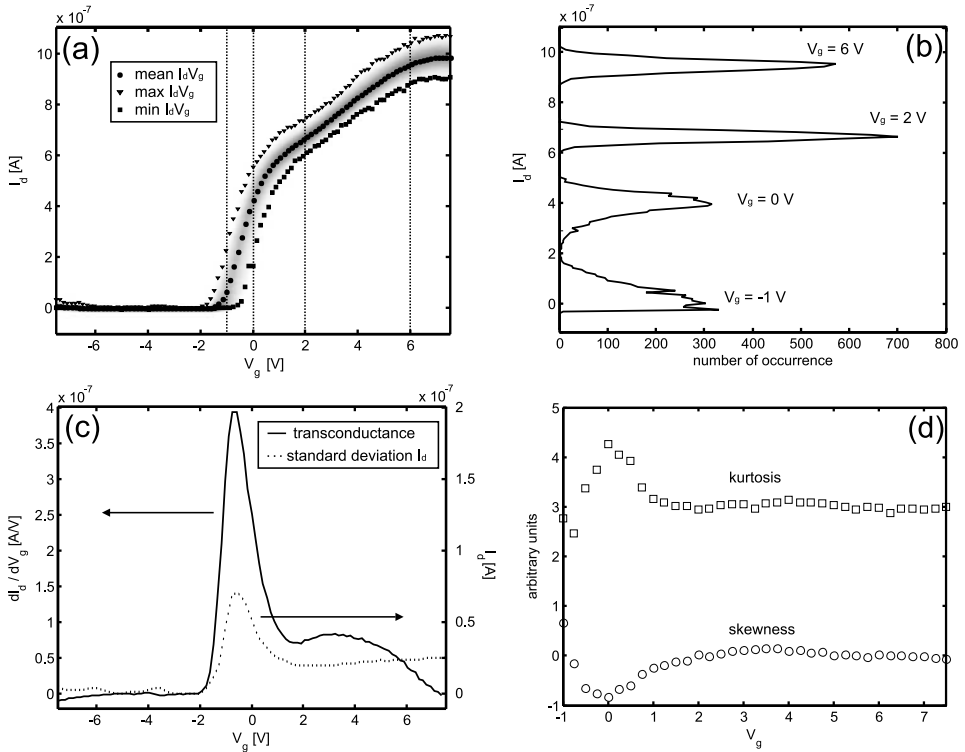
Figure 7.7: (a) Mean, minimum and maximum $I_d V_g$ characteristics (left axis) from an ensemble of 3820 $I_d V_g$ characteristics recorded with a fully passivated CNFET at 1 min sampling rate. The shaded area displays the distribution around the mean $I_d V_g$ characteristic. (b) Histograms of I_d at V_g = -1, 0, 2 and 6 V. (c) First derivative of the mean $I_d V_g$ characteristic and standard deviation (σ) of I_d versus V_g. (d) Values of skewness and kurtosis of I_d versus V_g.

histograms for V_g = -1, and 0 V are clearly wider with a standard deviation (σ) about twice as large as of the histograms for I_d at V_g = 2 and 6 V. In other words, at these V_g values the fluctuations of I_d are considerably larger than for larger V_g. In Fig. 7.5(c) also the derivative of the mean $I_d V_g$ characteristic is plotted together with $\sigma(I_d)$ versus V_g. From this plot it seems clear that the amplitude of the I_d fluctuations is the highest in the region of the highest transconductance. In Fig. 7.5(d) the skewness and the kurtosis [159] of the ensemble of I_d values versus V_g is shown. While the skewness is close to 0 the kurtosis is close to 3 for all V_g values.

Discussion

The observed difference in signal fluctuations of fully and non-passivated CN-FETs is in good agreement with findings of Helbling *et al.* [19, 63]. They found the amplitude of 1/f noise (2 Hz $\leq$ f $\leq$ 1.5 kHz) in fully ALD Al_2O_3 passivated CNFETs to be smaller than in as-prepared, non-passivated CNFETs by a factor of about 4. Due to the Al_2O_3 passivation layer the surrounding of the SWNT channel is chemically more quiet, which is believed to lead to less charge traps near the SWNT compared to the CNFET NO_2 sensor [60] and therewith to reduced noise amplitudes.

The bell-like shapes of the histograms and the values of skewness and kurtosis suggest that the fluctuations observed in $I_d V_g$ characteristics are mostly random. Skewness is a measure, which is used to indicate the symmetry of a distribution and kurtosis gives an information about how peaked a distribution is relative to a normal distribution. For a perfect normally distributed ensemble of datapoints skewness = 0 and kurtosis = 3, which is very close to our findings. The slightly larger values for kurtosis in the region of highest transconductance can be explained by the heavy tails of the respective histograms.

Noise following a 1/f law is known as Flicker noise and is believed to be caused by fluctuating charge traps [160]. 1/f noise in CNFETs [161–168] has been described by different models for the diffusive (adopted from MOSFET device physics, L > l_e) [169] and ballistic (L < l_e) transport regimes [143]. For diffusive transport randomly trapped and detrapped charges lead to carrier number fluctuations in the channel. In the ballistic regime, fluctuating states of charge traps affect the I_d via SB modulation (width and height) and the electrostatic potential along the channel. Lin *et al.* [170] compared the noise amplitude of suspended and non-suspended CNFETs, fabricated from the same long SWNT, and found it to be about 10 times lower. These findings suggest that charge traps in/on the gate oxide are to a great extent responsible for 1/f noise in CNFETs. The fluctuations in our devices might be also explained by fluctuating charge traps near the SWNT channel. They cause a fluctuating electrostatic potential, which acts in addition to the applied V_g and becomes visible in the form of V_{th} fluctuations [171, 172] in $I_d V_g$ characteristics. The dependence of I_d fluctuations on V_g was already reported by others [19, 104, 173]. This observation is in disagreement with Hooge's [174] empirical mobility fluctuation theory, according to which the current noise amplitude should only depend on carrier concentration, and thus I_d and not on device transconductance.

The current fabrication process (section 3.1) does not include any measures to reduce the density of charge traps near the SWNT channels. In standard MOSFETs typically forming gas (mixture of H_2 and N_2) annealing steps at around 400 °C

are performed to passivate charge traps in Si/SiO_2 interfaces. If high-k dielectric layers are involved, higher temperatures in the order of 600 °C are required to saturate interface traps [175]. To avoid such high temperatures, which are not compatible with standard CMOS processes, annealing strategies employing high pressure conditions and additional chemicals (e.g. deuterium) are applied [176, 177]. It might be that annealing strategies can help to reduce the charge trap density in our CNFETs and therewith also reduce the observed fluctuations in the I_dV_g characteristics. However, the effectiveness of annealing has to be verified for CNFET NO_2 sensors. After opening the window in to the ALD Al_2O_3 layer to expose the SWNT channel, molecules from the ambient can adsorb onto/near the SWNT and possibly reinstall charge traps [60].

External Influences | Over the entire duration of 72 h of the experiment T and the r.h. level were almost constant with regards to real sensors applications, varying at RT $\pm$ 1.6 °C and r.h. = 30 % $\pm$ 2 %, respectively. With respect to these rather small variations of the two parameters no correlation of the observed V_{th} fluctuations were observable. The same experiment was also performed with CNFET devices from different fabrication runs to minimize influences from process variation and also measurements in a closed box fabricated from μ-metal permalloy to shield electromagnetic waves, lead to very similar results.

7.5 Readout scheme 2 and 3

Motivation | Previous analysis reveals that the fluctuations of I_d strongly depend on V_g, reaching a maximum in the region of the highest transconductance. This means that using V_{th} as sensor output signal might be not the best solution because V_{th} is extracted at maximum transconductance and thus in the region of maximum I_d fluctuation. Therefore, we are led to ask whether there is another sensor output signal, which might be less prone to the intrinsic fluctuations of I_dV_g characteristics.

ROS 2 | Similar to the ChemiResistor mode we can also extract I_d at the same $V_g \neq 0$ V from all recorded I_dV_g characteristics. As I_dV_g characteristics are positively shifted due to NO_2 adsorption, I_d extracted at positive V_g would decrease. For two reasons it seems favorable to extract I_d at $+V_{g,max} = 7.5$ V. First, as seen from Fig. 7.7(b) the fluctuations of I_d are considerably small in the saturation region compared to other regions of the I_dV_g characteristics. Second, extracting I_d at $V_g = 7.5$ V would also make large shifts of V_{th} observable and therewith maximize the range of detectable NO_2 concentrations. An issue with taking I_d at $V_g = V_{g,max}$ as sensor signal might be that upon large NO_2 induced shifts of V_{th}, the region of maximum transconductance is eventually shifted to $V_{g,max}$ and I_d would be subject to large fluctuations. This strategy to form a sensor output signal is called ROS 2, as intro-

duced in section 7.2.

Another idea for a sensor output signal, which takes into account many more data points from an I_dV_g characteristic, and hopefully reduces signal fluctuations, is based on calculating the area enclosed by the n-type current branch and the x-axis. Once the I_dV_g characteristic is positively shifted, the calculated area decreases due to the limited V_g sweeping range. This strategy is called ROS 3, as introduced in section 7.2.

Results

Since we acquire complete I_dV_g characteristics, we are able to illustrate and assess the performance of both these proposed schemes. Fig. 7.8(b) shows the unfiltered sensor output signal, created from I_d at V_g = 7.5 V. During the first 2.5 h in synthetic dry air the sensor signal seems to be in a transient state until it saturates at a current level of about 0.7 μA with a local band of signal fluctuation of $\Delta I_d \approx$ 0.2 μA. Step-like decreases of I_d, which timewise coincide with addition of NO_2, can be mostly observed for 250 and 1000 ppb, while upon addition of 500 ppb the sensor signal seems not to change significantly. When the step of 2000 ppb of NO_2 is reached, the I_d based sensor signal is already close to 0 A. Upon flushing with synthetic dry air, I_d increases with an average rate of about 0.1 μA / h. The filtered sensor signals, again using moving average filtering of increasing span (Fig. 7.8(c)-(f)), show naturally smaller local fluctuations of I_d compared to the non-filtered signal and more clear step-wise decreases of I_d upon change of the NO_2 concentration level. The traces of the sensor output signal based on the calculated area enclosed by the n-type current branch and the x-axis are throughout the entire experiment very similar to the sensor output signal based on I_d at V_g = $V_{g,max}$. They can be found in appendix B.

Discussion

The most remarkable difference between ROS 1-3 is their behavior with regards to sensor saturation. The signal traces in Fig. 7.8 still show a step-like change upon injection of 1000 ppb of NO_2. For 2000 ppb of NO_2 also ROS 2 and 3 seem to be almost in saturation. However, upon exposure to the highest NO_2 concentration they remain close to 0, which can unambiguously be interpreted as sensor saturation. This behavior is in contrast to the large fluctuation of the ROS 1 signal for 1000 and 2000 ppb of NO_2, which might be misinterpreted as NO_2 adsorption/desorption.

The same filtering procedure as for ROS 1 is applied to ROS 2 and 3. After defining bands of signal fluctuation, the sensor response time and the number of
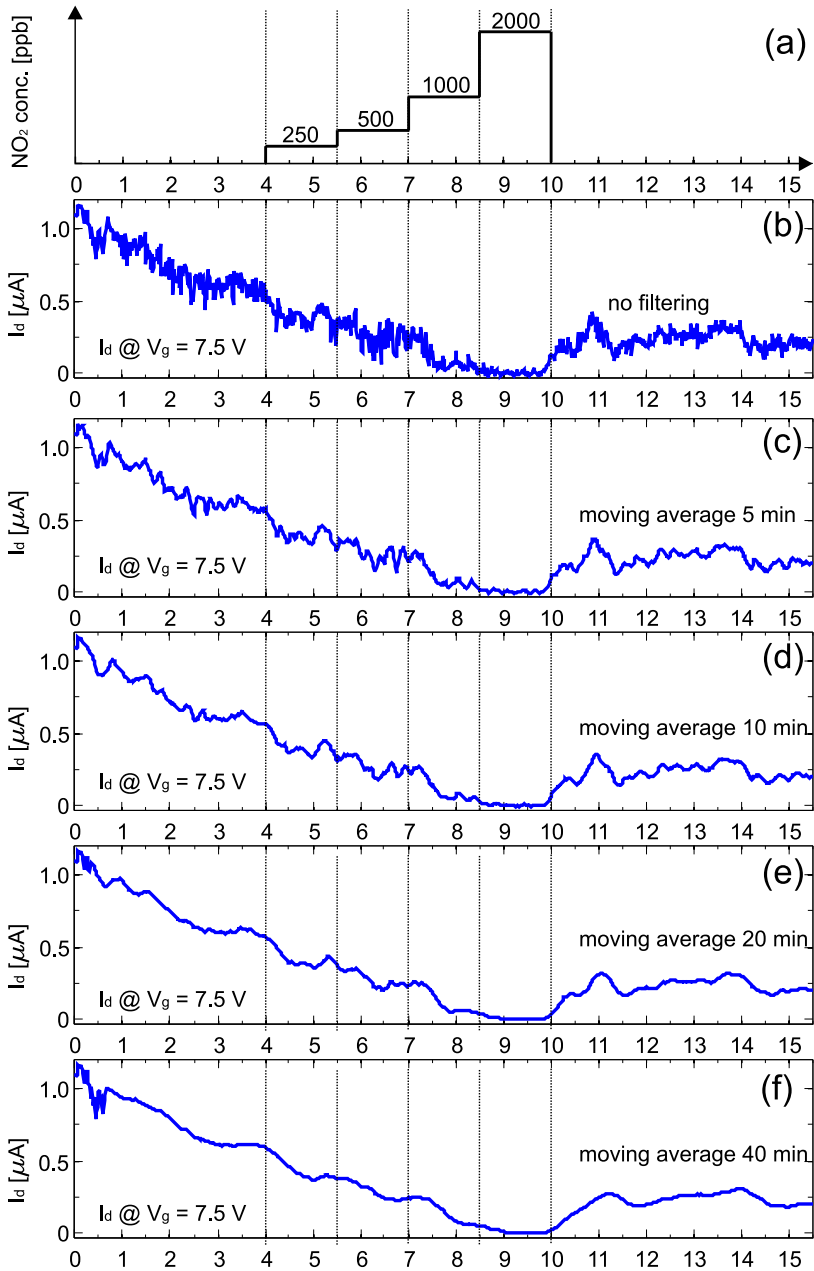
Figure 7.8: NO$_2$ concentration profile during the experiment (a). Extracted I_d values at V_g = const. = 7.5 V versus time, non-filtered (b); low-pass filtered with a span of 5 min (c), 10 min (d), 20 min (e) and 40 min (f).
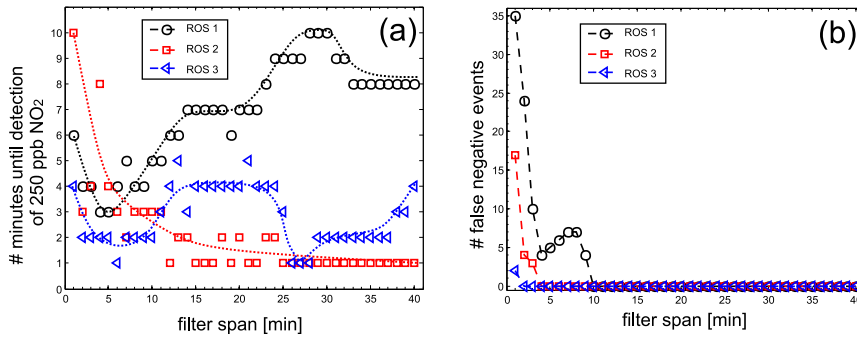
Figure 7.9: Filter span of a moving average low pass filter versus the sensor response time (a) and the number of false negative events (b) of all analyzed sensor output signals (ROS 1-3) upon exposure to 250 ppb of NO_2. The dashed lines are intended to guide the eye.

missed detection events upon exposure to 250 ppb NO_2 is determined and shown in Fig. 7.9(a) and (b), respectively. For reference also the values of ROS 1 are included (same data as in Fig. 7.4). For the available data ROS 2 and 3 seem to perform slightly better than ROS 1, as they both achieve the minimum achievable response time of 1 min (sampling rate). At the same time they don't show any false negative events for already small filter spans, which is in contrast to ROS 1. However, the results are not statistically significant as they are obtained from one data set alone. In order to do an accurate comparison, more data from many different sensors (with different initial V_{th}), upon many different NO_2 concentrations levels and repetitions are required.

7.6 Summary and conclusion

In this chapter we have addressed the issue of defining a time-dependent sensor signal. Due to the positive V_{th} value of the CNFET NO_2 sensors, the widely used ChemiResistor mode (monitoring I_d at $V_g = 0$ V) can not be applied. Instead three different readout schemes (ROSs), are proposed and tested on I_dV_g characteristics recorded with 1 min sampling rate. ROS 1 corresponds to extracted V_{th} values. During the experiment ROS 1 showed overall high fluctuations ($\Delta V_{th} \approx 2$ V). For the two highest NO_2 concentrations applied in the experiment, ROS 1 is in saturation and starts to fluctuate over several volts. At high NO_2 concentrations I_dV_g characteristics are heavily shifted and V_{th} can not be properly extracted anymore. Analysis of the low-pass filtered sensor signal revealed that the selection of

ROS 1

the filter span enables a tradeoff between short detection time and sensor signal reliability. The analysis suggests that the CNFET NO_2 sensors are more suitable to be operated as NO_2 detectors, rather than as NO_2 monitors due to the considerable signal fluctuations.

Fluctuations in $I_d V_g$ Characteristics

In the following the nature of intrinsic fluctuations of $I_d V_g$ characteristics in fully passivated CNFETs was investigated. The analysis of the data recorded over 72 h revealed that the $I_d V_g$ characteristics are subject to rigid shift-like random fluctuations along the V_g axis, with a 1/f frequency spectrum and highest I_d fluctuations in the region of the highest transconductance in the $I_d V_g$ characteristic.

ROS 2 & 3

Based on the findings about the nature of fluctuations in $I_d V_g$ characteristics, two alternative sensors output signals were proposed and tested. ROS 2 is based on extracting I_d at $V_g = V_{g,max}$ to avoid the region of highest I_d fluctuations in the $I_d V_g$ characteristics. ROS 3 is based on calculation of the area enclosed by the n-type current branch and the x-axis in order to average over all data points in the n-type current branch. Both alternative signals are intrinsically also very noisy and hardly revealed the NO_2 induced changes in the unfiltered state. Compared to ROS 1, they showed an enhanced measurement range, as they monotonically decrease with increasing NO_2 concentration and need less data points in the current onset of heavily shifted $I_d V_g$ characteristics. In terms of NO_2 detection time and sensor signal reliability ROS 2 and 3 performed slightly better compared to ROS 1 on the available data set. To allow a solid conclusion about the performance of the different sensor output signals more experimental data is required.

Outlook

In the end, all three tested sensor output signals are highly affected by the intrinsic fluctuations of the $I_d V_g$ characteristic. As such, the reduction of the density of charge traps near the SWNT channel, which are a potential source for 1/f noise in CNFETs, seems to be unavoidable. The large fluctuations in the sensor signals cause not only poor SNRs but also hinder the CNFET NO_2 sensors from being further characterized. As such, e.g. the extraction of NO_2 adsorption and desorption times and the comparison with data obtained from models describing molecular kinetics is currently not possible. Strategies to reduce the density of charge traps near the SWNT could be the incorporation of annealing steps in forming gas into the fabrication process, as they are applied in standard MOSFETs to saturate trap sites. Other solutions may involve applying high frequency V_g signals and using lock-in amplifiers to readout I_d. This solution however requests the adaption of the electrode layout and eventually of the entire measurement chain to become high frequency compatible.

8 Conclusion

8.1 Summary

In chapter 4 we have motivated the enhanced sensor structure and tested, whether it fulfills basic sensor requirements. As-prepared CNFETs were found by Helbling *et al.* to degrade within days and weeks, most probably due to oxidation of the metal contacts. Therefore, it seemed obvious that the metal contacts should be protected from environmental influences to improve device life time. From a sensing behavior point of view, Heller *et al.* have found during biosensing experiments with CNFETs sensing mechanisms at the SWNT metal interface to be less reproducible than mechanisms taking place at the SWNT bulk. Based on this information an enhanced sensor structure was proposed: CNFETs with individual SWNTs as gas sensitive channels and ALD Al_2O_3 passivated metal contacts. First, it was verified that 40 nm ALD Al_2O_3 can be used to protect fully passivated CNFETs from the influence of high concentrations of NO_2. I_dV_g characteristics of the tested devices remained unchanged upon exposure to 80 ppm of NO_2. NO_2 detection tests revealed a limit of detection (LOD) of 0.1 ppm of NO_2 (in steady state NO_2 adsorption conditions), which is well comparable the LOD of other CNFETs with pristine SWNT channels. The sensors responded with rigid shifts of the I_dV_g characteristic to NO_2 exposure, which is indeed the signature of charge transfer between the NO_2 molecules and the SWNT bulk while direct SB modulation as NO_2 sensing mechanism seemed to be inhibited. In a NO_2 desorption experiment it was shown that the proposed CNFET sensor structure can be reset: in ambient air within about 24 hours or accelerated by heat treatment for about 1 h at 110 °C . Finally, we demonstrated that the CNFET sensors with passivated metal contacts show superior long-term stability compared to as-prepared CNFETs. The I_dV_g characteristics of a CNFET NO_2 sensor recorded at day 0 and 310 (longest period measured) revealed that even after months the on-state current levels remained mostly unchanged.

Hysteresis in I_dV_g characteristics is a widely observed phenomenon in CNFETs, which is especially crucial for CNFET chemical sensors, as it hampers the unambiguous extraction of the intrinsic V_{th} value, often used as the sensor output signal. In chapter 5 we have systematically evaluated different pulsed V_g strategies for hysteresis reduction in synthetic dry air and for NO_2 sensing. During

<div style="text-align: right;">

Proposed
CNFET
Sensor
Structure

Pulsed V_g:
Hysteresis
Reduction

</div>

NO$_2$ detection substantial decrease of the gate hysteresis was observed at pulse times $t_{high} \leq 1$ ms (p++ mode). In addition an enhancement of the measurement range was found due to improved gate coupling compared to measurements with continuous V_g. A pulsed waveform, which is based on pulses of alternating polarity (p+- mode) achieved essentially hysteresis-free I_dV_g characteristics, almost independent from the employed pulse times (0.5 ms $\leq t_{high} \leq 50$ ms). Comparison of the measurement results with data obtained from an enhanced hysteresis model revealed good qualitative agreement. In contradiction to others studies, which proposed long V_g pulses to reset CNFET chemical sensors, the tested pulsed V_g strategies did not interfere with the NO$_2$ adsorption/desorption process. Further, it was shown that pulsed V_g waveforms can be used to erase the short-term electrical history of CNFETs. Before the measurement of an I_dV_g characteristic and the extraction of V_{th} as the sensor signal, pulsed V_g waveforms can electrically initialize a CNFET sensor and therewith improve the sensor's reliability and repeatability.

In chapter 6 we have presented the results of a study, which investigates first order influences of humidity and temperature (300 K $\leq$ T $\leq$ 390 K) on the CNFET I_dV_g characteristics. Upon addition of humidity (10 to 60 % r.h.) to synthetic air the CNFET NO$_2$ sensors showed increased gate hysteresis, which could be mostly reduced by employing pulsed V_g measurements. Especially the p+- mode featured good hysteresis reduction capabilities. As second effect, positive and negative shifts of V_{th} upon exposure to humidity were observed. The origin of this effect is not fully understood yet. It might be caused by the increased densitiy of fluctuating trapping/detrapping charges due to adsorbed H$_2$O molecules near the SWNT channel. The NO$_2$ detection behavior at constant moderate humidity (40 % r.h.) was found to be very similar to NO$_2$ sensing in dry conditions with comparable LOD and sensitivity ranges. In high humidity conditions (70 % r.h.) however, the CNFET NO$_2$ sensors could not be operated anymore. Molecularly adsorbed H$_2$O molecules seemed to shortcut the source, drain and gate electrodes. Possible solution to this issue might be the operation of the sensors in a ChemiResistor mode to avoid the high V_g potentials, coating of the sensor surface with a hydrophobic layer or constant heating of the sensor. Operation of CNFET above RT (300 K $\leq$ T $\leq$ 390 K) revealed enhanced charge trapping, which leads to increased gate hysteresis. While the pulsed p++ mode was not capable to reduce the temperature induced gate hysteresis, I_dV_g characteristics recorded with the p+- mode exhibit almost no gate hysteresis in dependence of the pulse width t_{high}.

In order to be able to monitor a NO$_2$ concentration profile, which is a-priori unknown, the CNFET NO$_2$ sensors have to be operated in a time continuous mode. In chapter 7 we have addressed the issue of defining a sensor output signal. A

Measurement Range Enhancement

Electrical Sensor Initialization

Influence of External Parameters

Sensor Output Signal

V_{th} based sensor output signal was found to suffer from large fluctuations ($\Delta V_{th} \approx$ 2 V), which severely limits the sensors' SNR, as only V_{th} shifts in the range of 4 to 5 V can be measured. Low-pass filtering of the V_{th} based sensor signal seemed to be a tradeoff between sensor response time and signal reliability. Further, the nature of intrinsic fluctuations in $I_d V_g$ characteristics was investigated in fully ALD Al_2O_3 passivated CNFETs. The fluctuations were found to be of the form of random rigid shifts along the V_g axis, showing a $1/f$ frequency spectrum. The highest amplitude of I_d fluctuations coincided with the region of maximum device transconductance. Based on this information two alternative sensor output signals were proposed and tested. Namely, extracting I_d at constant $V_g = V_{g,max}$ to avoid the region of high I_d fluctuations in $I_d V_g$ characteristics and the integration of all I_d values in the n-type current branch to average over more than just one datapoint. Comparison of the V_{th} based sensor signal with the two alternative strategies revealed that they performed slightly better in terms of detection time and signal reliability for the analyzed data set. However, in the end all three created sensors signals suffered from large signal fluctuations. As $1/f$ noise investigated in other studies at f < 1 Hz, the observed slow fluctuations (f < 0.5*1/60 Hz) in $I_d V_g$ characteristics are presumably also caused by charge trapping/detrapping events near the SWNT. Therefore, one possible solution to lower the large intrinsic fluctuations in $I_d V_g$ characteristics might be annealing steps during the sensor fabrication flow to saturate trap sites.

In Fig. 8.1 the overall sensor properties of the proposed CNFET NO$_2$ sensors are listed, which were collected during the experiments of this thesis. The presented listing is not a full sensor data sheet, as the characterization is still in its early stage.

Performance Overview

The proposed and characterized CNFET sensor structure features a typical power consumption of tens of nW during NO$_2$ sensing. This is about 6 orders of magnitude smaller than the power consumption of commercially available metal oxide based NO$_2$ sensors and comparable to other SWNT based sensors operated at RT. The sensor lifetime was shown to be at least 10 months, which was the longest period measured. This period of measurements is not long enough to allow a fair comparison with the specified lifetime of electrochemical cell based NO$_2$ sensors, which is in the range of 18 to 24 months. Compared to CNFETs without protecting passivation layer on the metal contacts, the observed long-term behavior is already a significant improvement. The application of pulsed V_g strategies for hysteresis reduction in CNFET chemical sensors was to our best knowledge not shown so far. Also the demonstrated electrical sensor initialization, and the reduction of the temperature and humidity induced gate hysteresis by pulsed V_g can be understood as an advancement of current state-of-the-art in CNFET (chemical)

Sensor metric	Value	Comment
Limit of detection (LOD)	100 ppb NO_2	in steady state NO_2 adsorption conditions
Sensing range	100 ppb – 18 ppm NO_2	considering multiple sensors
Sensitivity	0.25 – 50 V / ppm NO_2	V_{th} shifts, considering multiple sensors
Detection time	range of minutes	detection time as defined in chapter 7
Sensor recovery time	1 h @ 110°C, 24 h @ RT	-
Humidity range	0 – 40 % r.h.	-
Temperature range	27 - 117 °C	tested with fully Al_2O_3 passivated CNFETs only
Power consumption	tens of nW	during NO_2 sensing, without sensor recovery
Sensor lifetime	>10 months	longest period measured in ambient air

Figure 8.1: Table containing the key sensor metrics of the characterized CNFET NO_2 sensing technology.

sensor readout. The pulsed V_g strategies might be also applicable to other FET based sensor concepts, which suffer from gate hysteresis.

8.2 Outlook

Intrinsic Fluctuations

The most important issue to be addressed next in our opinion is the high level of intrinsic fluctuations, which was observed in this thesis (chapter 7). Noise does not only severely limit the SNR of the proposed CNFET NO_2 sensors, but it also hinders further in-depth characterization. For example to better understand the NO_2 adsorption/desorption characteristics, time constants from unfiltered sensor output signals should be extracted and also compared to results obtained from kinetic models. Considering the high I_d fluctuations, this is currently impossible. A potential solution to reduce the charge trap density near the SWNT channel and therewith also the observed signal fluctuations might be to include annealing strategies [175–177] in the fabrication flow to saturate trap sites in and between the oxide layers. However, this needs to be tested in NO_2 sensors with their exposed SWNT channel, onto which molecules from the ambient can adsorb and act as charge traps. Alternatively, applying high frequency signals to the gate and/or to the source electrode and using lock-in amplifiers to read out I_d at the locked frequency could help to obtain smoother sensor output signals [178]. This solution however may request considerable layout and read out redesign to make the entire measurement high frequency compatible.

Cross-sensitivity to Other Gases

In this thesis, NO_2 detection was only tested in dry and humid synthetic air but not in the presence of other gases, which may interfere with the positive NO_2 induced shifts of V_{th}. The selection and combinations of chemicals to which the

cross-sensitivity of the sensor should be tested, seems to be non-trivial. By defining the target application, maybe the ensemble of compounds to be tested can be minimized. Strategies, which can render a CNFET chemical sensor more specific toward certain chemicals were reviewed in section 2.3.3.

Even though first experiments on the effect of humidity and temperature on CNFET $I_d V_g$ characteristics were performed in this thesis, an in depth analysis with regards to these two external parameters is still needed. Especially, the humidity induced positive and negative shifts of V_{th} need to be clarified and the operation of the CNFET NO_2 sensors in high humidity conditions should be made possible. Here, optimization of the operation mode (avoid large V_g potential) and/or of the device structure and the used materials (employment of hydrophobic coatings) may improve the current situation.

Humidity & Temperature

Overall, in order to better understand and gain more confidence in the behavior of the CNFET NO_2 sensors with regards to the different aspects, which were investigated in this thesis, more experimental data is needed. During this thesis two major bottle necks were identified, which hindered us from collecting more measurement data. First, the current fabrication process is a prototyping process, which consists of very time consuming steps (e.g. AFM scanning and e-beam lithography) and results in only a low number of sensor devices (though the device yield is close to 100 %). Therefore, a batch fabriation process is needed to increases the number of devices available for charaterization and at the same time to reduce the fabrication time. Second, more measurement time to characterize the sensors in NO_2 is required since gas adsorption/desorption experiments typically take hours or even days.

More Experimental Data

The findings of this thesis do not only clarify open issues related with CNFET sensors, but they also rise new questions, as they advance in so far uncharted territory. Although some of the open issues may turn out to be real challenges, the new questions offer great possibilities for interesting experimental and theoretical work on the way to a mature CNFET chemical sensing technology.

A Fabrication Flow

1   **Dicing**   Date:

	1	Protection with photoresist type:		AZ4533		
	2	Wafer spin coating (FIRST)				
	3	Baking	temperature:	100 °C	time:	60 s
	4	Dicing (CLA), parameters ? logsheet				
			cutting depth	300 um		
			dimensions:	6 x 6 mm^2		

2   **Cleaning after dicing**   Date:

	1	Acetone	temperature:	RT	time:	seconds
	2	Acetone	temperature:	50 °C	time:	10 min
	3	NMP	temperature:	50 °C	time:	5 h
	4	Acetone	temperature:	50 °C	time:	10 min
	5	Isopropanol	temperature:	50 °C	time:	5 min
	6	N_2 - blow dry				

3   **Synthesis of SWNTs**   Date:

	1	Particle adsorption	according to PhD thesis of L. Durrer
	2	SWNT synthesis in LPCVD	according to PhD thesis of L. Durrer

4   **Bondpads and electrodes structures**   Date:

	1	Spin coating	photoresist:	nLOF 2070 : EBR 2:1		
				acc step	*rpm*	*time*
			step 1:	3 s	3000	3 s
			step 2:	3 s	5000	45 s
	2	Baking	temperature:	115 °C	time:	60 s
	3	Exposure MJB3	intensity:	13 mW/cm^2	time:	2.4 s	dose:	30 mJ
	4	Baking	temperature:	115 °C	time:	60 s
	5	Development				

		1	MIF 826 pure		time:	50 s
		2	H_2O		time:	60 s
		3	N_2 - blow dry			

5   **Metal evaporation (PVD)**   Date:

1	Chromium (Cr)	thickness:	2 nm	rate:	0.2 Å/s
2	Gold (Au)	thickness:	40 / 60 nm	rate:	2 Å/s

6   **Lift-off**   Date:

1	Acetone	temperature:	50 °C	time:	1 h
2	Remove metal layer with pipette				
3	NMP	temperature:	50 °C	time:	3 h (at least)
4	Acetone	temperature:	50 °C	time:	10 min
5	Isopropanol	temperature:	50 °C	time:	5 min
6	N_2 - blow dry				

7   **E-beam lithography of AFM markers**   Date:

1   Spin coating of samples

1	Coating	photoresist:	P(MMA/MAA) (1:1) 950K		

		acc step	rpm	time
	step 1:	2 s	1000	3 s
	step 2:	4 s	5000	45 s

2	Baking	temperature:	180 °C	time:	15 min
3	Coating	photoresist:	PMMA (1:1) 950K in CB		

		acc step	rpm	time
	step 1:	2 s	1000	3 s
	steü 2:	4 s	5000	45 s

4	Baking	temperature:	180 °C	time:	15 min

2   E-beam

clearance dose:	$150\ \mu C/cm^2$	
dose factor:	15	
GDSII data type:	0.2	for small structures
	0.1	for big structures

Written dose = (clearance dose) x (dose factor) x (GDSII data type)

3   Development

1	MIBK : IPA (1:3)		time:	60 s
2	Isopropanol		time:	60 s

8   **Metal evaporation (PVD)**   Date:

1	Chromium (Cr)	thickness:	2 nm	rate:	0.2 Å/s
2	Gold (Au)	thickness:	40 nm	rate:	2 Å/s

9 **Lift-off**   Date:

1	Acetone	temperature:	50 °C	time:	1 h
2	Remove metal layer with pipette				
3	NMP	temperature:	50 °C	time:	3 h (at least)
4	Acetone	temperature:	50 °C	time:	10 min
5	Isopropanol	temperature:	50 °C	time:	5 min
6	N_2 - blow dry				

10 **Create E-beam masks of contacts**   Date:

1	AFM scans (to find SWNTs which are straight and have diameter 2 ... 2.5 nm)
2	Mask drawing (with Corel Draw and L-Edit)
3	Mask export (data type: GDSII)

11 **E-beam lithography of contacts**   Date:

1	Spin coating of samples					
	1	Coating	photoresist:	P(MMA/MAA) (1:1) 950K		
				acc step	*rpm*	*time*
			step 1:	2 s	1000	3 s
			step 2:	4 s	5000	45 s
	2	Baking	temperature:	180 °C	time:	15 min
	3	Coating	photoresist:	PMMA (1:1) 950K in CB		
				acc step	*rpm*	*time*
			step 1:	2 s	1000	4 s
			step 2:	4 s	5000	45 s
	4	Baking	temperature:	180 °C	time:	15 min

2	E-beam	clearance dose:	150 $\mu C/cm^2$		
		dose factor:	15		
		GDSII data type:	0.1 / 0.2	for small / big structures	
		Written dose = (clearance dose) x (dose factor) x (GDSII data type)			

3	Development			
	1	MIBK : IPA (1:3)	time:	60 s
	2	Isopropanol	time:	60 s

12 **Metal evaporation (PVD)**   Date:

1	Chromium (Cr)	thickness:	2 nm	rate:	0.2 Å/s
2	Gold (Au)	thickness:	40 / 60 nm	rate:	2 Å/s

117

13   **Lift-off**   Date:

1	Acetone	temperature:	50 °C	time:	1 h
2	Remove metal layer with pipette				
3	NMP	temperature:	50 °C	time:	3 h (at least)
4	Acetone	temperature:	50 °C	time:	10 min
5	Isopropanol	temperature:	50 °C	time:	5 min
6	N_2 - blow dry				

14   **Atomic layer depostion (ALD) of Al_2O_3**   Date:

1	Depostion	thickness:	40 nm	cycles:	460
		precursors	TMA / water	pulse	0.1 s / 4 s

15   **ALD Al_2O_3 removal at the bond pads**   Date:

1	Drop of photoresist to cover chip center area				AZ4533
2	Baking	temperature:	110 °C	time:	2 min
3	Etching with 6 % BHF			time:	20 s
4	H_2O rinse			time:	5 min
5	Remove photoresist mesa				
6	Acetone	temperature:	50 °C	time:	2 min
7	NMP	temperature:	50 °C	time:	10 h
8	Acetone	temperature:	50 °C	time:	10 min
9	Isopropanol	temperature:	50 °C	time:	5 min
10	N_2 - blow dry				

16   **Etch mask to open windows in ALD Al_2O_3**   Date:

1	Spin coating of samples				
	1	Place a piece of paper on the chuck			
	2	Coating	photoresist:	P(MMA/MAA) pure	

	acc step	rpm	time
step 1:	2 s	1000	3 s
step 2:	4 s	5000	45 s

	3	Baking	temperature:	180 °C	time:	15 min

2	E-beam	clearance dose:	$150\ \mu C/cm^2$	
		dose factor:	12	
		GDSII data type:	0.1	for windows
		Written dose = (clearance dose) x (dose factor) x (GDSII data type)		

3	Development			
	1	MIBK : IPA (1:3)	time:	60 s
	2	Isopropanol	time:	60 s

17   **ALD Al$_2$O$_3$ window etching**   Date: �

1	Baking	temperature:	150°C	time:	2 min
2	H$_2$O dip to wet the sample			time:	seconds
3	Etching with 6 % BHF			time:	25 s
4	H$_2$O rinse (stirring of the sample during first minute)			time:	5 min
5	Remove photoresist etch mask				
6	Acetone	temperature:	50 °C	time:	2 min
7	NMP	temperature:	50 °C	time:	10 min
8	Acetone	temperature:	50 °C	time:	10 min
9	Isopropanol	temperature:	50 °C	time:	5 min
10	N$_2$ - blow dry				

18   **Sample packaging and wire bonding**   Date: ▢

1	Brake 12 x 12 mm chips along halfway cuts in to 6 x 6 mm chips				
2	Drop of photoresist into the chip package		AZ4533		
3	Place sample into the package onto drop of photoresist				
4	Baking	temperature	110 °C	time:	2 min
5	Wire bonding in CLA FIRST				
	settings according to database of the wire bonder				

B Sensor output signal
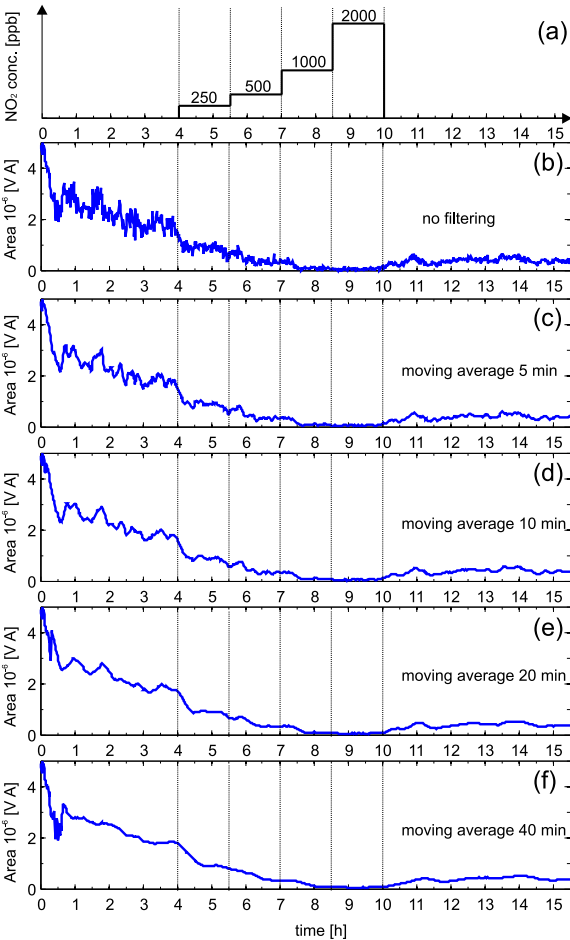
Figure B.1: NO_2 concentration profile during the experiement (a). ROS 3: calculated area enclosed by the n-type current branch and the x-axis versus time, non-filtered (b); low-pass filtered with a span of 5 min (c), 10 min (d), 20 min (e) and 40 min (f).

C Failure Mode and Effect Analysis

The Failure Mode and Effects Analysis (FMEA) was completed according to the guidelines given in [16]. During the project, the risk for certain items in the FMEA could not be soundly assessed. E.g. the item "Power consumption - to high" would result in need of large batteries or access to AC power supply would be required. However, the power consumption depends on readout circuitry and other system components, which are unknown in the current phase of the project. For such items 5 points out of 10 were given in the "Severity" and/or "Occurrence" rating by default. Based on the outlined methodology, an exhaustive list of items was first compiled into an FMEA table. In order to indentify the critical items to be addressed from the complete FMEA item list, three selection criteria were applied: high risk priority number (RPN), resources (estimated time and project budget) and item inter-dependencies (natural time order of items).

Item or Process Step	Potential Failure Mode	Potential Effects of Failure	S	Potential Cause(s)	O	Current Controls	D	RPN	Recommended Action
Limit of detection	Insufficient	Weak signals not detected	10	1/f noise too high	3	Sensor Characterization	1	30	Long tube channels or multiple tube devices
				Analyte-CNT interaction too weak					Lock-in measurements and filtering
Sensitivity	Insufficient	Can't distinguish between signal levels	8	Analyte-CNT interaction too weak	6	Sensor Characterization	1	48	CNT functionalization / structural defect induction
									Device preselection
Response time	Too long	Detection not fast enough	9	Sensitive area too small	7	Sensor Characterization	1	63	Long tube channels or multiple tube devices
									CNT functionalization / structural defect induction
									Device preselection
Recovery	Too slow	Output can not follow concentration profile	9	Desorption time of NO2 too long	7	Sensor Characterization	1	63	Recovery strategy self-heating
									Recovery strategy on-/off-chip heater
									Recovery strategy UV illumination
									Replace sensor after a while
Dynamic range / Measurement range	Insufficient	Output saturates above certain concentration	5	Gate coupling insufficient	7	Sensor Characterization	1	35	Gate oxide thinning, new oxide material or gate stack tuning
									CNT doping or metal workfunction tuning to make device p-type
									Pulsed I_dV_g measurements
									Several sensors with overlapping dynamic ranges
Degradation	Too fast	Lifetime is limited	8	Corrosion/oxidation of CNT and/or contacts due to environment	9	Long-term Characterization	1	72	Passivation/encapsulation/coating
									Replace sensor after a while
			8	Large bias currents causes migration, oxidation, etc.	3	Long-term Characterization	1	24	Use other recovery strategies (off-chip heaters, UV illumination)
									Pulsed bias voltage during self-heating
Cross-talk	Too high	Output is not reliable	9	Humidity / other interfering agents (e.g. NH3, CO2, ...) dope or gate the CNT	5	Cross-talk Characterization	1	45	CNT functionalization to render NO2 interaction more specific
			9	Humidity / other interfering agents (e.g. NH3, CO2, ...) change NO2 gas adsorption/desorption	5	Cross-talk Characterization	1	45	Compensation with additional specific humidity or interfering agents sensor
									More signal analysis (more I_dV_g points, PCA) and/or use additional signals (e.g. noise amplitudes)
			9	Temperature influences sensor output (transport or gas kinetics)	5	Cross-talk Characterization	1	45	More signal analysis (more IdVg points)
									Temperature compensation with other sensor
									Wheatstone bridge
			9	Light, radiation, fields	3	Cross-talk Characterization	1	27	Packaging and shielding

Function	Mode	Effect	S	Cause	O	Detection	D	RPN	Action
Drift	Too high	Output is not reliable	9	Humidity, other chemical interfering agents (e.g. NH_3, CO_2, ...) or temperature cause drift/noise	5	Long-term Characterization	1	45	Lock-in measurements and filtering
									Compensation with sensors for other stimuli
			9	Light, radiation, fields	5	Long-term Characterization	1	45	All of the above plus
									Packaging and shielding
Power consumption	Too high	Sensor requires large batteries or access to AC power supply	5	-	1	Sensor Characterization	1	5	Reduce V_{ds} (currently ~100mV)
									Sample sensor output only from time to time (0W in idle mode)
Gate voltage V_g	Too high	Several voltage sources required	5	Insufficient gate coupling	5	Sensor Characterization	1	25	Optimize gate oxide material
		ChemFET not CMOS compatible	6		4		1	24	CNT doping or metal workfunction tuning to change device into p-type
Readout circuitry power consumption	Too high	Sensor requires large batteries or access to AC power supply	3	ChemFET signals require conditioning and processing	3	Electrical Characterization	1	9	Optimize readout and ChemFET design
Heater power consumption	Too high	Sensor requires large batteries or access to AC power supply	6	Recovery requires high temperatures	3	Electrical Characterization	1	18	Optimize heater design and thermal coupling to ChemFETs
									Pulsed currents through heater
									Natural recovery combined with heating pulses to achieve desired recovery time
									Use other recovery strategies such as UV illumination
									CNT self heating
Heater size	Too large	Sensor (plus heater) doesn't fit in allocated slot	5	Recovery requires high temperatures	4	Layout	1	20	Optimize heater design and thermal coupling to ChemFETs
									Use other recovery strategies such as UV illumination
Readout circuit size	Too large	Sensor doesn't fit in allocated slot / chip size too large	6	ChemFET signals require conditioning and processing	4	Layout	1	24	Optimize readout and ChemFET design
			6	ChemFET device characteristics vary from device to device requiring flexible/programmable readout and/or sensor calibration	4	Layout	1	24	ChemFET fabrication process optimization
									Use different materials (e.g. Sapphire as gate oxide)
Number of ChemFETs	Too high	Sensor doesn't fit in allocated slot / costs	6	Device fabrication reproducibility / yield is low	3	Layout	1	18	Optimize fabrication process
									Integrated multiplexing and/or programmable device selector
Sensor fabrication yield	Too low	Sensor costs too high	8	CNT diameter, location, direction, length, number/density are not controlled	5	Characterization	1	40	Process control and monitoring
									Fabrication statistical process optimization
									Optimization of different process steps (e.g. CNT alignment, catalyst particle sorting, contact deposition methods)
									New materials (e.g. sapphire as gate oxide)
									Use different fabrication processes (e.g. dielectrophoresis, in situ growth on SOI)
									Fast device pre-selection strategies
Testing/Calibration	Too complex	Sensor costs too high	8	Device variability too high	4	Characterization	1	32	Optimize testing/calibration strategies
									Reduce device variability via PCM, new materials, etc.

Bibliography

[1] N. A. Campbell and J. B. Reece, *Biology - 6th edition*. San Francisco: Pearson Education Inc. publishing as Benjamin Cummings, 2002.

[2] Gas Leak Detection; http://en.wikipedia.org/wiki/Gas_leak_detection.

[3] U.S. Environmental Pollution Agency (EPA); http://www.epa.gov/airquality/nitrogenoxides/basic.html.

[4] Scott Speciality Gases; http://www.scottecatalog.com/.

[5] Schweizerische Unfallversicherungsanstalt (SUVA); http://www.suva.ch.

[6] R. Pohle, E. Simon, R. Schneider, M. Fleischer, R. Sollacher, H. Gao, K. Mueller, P. Jauch, M. Loepfe, H. P. Frerichs, and C. Wilbertz, "Fire detection with low power fet gas sensors," *Sensors and Actuators B: Chemical*, vol. 120, no. 2, pp. 669–672, 2007.

[7] M. Gill, S. Walker, A. Khan, S. M. Green, L. Kim, S. Gray, and B. Krauss, "Exhaled nitric oxide levels during acute asthma exacerbation," *Academic Emergency Medicine*, vol. 12, no. 7, pp. 579–586, 2005.

[8] M. Fleischer, E. Simon, E. Rumpel, H. Ulmer, M. Harbeck, M. Wandel, C. Fietzek, U. Weimar, and H. Meixner, "Detection of volatile compounds correlated to human diseases through breath analysis with chemical sensors," *Sensors and Actuators B: Chemical*, vol. 83, no. 1-3, pp. 245–249, 2002.

[9] S. Drost, "Gassensoren," in *Sensortechnik: Handbuch für Praxis und Wissenschaft*, H.-R. Traenkler and E. Obermeier, Eds. Berlin: Springer, 1998.

[10] Alphasense; http://www.alphasense.com.

[11] E2v Technologies; http://www.e2v.com.

[12] Draeger; http://www.draeger.com.

[13] City Technology; http://www.citytech.com.

[14] Applied Sensor; http://www.appliedsensor.com.

[15] J. Kong, N. R. Franklin, C. Zhou, M. G. Chapline, S. Peng, K. Cho, and H. Dai, "Nanotube molecular wires as chemical sensors," *Science*, vol. 287, no. 5453, pp. 622–625, 2000.

[16] Rath and Strong, "Rath & strong's six sigma pocket guide," 2006, iSBN: 0974632872.

[17] C. Stampfer, "Electromechanical transducers based on single-walled carbon nanotubes," Ph.D. dissertation, No. 16968, ETH Zurich, 2007.

[18] A. Jungen, "Direct integration by synthesis and properties of single-walled carbon nanotubes," Ph.D. dissertation, No. 17089, ETH Zurich, 2007.

[19] T. Helbling, "Carbon nanotube field effect transistors as electromechanical transducers," Ph.D. dissertation, No. 18823, ETH Zurich, 2010.

[20] L. Durrer, "Controlled single-walled carbon nanotube growth for sensing applications," Ph.D. dissertation, No. 18947, ETH Zurich, 2010.

[21] S. Drittenbass, "Ultra small single walled carbon nanotube pressure sensors," Master's thesis, ETH Zurich, 2008.

[22] M. Biercuk, S. Ilani, C. Marcus, and P. McEuen, "Electrical transport in single-wall carbon nanotubes," in *Carbon Nanotubes Topics in Applied Physics*, C. E. Ascheron and A. H. Duhm, Eds. Springer, 2008, vol. 111/2008, pp. 455–493.

[23] S. Reich, C. Thomsen, and J. Maultzsche, *Carbon Nanotubes*. Wiley-VCH, 2003.

[24] M. Dresselhaus, G. Dresselhaus, and E. Avouris P., *Carbon Nanotubes: Synthesis, Structure, Properties and Applications*. Springer, 2001.

[25] R. Saito, G. Dresselhaus, and M. Dresselhaus, *Physical Properties of Carbon Nanotubes*. Imperial College Press, 2001.

[26] S. Datta, *Electronic Transport in Mesoscopic Systems*. Cambridge Studies in Semiconductor Physics Series, 1998.

[27] J.-C. Charlier, X. Blase, and S. Roche, "Electronic and transport properties of nanotubes," *Reviews of Modern Physics*, vol. 79, no. 2, p. 677, 2007.

[28] P. Avouris, Z. Chen, and V. Perebeinos, "Carbon-based electronics," *Nat Nano*, vol. 2, no. 10, pp. 605–615, 2007.

[29] H. Dai, "Carbon nanotubes: Synthesis, integration, and properties," *Accounts of Chemical Research*, vol. 35, no. 12, pp. 1035–1044, 2002.

[30] P. L. McEuen, M. S. Fuhrer, and P. Hongkun, "Single-walled carbon nanotube electronics," *Nanotechnology, IEEE Transactions on*, vol. 1, no. 1, pp. 78–85, 2002.

[31] A. Robert-Peillard and S. V. Rotkin, "Modeling hysteresis phenomena in nanotube field-effect transistors," *Nanotechnology, IEEE Transactions on*, vol. 4, no. 2, pp. 284–288, 2005.

[32] S. Iijima, "Helical microtubules of graphitic carbon," *Nature*, vol. 354, no. 6348, pp. 56–58, 1991.

[33] S. Iijima and T. Ichihashi, "Single-shell carbon nanotubes of 1-nm diameter," *Nature*, vol. 363, no. 6430, pp. 603–605, 1993.

[34] V. N. Popov, "Carbon nanotubes: properties and application," *Materials Science and Engineering: R: Reports*, vol. 43, no. 3, pp. 61–102, 2004.

[35] R. Martel, T. Schmidt, H. R. Shea, T. Hertel, and P. Avouris, "Single- and multi-wall carbon nanotube field-effect transistors," *Applied Physics Letters*, vol. 73, no. 17, pp. 2447–2449, 1998.

[36] S. J. Tans, A. R. M. Verschueren, and C. Dekker, "Room-temperature transistor based on a single carbon nanotube," *Nature*, vol. 393, no. 6680, pp. 49–52, 1998.

[37] Z. Wu, Z. Chen, X. Du, J. M. Logan, J. Sippel, M. Nikolou, K. Kamaras, J. R. Reynolds, D. B. Tanner, A. F. Hebard, and A. G. Rinzler, "Transparent, conductive carbon nanotube films," *Science*, vol. 305, no. 5688, pp. 1273–1276, 2004.

[38] Y. Saito and S. Uemura, "Field emission from carbon nanotubes and its application to electron sources," *Carbon*, vol. 38, no. 2, pp. 169–182, 2000.

[39] M. S. Fuhrer, B. M. Kim, T. Durkop, and T. Brintlinger, "High-mobility nanotube transistor memory," *Nano Letters*, vol. 2, no. 7, pp. 755–759, 2002.

[40] K. Balasubramanian and M. Burghard, "Biosensors based on carbon nanotubes," *Analytical and Bioanalytical Chemistry*, vol. 385, no. 3, pp. 452–468, 2006.

[41] C. Hierold, A. Jungen, C. Stampfer, and T. Helbling, "Nano electromechanical sensors based on carbon nanotubes," *Sensors and Actuators A: Physical*, vol. 136, no. 1, pp. 51–61, 2007.

[42] A. Modi, N. Koratkar, E. Lass, B. Wei, and P. M. Ajayan, "Miniaturized gas ionization sensors using carbon nanotubes," *Nature*, vol. 424, no. 6945, pp. 171–174, 2003.

[43] C. Stampfer, T. Helbling, D. Obergfell, B. Schoberle, M. K. Tripp, A. Jungen, S. Roth, V. M. Bright, and C. Hierold, "Fabrication of single-walled carbon-nanotube-based pressure sensors," *Nano Letters*, vol. 6, no. 2, pp. 233–237, 2006.

[44] C. Stampfer, A. Jungen, R. Linderman, D. Obergfell, S. Roth, and C. Hierold, "Nano-electromechanical displacement sensing based on single-walled carbon nanotubes," *Nano Letters*, vol. 6, no. 7, pp. 1449–1453, 2006.

[45] P. Kim and C. M. Lieber, "Nanotube nanotweezers," *Science*, vol. 286, no. 5447, pp. 2148–2150, 1999.

[46] M. Freitag, J. Chen, J. Tersoff, J. C. Tsang, Q. Fu, J. Liu, and P. Avouris, "Mobile ambipolar domain in carbon-nanotube infrared emitters," *Physical Review Letters*, vol. 93, no. 7, p. 076803, 2004.

[47] X. Qiu, M. Freitag, V. Perebeinos, and P. Avouris, "Photoconductivity spectra of single-carbon nanotubes: Implications on the nature of their excited states," *Nano Letters*, vol. 5, no. 4, pp. 749–752, 2005.

[48] M. E. Itkis, F. Borondics, A. Yu, and R. C. Haddon, "Bolometric infrared photoresponse of suspended single-walled carbon nanotube films," *Science*, vol. 312, no. 5772, pp. 413–416, 2006.

[49] M. S. Dresselhaus, G. Dresselhaus, and R. Saito, "Physics of carbon nanotubes," *Carbon*, vol. 33, no. 7, pp. 883–891, 1995.

[50] C. L. Kane and E. J. Mele, "Size, shape, and low energy electronic structure of carbon nanotubes," *Physical Review Letters*, vol. 78, no. 10, p. 1932, 1997.

[51] A. Kleiner and S. Eggert, "Band gaps of primary metallic carbon nanotubes," *Physical Review B*, vol. 63, no. 7, p. 073408, 2001.

[52] A. Javey, J. Guo, Q. Wang, M. Lundstrom, and H. Dai, "Ballistic carbon nanotube field-effect transistors," *Nature*, vol. 424, no. 6949, pp. 654–657, 2003.

[53] P. L. McEuen, "Single-wall carbon nanotubes," *Physics World*, vol. 13, p. 31, 2000.

[54] M. Freitag, A. T. Johnson, S. V. Kalinin, and D. A. Bonnell, "Role of single defects in electronic transport through carbon nanotube field-effect transistors," *Physical Review Letters*, vol. 89, no. 21, p. 216801, 2002.

[55] N. Neophytou, D. Kienle, E. Polizzi, and M. P. Anantram, "Influence of defects on nanotube transistor performance," *Applied Physics Letters*, vol. 88, no. 24, pp. 242 106–3, 2006.

[56] B. Biel, F. J. Carcia-Vidal, A. Rubio, and F. Flores, "Ab initio study of transport properties in defected carbon nanotubes: an o(n) approach," *Journal of Physics: Condensed Matter*, vol. 20, no. 29, p. 294214, 2008.

[57] C. Roman, T. Helbling, and C. Hierold, "Single-walled carbon nanotube sensor concepts," in *Springer Handbook of Nanotechnology, 3rd ed.*, B. Bhushan, Ed. Berlin Heidelberg: Springer, 2009.

[58] F. Leonard and J. Tersoff, "Role of fermi-level pinning in nanotube schottky diodes," *Physical Review Letters*, vol. 84, no. 20, p. 4693, 2000.

[59] H. Lin and S. Tiwari, "Localized charge trapping due to adsorption in nanotube field-effect transistor and its field-mediated transport," *Applied Physics Letters*, vol. 89, no. 7, p. 073507, 2006.

[60] W. Kim, A. Javey, O. Vermesh, Q. Wang, Y. Li, and H. Dai, "Hysteresis caused by water molecules in carbon nanotube field-effect transistors," *Nano Letters*, vol. 3, no. 2, pp. 193–198, 2003.

[61] H. Shimauchi, Y. Ohno, S. Kishimoto, and T. Mizutani, "Suppression of hysteresis in carbon nanotube field-effect transistors: Effect of contamination induced by device fabrication process," *Japanese Journal of Applied Physics*, vol. 45, pp. 5501–5503, 2006.

[62] S. M. Sze and K. N. Kwok, *Physics of Semiconductor Devices, 3rd ed.* Hoboken: John Wiley & Sons, 2007.

[63] T. Helbling, C. Hierold, C. Roman, L. Durrer, M. Mattmann, and V. M. Bright, "Long term investigations of carbon nanotube transistors encapsulated by atomic-layer-deposited Al_2O_3 for sensor applications," *Nanotechnology*, vol. 20, no. 43, p. 434010, 2009.

[64] P. Hu, C. Zhang, A. Fasoli, V. Scardaci, S. Pisana, T. Hasan, J. Robertson, W. I. Milne, and A. C. Ferrari, "Hysteresis suppression in self-assembled single-wall nanotube field effect transistors," *Physica E: Low-dimensional Systems and Nanostructures*, vol. 40, no. 7, pp. 2278–2282, 2008.

[65] M. Muoth, T. Helbling, L. Durrer, S. W. Lee, C. Roman, and C. Hierold, "Hysteresis-free operation of suspended carbon nanotube transistors," *Nat Nano*, vol. 5, no. 8, pp. 589–592, 2010.

[66] R. H. Fowler and L. Nordheim, "Electron emission in intense electric fields," *Proceedings of the Royal Society of London. Series A, Containing Papers of a Mathematical and Physical Character*, vol. 119, no. 781, pp. 173–181, 1928.

[67] M. Mattmann, C. Roman, T. Helbling, D. Bechstein, L. Durrer, R. Pohle, M. Fleischer, and C. Hierold, "Pulsed gate sweep strategies for hysteresis reduction in carbon nanotube transistors for low concentration NO_2 gas detection," *Nanotechnology*, vol. 21, no. 18, p. 185501, 2010.

[68] E. S. Snow, F. K. Perkins, E. J. Houser, S. C. Badescu, and T. L. Reinecke, "Chemical detection with a single-walled carbon nanotube capacitor," *Science*, vol. 307, no. 5717, pp. 1942–1945, 2005.

[69] J. T. W. Yeow and J. P. M. She, "Carbon nanotube-enhanced capillary condensation for a capacitive humidity sensor," *Nanotechnology*, vol. 17, no. 21, p. 5441, 2006.

[70] J. C. Robert, R. F. Nathan, K. Jing, C. Jien, W. T. Thomas, Z. Yuegang, and D. Hongjie, "Molecular photodesorption from single-walled carbon nanotubes," *Applied Physics Letters*, vol. 79, no. 14, pp. 2258–2260, 2001.

[71] A. Goldoni and et al., "Sensing gases with carbon nanotubes: a review of the actual situation," *Journal of Physics: Condensed Matter*, vol. 22, no. 1, p. 013001, 2010.

[72] Y. Wang and J. T. W. Yeow, "A review of carbon nanotubes-based gas sensors," *Journal of Sensors*, vol. 2009, p. 493904, 2009.

[73] T. Zhang, S. Mubeen, N. V. Myung, and M. A. Deshusses, "Recent progress in carbon nanotube-based gas sensors," *Nanotechnology*, vol. 19, no. 33, p. 332001, 2008.

[74] D. Kauffman and A. Star, "Carbon nanotube gas and vapor sensors," *Angewandte Chemie International Edition*, vol. 47, no. 35, pp. 6550–6570, 2008.

[75] E. S. Snow, F. K. Perkins, and J. A. Robinson, "Chemical vapor detection using single-walled carbon nanotubes," *Chemical Society Reviews*, vol. 35, no. 9, pp. 790–798, 2006.

[76] Y. W. Cheng, Z. Yang, H. Wei, Y. Y. Wang, L. Wei, and Y. F. Zhang, "Progress in carbon nanotube gas sensor research," *Acta Physico-Chimica Sinica*, vol. 26, no. 12, pp. 3127–3142, 2010.

[77] J. Wang, "Carbon-nanotube based electrochemical biosensors: A review," *Electroanalysis*, vol. 17, no. 1, pp. 7–14, 2005.

[78] P. Hu, J. Zhang, L. Li, Z. Wang, W. ONeill, and P. Estrela, "Carbon nanostructure-based field-effect transistors for label-free chemical/biological sensors," *Sensors*, vol. 10, no. 5, pp. 5133–5159, 2010.

[79] B. L. Allen, P. D. Kichambare, and A. Star, "Carbon nanotube field-effect-transistor-based biosensors," *Advanced Materials*, vol. 19, no. 11, pp. 1439–1451, 2007.

[80] C. B. Jacobs, M. J. Peairs, and B. J. Venton, "Review: Carbon nanotube based electrochemical sensors for biomolecules," *Analytica Chimica Acta*, vol. 662, no. 2, pp. 105–127, 2010.

[81] M. Cinke, J. Li, B. Chen, A. Cassell, L. Delzeit, J. Han, and M. Meyyappan, "Pore structure of raw and purified hipco single-walled carbon nanotubes," *Chemical Physics Letters*, vol. 365, no. 1-2, pp. 69–74, 2002.

[82] Y. Shimizu and M. Egashira, "Basic aspects and challenges of semiconductor gas sensors," *MRS Bulletin*, vol. 24, p. 18, 1999.

[83] Y. Takao, K. Miyazaki, Y. Shimizu, and M. Egashira, "High ammonia sensitive semiconductor gas sensors with double-layer structure and interface electrodes," *Journal of The Electrochemical Society*, vol. 141, no. 4, pp. 1028–1034, 1994.

[84] S. Peng, K. Cho, P. Qi, and H. Dai, "Ab initio study of cnt NO_2 gas sensor," *Chemical Physics Letters*, vol. 387, no. 4-6, pp. 271–276, 2004.

[85] H. Chang, J. D. Lee, S. M. Lee, and Y. H. Lee, "Adsorption of NH_3 and NO_2 molecules on carbon nanotubes," *Applied Physics Letters*, vol. 79, no. 23, pp. 3863–3865, 2001.

[86] J. Zhao, A. Buldum, J. Han, and J. Lu, "Gas molecule adsorption in carbon nanotubes and nanotube bundles," *Nanotechnology*, vol. 13, no. 2, p. 195, 2002.

[87] D. L. Carroll, P. Redlich, X. Blase, J. C. Charlier, S. Curran, P. M. Ajayan, S. Roth, and M. Ruehle, "Effects of nanodomain formation on the electronic structure of doped carbon nanotubes," *Physical Review Letters*, vol. 81, no. 11, p. 2332, 1998.

[88] J. A. Robinson, E. S. Snow, S. C. Badescu, T. L. Reinecke, and F. K. Perkins, "Role of defects in single-walled carbon nanotube chemical sensors," *Nano Letters*, vol. 6, no. 8, pp. 1747–1751, 2006.

[89] L. Valentini, F. Mercuri, I. Armentano, C. Cantalini, S. Picozzi, L. Lozzi, S. Santucci, A. Sgamellotti, and J. M. Kenny, "Role of defects on the gas sensing properties of carbon nanotubes thin films: experiment and theory," *Chemical Physics Letters*, vol. 387, no. 4-6, pp. 356–361, 2004.

[90] F. Mercuri, A. Sgamellotti, L. Valentini, I. Armentano, and J. M. Kenny, "Vacancy-induced chemisorption of no_2 on carbon nanotubes: A combined theoretical and experimental study," *The Journal of Physical Chemistry B*, vol. 109, no. 27, pp. 13 175–13 179, 2005.

[91] J. Andzelm, N. Govind, and A. Maiti, "Nanotube-based gas sensors - role of structural defects," *Chemical Physics Letters*, vol. 421, no. 1-3, pp. 58–62, 2006.

[92] A. Goldoni, L. Petaccia, L. Gregoratti, B. Kaulich, A. Barinov, S. Lizzit, A. Laurita, L. Sangaletti, and R. Larciprete, "Spectroscopic characterization of contaminants and interaction with gases in single-walled carbon nanotubes," *Carbon*, vol. 42, no. 10, pp. 2099–2112, 2004.

[93] J. Zhang, A. Boyd, A. Tselev, M. Paranjape, and P. Barbara, "Mechanism of NO_2 detection in carbon nanotube field effect transistor chemical sensors," *Applied Physics Letters*, vol. 88, no. 12, pp. 123 112–3, 2006.

[94] S. Auvray, J. Borghetti, M. F. Goffman, A. Filoramo, V. Derycke, J. P. Bourgoin, and O. Jost, "Carbon nanotube transistor optimization by chemical control of the nanotube–metal interface," *Applied Physics Letters*, vol. 84, no. 25, pp. 5106–5108, 2004.

[95] I. Heller, A. M. Janssens, J. Mannik, E. D. Minot, S. G. Lemay, and C. Dekker, "Identifying the mechanism of biosensing with carbon nanotube transistors," *Nano Letters*, vol. 8, no. 2, pp. 591–595, 2007.

[96] T. Helbling, C. Hierold, L. Durrer, C. Roman, R. Pohle, and M. Fleischer, "Suspended and non-suspended carbon nanotube transistors for NO_2 sensing - a qualitative comparison," *Physica Status Solidi B-Basic Solid State Physics*, vol. 245, no. 10, pp. 2326–2330, 2008.

[97] M. Penza, G. Cassano, R. Rossi, A. Rizzo, M. A. Signore, M. Alvisi, N. Lisi, E. Serra, and R. Giorgi, "Effect of growth catalysts on gas sensivity in carbon nanotube film based chemiresistive sensors," *Applied Physics Letters*, vol. 90, no. 10, pp. 103 101–3, 2007.

[98] J. Li, Y. Lu, Q. Ye, M. Cinke, J. Han, and M. Meyyappan, "Carbon nanotube sensors for gas and organic vapor detection," *Nano Letters*, vol. 3, no. 7, pp. 929–933, 2003.

[99] P. Qi, O. Vermesh, M. Grecu, A. Javey, Q. Wang, H. Dai, S. Peng, and K. J. Cho, "Toward large arrays of multiplex functionalized carbon nanotube sensors for highly sensitive and selective molecular detection," *Nano Letters*, vol. 3, no. 3, pp. 347–351, 2003.

[100] A. Star, V. Joshi, S. Skarupo, D. Thomas, and J.-C. P. Gabriel, "Gas sensor array based on metal-decorated carbon nanotubes," *The Journal of Physical Chemistry B*, vol. 110, no. 42, pp. 21 014–21 020, 2006.

[101] E. H. Espinosa, R. Ionescu, C. Bittencourt, A. Felten, R. Erni, G. Van Tendeloo, J. J. Pireaux, and E. Llobet, "Metal-decorated multi-wall carbon nanotubes for low temperature gas sensing," *Thin Solid Films*, vol. 515, no. 23, pp. 8322–8327, 2007.

[102] M. Penza, G. Cassano, R. Rossi, M. Alvisi, A. Rizzo, M. A. Signore, T. Dikonimos, E. Serra, and R. Giorgi, "Enhancement of sensitivity in gas chemiresistors based on carbon nanotube surface functionalized with noble metal (au, pt) nanoclusters," *Applied Physics Letters*, vol. 90, no. 17, pp. 173 123–3, 2007.

[103] K. Bradley, J.-C. P. Gabriel, A. Star, and G. Gruner, "Short-channel effects in contact-passivated nanotube chemical sensors," *Applied Physics Letters*, vol. 83, no. 18, pp. 3821–3823, 2003.

[104] I. Heller, J. Mannik, S. G. Lemay, and C. Dekker, "Optimizing the signal-to-noise ratio for biosensing with carbon nanotube transistors," *Nano Letters*, vol. 9, no. 1, pp. 377–382, 2008.

[105] X. Liu, Z. Luo, S. Han, T. Tang, D. Zhang, and C. Zhou, "Band engineering of carbon nanotube field-effect transistors via selected area chemical gating," *Applied Physics Letters*, vol. 86, no. 24, pp. 243 501–3, 2005.

[106] D. Kaminishi, H. Ozaki, Y. Ohno, K. Maehashi, K. Inoue, K. Matsumoto, Y. Seri, A. Masuda, and H. Matsumura, "Air-stable n-type carbon nanotube field-effect transistors with Si_3N_4 passivation films fabricated by catalytic chemical vapor deposition," *Applied Physics Letters*, vol. 86, no. 11, pp. 113 115–3, 2005.

[107] N. Peng, Q. Zhang, O. K. Tan, and N. Marzari, "Study of gaseous inter- actions in carbon nanotube field-effect transistors through selective Si_3N_4 passivation," *Nanotechnology*, vol. 19, no. 46, p. 5, 2008.

[108] R. Moos, K. Sahner, M. Fleischer, U. Guth, N. Barsan, and U. Weimar, "Solid state gas sensor research in germany - a status report," *Sensors*, vol. 9, no. 6, pp. 4323–4365, 2009.

[109] M. W. Ahn, K. S. Park, J. H. Heo, D. W. Kim, K. J. Choi, and J. G. Park, "On-chip fabrication of Zno-nanowire gas sensor with high gas sensitivity," *Sensors and Actuators B: Chemical*, vol. 138, no. 1, pp. 168–173, 2009.

[110] J. Wan, S.-R. Deng, R. Yang, Z. Shu, B.-R. Lu, S.-Q. Xie, Y. Chen, E. Huq, R. Liu, and X.-P. Qu, "Silicon nanowire sensor for gas detection fabricated by nanoimprint on SU8/SiO_2/PMMA trilayer," *Microelectronic Engineering*, vol. 86, no. 4-6, pp. 1238–1242, 2008.

[111] I.-D. Kim, A. Rothschild, B. H. Lee, D. Y. Kim, S. M. Jo, and H. L. Tuller, "Ultrasensitive chemiresistors based on electrospun TiO_2 nanofibers," *Nano Letters*, vol. 6, no. 9, pp. 2009–2013, 2006.

[112] S. Bianchi, E. Comini, M. Ferroni, G. Faglia, A. Vomiero, and G. Sberveglieri, "Indium oxide quasi-monodimensional low temperature gas sensor," *Sensors and Actuators B: Chemical*, vol. 118, no. 1-2, pp. 204–207, 2006.

[113] D. Zhang, Z. Liu, C. Li, T. Tang, X. Liu, S. Han, B. Lei, and C. Zhou, "Detec- tion of NO_2 down to ppb levels using individual and multiple In_2O_3 nano- wire devices," *Nano Letters*, vol. 4, no. 10, pp. 1919–1924, 2004.

[114] C. Mueller, T. Nirmaier, A. Ruegemer, and M. v. Schickfus, "Sensitive NO_2 detection with surface acoustic wave devices using a cyclic measuring tech- nique," *Sensors and Actuators B: Chemical*, vol. 68, no. 1-3, pp. 69–73, 2000.

[115] A. Z. Sadek, W. Wlodarski, K. Shin, R. B. Kaner, and K. Kalantar-Zadeh, "A layered surface acoustic wave gas sensor based on a polyaniline/In_2O_3 nanofibre composite," *Nanotechnology*, vol. 17, no. 17, p. 4488, 2006.

[116] C. Park, J. Fergus, N. Miura, J. Park, and A. Choi, "Solid-state electrochemi- cal gas sensors," *Ionics*, vol. 15, no. 3, pp. 261–284, 2009.

[117] P. Jasinski, "Solid-state electrochemical gas sensors," *Materials Science- Poland*, vol. 24, no. 1, pp. 269–278, 2006.

[118] J. Lagois, "Elektrochemische gassensoren," in *Sensortechnik: Handbuch für Praxis und Wissenschaft*, H.-R. Traenkler and E. Obermeier, Eds.   Berlin: Springer, 1998.

[119] L. Hsu, T. Ativanichayaphong, H. Cao, J. Sin, M. Graff, H. E. Stephanou, and J.-C. Chiao, "Evaluation of commercial metal-oxide based NO_2 sensors," *Sensor Review*, vol. 27, no. 2, pp. 121–131, 2007.

[120] L. Durrer, T. Helbling, C. Zenger, A. Jungen, C. Stampfer, and C. Hierold, "Swnt growth by cvd on ferritin-based iron catalyst nanoparticles towards cnt sensors," *Sensors and Actuators B: Chemical*, vol. 132, no. 2, pp. 485–490, 2008.

[121] L. Durrer, J. Greenwald, T. Helbling, M. Muoth, R. Riek, and C. Hierold, "Narrowing swnt diameter distribution using size-separated ferritin-based fe catalysts," *Nanotechnology*, vol. 20, no. 35, p. 355601, 2009.

[122] N. D. Chasteen and P. M. Harrison, "Mineralization in ferritin: An efficient means of iron storage," *Journal of Structural Biology*, vol. 126, no. 3, pp. 182–194, 1999.

[123] R. M. Kramer, L. A. Sowards, M. J. Pender, M. O. Stone, and R. R. Naik, "Constrained iron catalysts for single-walled carbon nanotube growth," *Langmuir*, vol. 21, no. 18, pp. 8466–8470, 2005.

[124] Y. Li, W. Kim, Y. Zhang, M. Rolandi, D. Wang, and H. Dai, "Growth of single-walled carbon nanotubes from discrete catalytic nanoparticles of various sizes," *The Journal of Physical Chemistry B*, vol. 105, no. 46, pp. 11 424–11 431, 2001.

[125] K. Chikkadi, "Charaterization of atomic layer deposited aluminum oxide as passivation layer for carbon nanotube field effect transistors," Master's thesis, ETH Zurich, 2009.

[126] R. L. Puurunen, "Surface chemistry of atomic layer deposition: A case study for the trimethylaluminum/water process," *Journal of Applied Physics*, vol. 97, no. 12, pp. 121 301–52, 2005.

[127] S. M. George, A. W. Ott, and J. W. Klaus, "Surface chemistry for atomic layer growth," *The Journal of Physical Chemistry*, vol. 100, no. 31, pp. 13 121–13 131, 1996.

[128] S. Drittenbass, "Investigations on the gate hysteresis in single-walled carbon nanotube field effect transistors," Master's thesis, ETH Zurich, 2007.

[129] M. Mattmann, T. Helbling, L. Durrer, C. Roman, C. Hierold, R. Pohle, and M. Fleischer, "Sub-ppm NO_2 detection by Al_2O_3 contact passivated carbon nanotube field effect transistors," *Applied Physics Letters*, vol. 94, no. 18, pp. 183 502–3, 2009.

[130] M. D. Groner, F. H. Fabreguette, J. W. Elam, and S. M. George, "Low-temperature Al_2O_3 atomic layer deposition," *Chemistry of Materials*, vol. 16, no. 4, pp. 639–645, 2004.

[131] M. D. Groner, S. M. George, R. S. McLean, and P. F. Carcia, "Gas diffusion barriers on polymers using al_2o_3 atomic layer deposition," *Applied Physics Letters*, vol. 88, no. 5, p. 051907, 2006.

[132] S. Heinze, J. Tersoff, R. Martel, V. Derycke, J. Appenzeller, and P. Avouris, "Carbon nanotubes as schottky barrier transistors," *Physical Review Letters*, vol. 89, no. 10, p. 106801, 2002.

[133] V. Derycke, R. Martel, J. Appenzeller, and P. Avouris, "Carbon nanotube inter- and intramolecular logic gates," *Nano Letters*, vol. 1, no. 9, pp. 453–456, 2001.

[134] P. Avouris, R. Martel, V. Derycke, and J. Appenzeller, "Carbon nanotube transistors and logic circuits," *Physica B: Condensed Matter*, vol. 323, no. 1-4, pp. 6–14, 2002.

[135] P. G. Collins, K. Bradley, M. Ishigami, and A. Zettl, "Extreme oxygen sensitivity of electronic properties of carbon nanotubes," *Science*, vol. 287, no. 5459, pp. 1801–1804, 2000.

[136] K. Donghun and et al., "Oxygen-induced p-type doping of a long individual single-walled carbon nanotube," *Nanotechnology*, vol. 16, no. 8, p. 1048, 2005.

[137] D. B. Farmer and R. G. Gordon, "Atomic layer deposition on suspended single-walled carbon nanotubes via gas-phase noncovalent functionalization," *Nano Letters*, vol. 6, no. 4, pp. 699–703, 2006.

[138] A. Javey, J. Guo, D. B. Farmer, Q. Wang, E. Yenilmez, R. G. Gordon, M. Lundstrom, and H. Dai, "Self-aligned ballistic molecular transistors and electrically parallel nanotube arrays," *Nano Letters*, vol. 4, no. 7, pp. 1319–1322, 2004.

[139] T. Helbling, R. Pohle, L. Durrer, C. Stampfer, C. Roman, A. Jungen, M. Fleischer, and C. Hierold, "Sensing NO_2 with individual suspended single-walled carbon nanotubes," *Sensors and Actuators B: Chemical*, vol. 132, no. 2, pp. 491–497, 2008.

[140] S. A. McGill, S. G. Rao, P. Manandhar, P. Xiong, and S. Hong, "High-performance, hysteresis-free carbon nanotube field-effect transistors via directed assembly," *Applied Physics Letters*, vol. 89, no. 16, pp. 163 123–3, 2006.

[141] M. Mattmann, T. Helbling, L. Durrer, C. Roman, R. Pohle, M. Fleischer, and C. Hierold, "Hysteresis reduction and measurement range enhancement of carbon nanotube based NO_2 gas sensors by pulsed gate voltages," *Procedia Chemistry*, vol. 1, no. 1, pp. 1431–1434, 2009.

[142] M. Mattmann, D. Bechstein, C. Roman, K. Chikkadi, T. Helbling, L. Durrer, R. Pohle, M. Fleischer, and C. Hierold, "Electrical initialization to erase history in hysteretic carbon nanotube transistors for sensing applications," *Procedia Engineering*, vol. 5, pp. 1119–1122, 2010.

[143] J. Tersoff, "Low-frequency noise in nanoscale ballistic transistors," *Nano Letters*, vol. 7, no. 1, pp. 194–198, 2006.

[144] Y. W. Chang, J. S. Oh, S. H. Yoo, H. H. Choi, and K.-H. Yoo, "Electrically refreshable carbon-nanotube-based gas sensors," *Nanotechnology*, vol. 18, no. 43, p. 435504, 2007.

[145] M. H. Ervin, A. M. Dorsey, and N. M. Salaets, "Hysteresis contributions to the apparent gate pulse refreshing of carbon nanotube based sensors," *Nanotechnology*, vol. 20, no. 34, p. 345503, 2009.

[146] M. Cho, R. Degraeve, P. Roussel, B. Govoreanu, B. Kaczer, M. B. Zahid, E. Simoen, A. Arreghini, M. Jurczak, J. V. Houdt, and G. Groeseneken, "A consistent model for oxide trap profiling with the trap spectroscopy by charge injection and sensing (tscis) technique," *Solid-State Electronics*, vol. 54, no. 11, pp. 1384–1391, 2010.

[147] J. Nygard, D. H. Cobden, and P. E. Lindelof, "Kondo physics in carbon nanotubes," *Nature*, vol. 408, no. 6810, pp. 342–346, 2000.

[148] L. Marty, V. Bouchiat, C. Naud, M. Chaumont, T. Fournier, and A. M. Bonnot, "Schottky barriers and coulomb blockade in self-assembled carbon nanotube fets," *Nano Letters*, vol. 3, no. 8, pp. 1115–1118, 2003.

[149] M. Mattmann, D. Bechstein, C. Roman, K. Chikkadi, and C. Hierold, "Reduction of gate hysteresis above ambient temperature via ambipolar pulsed gate sweeps in carbon nanotube field effect transistors for sensor applications," *Applied Physics Letters*, vol. 97, no. 15, pp. 153 103–3, 2010.

[150] D. Sung, S. Hong, Y.-H. Kim, N. Park, S. Kim, S. L. Maeng, and K.-C. Kim, "Ab initio study of the effect of water adsorption on the carbon nanotube field-effect transistor," *Applied Physics Letters*, vol. 89, no. 24, pp. 243 110–3, 2006.

[151] G. E. Ewing, "Ambient thin film water on insulator surfaces," *ChemInform*, vol. 37, no. 25, pp. no–no, 2006.

[152] X. Wang, M. Zhao, and D. D. Nolte, "Ambient molecular water accumulation on silica surfaces detected by a reflectance interference optical balance," *Applied Physics Letters*, vol. 97, no. 18, pp. 183 702–3, 2010.

[153] A. Verdaguer, C. Weis, G. Oncins, G. Ketteler, H. Bluhm, and M. Salmeron, "Growth and structure of water on SiO_2 films on Si investigated by kelvin probe microscopy and in situ x-ray spectroscopies," *Langmuir*, vol. 23, no. 19, pp. 9699–9703, 2007.

[154] P. Thissen, G. Grundmeier, S. Wippermann, and W. G. Schmidt, "Water adsorption on the alpha -Al_2O_3(0001) surface," *Physical Review B*, vol. 80, no. 24, p. 245403, 2009.

[155] C. E. Mortimer and U. Müller, *Das Basiswissen der Chemie*. Stuttgart: Thieme, 2003.

[156] D. Buchanan and D. Felnhofer, "On the characterization of electronically active defects in high-k gate dielectrics," in *Defects in High-k Gate Dielectric Stacks*, E. Gusev, Ed. Netherlands: Springer, 2006, pp. 41–59.

[157] D. Estrada, S. Dutta, A. Liao, and E. Pop, "Reduction of hysteresis for carbon nanotube mobility measurements using pulsed characterization," *Nanotechnology*, vol. 21, no. 8, p. 085702, 2010.

[158] A. Ortiz-Conde, F. J. Garcia Sanchez, J. J. Liou, A. Cerdeira, M. Estrada, and Y. Yue, "A review of recent mosfet threshold voltage extraction methods," *Microelectronics Reliability*, vol. 42, no. 4-5, pp. 583–596, 2002.

[159] Engineering Statistics Handboook; http:///www.itl.nist.gov/div898/handbook/.

[160] P. Dutta and P. M. Horn, "Low-frequency fluctuations in solids: 1/f noise," *Reviews of Modern Physics*, vol. 53, no. 3, p. 497, 1981.

[161] P. G. Collins, M. S. Fuhrer, and A. Zettl, "1/f noise in carbon nanotubes," *Applied Physics Letters*, vol. 76, no. 7, pp. 894–896, 2000.

[162] M. Ishigami, J. H. Chen, E. D. Williams, D. Tobias, Y. F. Chen, and M. S. Fuhrer, "Hooge's constant for carbon nanotube field effect transistors," *Applied Physics Letters*, vol. 88, no. 20, pp. 203 116–3, 2006.

[163] F. Liu, K. L. Wang, D. Zhang, and C. Zhou, "Noise in carbon nanotube field effect transistor," *Applied Physics Letters*, vol. 89, no. 6, pp. 063 116–3, 2006.

[164] E. S. Snow, J. P. Novak, M. D. Lay, and F. K. Perkins, "1/f noise in single-walled carbon nanotube devices," *Applied Physics Letters*, vol. 85, no. 18, pp. 4172–4174, 2004.

[165] S. Reza, Q. T. Huynh, G. Bosman, J. Sippel-Oakley, and A. G. Rinzler, "Thermally activated low frequency noise in carbon nanotubes," *Journal of Applied Physics*, vol. 99, no. 11, pp. 114 309–4, 2006.

[166] J. Mannik, I. Heller, A. M. Janssens, S. G. Lemay, and C. Dekker, "Charge noise in liquid-gated single-wall carbon nanotube transistors," *Nano Letters*, vol. 8, no. 2, pp. 685–688, 2008.

[167] Y.-M. Lin, J. Appenzeller, Z. Chen, and P. Avouris, "Electrical transport and 1/f noise in semiconducting carbon nanotubes," *Physica E: Low-dimensional Systems and Nanostructures*, vol. 37, no. 1-2, pp. 72–77, 2007.

[168] M. Briman, K. Bradley, and G. Gruner, "Source of 1/f noise in carbon nanotube devices," *Journal of Applied Physics*, vol. 100, no. 1, pp. 013 505–5, 2006.

[169] K. K. Hung, P. K. Ko, C. Hu, and Y. C. Cheng, "A unified model for the flicker noise in metal-oxide-semiconductor field-effect transistors," *Electron Devices, IEEE Transactions on*, vol. 37, no. 3, pp. 654–665, 1990.

[170] Y. Lin, J. C. Tsang, M. Freitag, and P. Avouris, "Impact of oxide substrate on electrical and optical properties of carbon nanotube devices," *Nanotechnology*, vol. 18, no. 29, p. 295202, 2007.

[171] D. Tobias, M. Ishigami, A. Tselev, P. Barbara, E. D. Williams, C. J. Lobb, and M. S. Fuhrer, "Origins of 1/f noise in individual semiconducting carbon nanotube field-effect transistors," *Physical Review B*, vol. 77, no. 3, p. 033407, 2008.

[172] N.-P. Wang, S. Heinze, and J. Tersoff, "Random-telegraph-signal noise and device variability in ballistic nanotube transistors," *Nano Letters*, vol. 7, no. 4, pp. 910–913, 2007.

[173] S. Kim, S. Kim, D. B. Janes, S. Mohammadi, J. Back, and M. Shim, "Dc modeling and the source of flicker noise in passivated carbon nanotube transistors," *Nanotechnology*, vol. 21, no. 38, p. 385203, 2010.

[174] F. N. Hooge, "1/f noise is no surface effect," *Physics Letters A*, vol. 29, no. 3, pp. 139–140, 1969.

[175] R. J. Carter, E. Cartier, A. Kerber, L. Pantisano, T. Schram, S. De Gendt, and M. Heyns, "Passivation and interface state density of SiO_2/HfO_2-based/polycrystalline-Si gate stacks," *Applied Physics Letters*, vol. 83, no. 3, pp. 533–535, 2003.

[176] H. Park, M. S. Rahman, M. Chang, B. H. Lee, R. Choi, C. D. Young, and H. Hwang, "Improved interface quality and charge-trapping characteristics of mosfets with high-kappa; gate dielectric," *Electron Device Letters, IEEE*, vol. 26, no. 10, pp. 725–727, 2005.

[177] M. S. Rahman, H. Park, M. Chang, D. Lee, B. H. Lee, and H. Hwang, "Enhanced reliability and performance of high-k mosfet by two-step annealing," *Electrochemical and Solid-State Letters*, vol. 9, no. 4, pp. G127–G129, 2006.

[178] Y. Yasuki, O. Yasuhide, M. Kenzo, and M. Kazuhiko, "Noise reduction of carbon nanotube field-effect transistor biosensors by alternating current measurement," *Japanese Journal of Applied Physics*, vol. 40, p. 06FJ01, 2009.

Publications

Reviewed Articles

A1 H. Chandrahalim, M. Mattmann, K. Chikkadi, S-W. Lee, Y. Liu, C. Roman, and C Hierold, "Strain-modulated steady-state motional currents in a capacitively transduced vibrating single-walled carbon nanotube," *In preparation for submission to Nanotechnology*, 2011.

A2 K. Chikkadi, M. Mattmann, M. Muoth, L. Durrer, C. Hierold, "The role of pH in the density control of ferritin-based catalyst nanoparticles towards scalable single-walled carbon nanotube growth," *Microelectronic Engineering*, article in press. DOI: 10.1016/j.mee.2011.02.069, 2011.

A3 M. Mattmann, D. Bechstein, C. Roman, K. Chikkadi, and C. Hierold, "Reduction of gate hysteresis above ambient temperature via ambipolar pulsed gate sweeps in carbon nanotube field effect transistors for sensor applications," *Applied Physics Letters*, vol. 97, no. 15, p. 153103–153103, 2010.

A4 M. Muoth, S.-W. Lee, K. Chikkadi, M. Mattmann, T. Helbling, A. Intlekofer, and C. Hierold, "Encapsulation of electrical contacts for suspended single-walled carbon nanotubes by atomic layer deposition," *physica status solidi (b)*, vol. 247 no. 11-12, p. 2997–3001, 2010.

A5 M. Mattmann, C. Roman, T. Helbling, D. Bechstein, L. Durrer, R. Pohle, M. Fleischer, and C. Hierold,"Pulsed gate sweep strategies for hysteresis reduction in carbon nanotube transistors for low concentration NO_2 gas detection," *Nanotechnology*, vol. 21, no. 18, p. 185501, 2010.

A6 T. Helbling, C. Hierold, C. Roman, L. Durrer, M. Mattmann, and V. M. Bright, "Long term investigations of carbon nanotube transistors encapsulated by atomic-layer-deposited Al_2O_3 for sensor applications," *Nanotechnology*, vol. 20, no. 43, p. 434010, 2009.

A7 M. Mattmann, T. Helbling, L. Durrer, C. Roman, C. Hierold, R. Pohle, and M. Fleischer,"Sub-ppm NO_2 detection by Al_2O_3 contact passivated carbon nanotube field effect transistors," *Applied Physics Letters*, vol. 94, no. 18, p. 183502–183503, 2009.

A8 O. Florescu, M. Mattmann, and B. Boser, "Fully integrated detection of single magnetic beads in complementary metal-oxide-semiconductor," *Journal of Applied Physics*, vol. 103, no. 4, p. 046101–046103, 2008.

Conference Proceedings (partially reviewed)

C1 M. Mattmann, D. Bechstein, C. Roman, K. Chikkadi, T. Helbling, L. Durrer, R. Pohle, M. Fleischer, and C. Hierold, "Electrical initialization to erase history in hysteretic carbon nanotube transistors for sensing applications," in *Proc. Eurosensors XXIV*, Linz, Austria, 2010.

C2 M. Mattmann, T. Helbling, L. Durrer, C. Roman, R. Pohle, M. Fleischer, and C. Hierold,"Hysteresis reduction and measurement range enhancement of carbon nanotube based NO_2 gas sensors by pulsed gate voltages," in *Proc. Eurosensors XXIII*, Lausanne, Switzerland, 2009.

Patent Applications

P1 O. Florescu, M. Mattmann, B. Boser, "Integrated circuit apparatus used as component of biosensor device has magnetic concentration/magnetization field generator embedded in substrate beneath exposed surface area and between magnetic field detector and exposed surface area," Patent Numbers: WO2009091926-A2; WO2009091926-A3; EP2235516-A2; KR2010115744-A; US2011018532-A1; IN201004175-P4; CA2711956-A1, 2009.

Conference Talks and Invited Talks

T1 M. Mattmann, D. Bechstein, C. Roman, K. Chikkadi, T. Helbling, L. Durrer, R. Pohle, M. Fleischer, and C. Hierold, "Electrical initialization to erase history in hysteretic carbon nanotube transistors for sensing applications," in *Eurosensors XXIV*, Linz, Austria, 2010.

T2 M. Mattmann, K. Chikkadi, C. Roman, T. Helbling, L. Durrer, R. Pohle, M. Fleischer, M. Haluska, and C. Hierold, "CNFET NO_2 sensing," in *Technotubes Project Progress Meeting on May 31st*, Trieste, Italy, 2010.

T3 M. Mattmann, T. Helbling, L. Durrer, C. Roman, R. Pohle, M. Fleischer, and C. Hierold,"Hysteresis reduction and measurement range enhancement of carbon nanotube based NO_2 gas sensors by pulsed gate voltages," in *Eurosensors XXIII*, Lausanne, Switzerland, 2009.

Poster Presentations

P1 M. Haluska, M. Mattmann, K. Chikkadi, C. Roman, C. Hierold, "Utilization of single-walled carbon nanotubes for NO_x sensors," *International Winterschool on Electronic Properties of Novel Materials*, Kirchberg, Austria, 2011.

P2 M. Mattmann, C. Hierold, "Low power sub-ppm detection of NO_2 gas with carbon nanotube sensors," *Industry Day 2010, Micro and Nano Science Platform, ETH Zurich* Zurich, Switzerland, 2010.

P3 K. Chikkadi, M. Mattmann, M. Muoth, L. Durrer, C. Hierold, "The role of pH in the density control of ferritin-based catalyst nanoparticles towards scalable single-walled carbon nanotube growth," *36th International conference on Micro and Nano Engineering (MNE 2010)*, Genoa, Italy, 2010.

P4 S-W. Lee, M. Muoth, T. Helbling, M. Mattmann, C. Hierold, "ALD-assisted Metal Lift-off for Contamination-free Contact Areas to Carbon Nanotubes," *36th International conference on Micro and Nano Engineering (MNE 2010)*, Genoa, Italy, 2010.

P5 M. Haluska, L. Durrer, T. Helbling, M. Muoth, M. Mattmann, K. Chikkadi, T. Süss, C. Roman, Ch. Hierold, "Targeted growth of single-walled carbon nanotubes for nanosensor devices," *NT10, 11th International Conference on the Science and Application of Nanotubes*, Montreal, Canada, 2010.

P6 L. Durrer, M. Muoth, M. Mattmann, T. Helbling, K. Chikkadi, T. Süss, M. Haluska, Ch. Hierold, "Targeted growth of single walled carbon nanotubes for applications in nanosensor devices," *International Winterschool on Electronic Properties of Novel Materials*, Kirchberg, Austria, 2010.

P7 M. Muoth, K. Chikkadi, M. Mattmann, T. Helbling, C. Hierold, "Encapsulation of electrical contacts for suspended SWNTs by atomic layer deposition," *International Winterschool on Electronic Properties of Novel Materials*, Kirchberg, Austria, 2010.

P8 M. Mattmann, T. Helbling, L.Durrer, C. Roman, R. Pohle, M. Fleischer, C. Hierold, "Low Power Sub-ppm Detection of NO_2 Gas with Carbon Nanotube Sensors," *NanoEurope*, Rapperswil, Switzerland, 2009.

P9 M. Mattmann, T. Helbling, L.Durrer, C. Roman, R. Pohle, M. Fleischer, C. Hierold, "Low Power Sub-ppm Detection of NO_2 Gas with Carbon Nanotube Sensors," *KTI Meeting*, Neuchâtel, Switzerland, 2009.

Curriculum vitae

Personal Details

Name	Moritz Peter Paul Mattmann
Birth	13 September 1983 in Uster, Switzerland
Citizenship	Switzerland
Marital Status	Single

Education

10/2007 –	**ETH Zurich, Micro and Nanosystems, Switzerland** Dissertation: *Carbon Nanotube Field Effect Transistors with Al_2O_3 Passivated Metal Contacts as NO_2 Gas Sensors.*
10/2002 – 09/2007	**ETH Zurich, Department of Information Technology and Electrical Engineering** Graduation with Masters Degree
03/2007 – 09/2007	**University of California at Berkeley (UCB), Group of Prof. Bernhard Boser, Berkeley Sensor and Actuator Center (BSAC), USA** Visiting Scholar. Master Thesis: *Fully Integrated Detection of Individual Micro Magnetic Beads in CMOS.*
08/1996 – 05/2002	**Kantonsschule Zug, ZG** Graduation with Matura, major: English / Latin

Work Experience

10/2007 –	**ETH Zurich, Micro and Nanosystems, Switzerland** Research and teaching assistant
10/2006 – 02/2007	**Phonak AG, Stäfa, Switzerland** Internetship. Microsystems Group: *Testing of a communication protocol of a wireless link between hearingaids.*

Languages

German	mother tongue
English	fluent (Level C2 - Common European Framework of Reference for Languages (CEFR))
French	Oral communication (Level B1)